Tandem Laser Ablation Synthesis in Solution-Galvanic Replacement Reaction (LASiS-GRR): A facile route for the synthesis of complex intermetallic nanomaterials with engineered functionalities

A Dissertation Presented for the

Doctor of Philosophy

Degree

The University of Tennessee, Knoxville

Sheng Hu

May 2016

Dedication

To my parents, Zhizhong Hu, Xinyu Huang, and my girlfriend, Ting Wu.

"When there is no enemy within, the enemies outside cannot hurt you."

Acknowledgement

First of all, I would like to offer my great appreciation to my advisor, Dr. Dibyendu Mukherjee, for his compassionate mentorship, tireless inspiration and encouragement throughout my PhD study in the past three years, which would not have been possible without his support. I am also exceptionally grateful to Dr. Bamin Khomami, my mentor and advisor during the Master program. I appreciate him for contributing his knowledge and expertise to me as well as introducing me to Dr. Dibyendu Mukherjee for continuing my PhD. Also I would like to extend my sincere thanks to Dr. Ramakrishnan Kalyanaraman and Dr. Robert Counce as well as Dr. Bamin Khomami for their willingness to serve on my committee and offer helpful feedback. Besides, I acknowledge the financial support and funding through Sustainable Energy Education and Research Center (SEERC) at the University of Tennessee, Knoxville (UTK.).

Next I would express my appreciation to my collaborators who also made great contribution to my research work. I would like to thank Dr. John Dunlap and Dr. Gerd Duscher for their assistance on TEM characterizations, Dr. Maulik Patel for his help on XRD experiments, and finally, Dr. Ilia Ivanov for his guidance on the ORNL instruments made available through the CNMS user support facilities. Also, thank all my lab mates and all my friends in USA and China for their consistent support.

Finally, and most importantly, my sincere appreciation goes out to all my family members for their unyielding love and support.

Abstract

Tailoring the heteronanostructures of nanoscale materials to tune their structure-property relations for desirable interfacial energetics is imperative for their catalytic, optoelectronic and electrochemical applications. Current PhD thesis develops a facile, yet "green" synthesis route that uses laser ablation synthesis in solution in tandem with galvanic replacement reaction (tandem LASiS-GRR) as a one-pot, one-step technique for manufacturing diverse and complex heteronanostructures of metal oxides, hydroxides, nanocomposites (NCs), and nanoalloys (NAs). The scientific concept here is that the non-equilibrium thermodynamics and kinetics of high-energy LASiS-GRR can be tuned by laser parameters and solvent chemistry to form complex NCs/NAs of tailored sizes/shapes, metastable structures and compositions.

The results indicate that the presence or absence of solution-phase oxygen (O_2) during LASiS on bulk Cobalt (Co) produces cobalt monoxide (CoO) or, single crystal beta-cobalt hydroxide (β-cobalt hydroxide), nanoparticles (NPs) respectively as the metastable states. These intermediates finally transform into cobaltosic oxide (Co_3O_4) NPs, along with the formation of Co_3O_4 nanorods with enhanced localized surface plasmon resonance (LSPR) at high pH. In contrast, LASiS-GRR on Co in Potassium tetrachloride palatinate (K_2PtCl_4) salt solution produces NCs of PtCo NAs embedded in cobalt oxide (CoO_x) matrices (i.e., $PtCo/CoO_x$). These NCs exhibit outstanding bifunctional electrocatalytic activities for both oxygen reduction reaction (ORR) and oxygen evolution reaction (OER) along with better stability, which are attributed to the shrunken lattice constants of alloyed PtCo that promote oxygen adsorption, and synergic "spillover" effects from high surface area CoO_x matrices that promote symbiotic adsorption/desorption of intermediate species. Subsequent acid wash of the aforementioned $PtCo/CoO_x$ NCs results in spherical PtCo NAs with tunable sizes, compositions and degrees of alloying. These NAs exhibit uniformly alloyed core encapsulated in few nanometers of Pt-rich shell. Such core-shell NA structures along

with high degrees of alloying promote their outstanding electrocatalytic ORR activities in acid electrolytes. Finally, preliminary results for LASiS-GRR on bulk zinc/titanium (Zn/Ti) in silver nitrate ($AgNO_3$) salt solution indicate the formation of plasmonic Ag NPs embedded in zinc oxide (ZnO) or titania (TiO_2) matrices, with the majority of Ag NPs covered by spherical TiO_2 that are anti-corrosive in acid.

Table of Contents

Chapter 1 Tandem Laser Ablation Synthesis in Solution-Galvanic Replacement Reacton (LASiS-GRR): An Overview 1

1.1 Introduction of LASiS and LASiS-GRR 1

1.1.1 Conventional routes for synthesizing NMs 1

1.1.2 Laser ablation synthesis in solution (LASiS) 2

1.1.3 Laser ablation synthesis in solution-galvanic replacement reaction (LASiS-GRR) 5

1.2 Applications of LASiS-GRR for the synthesis of functional NMs 6

1.2.1 Bifunctional electrocatalysts for oxygen reduction/evolution reactions (ORR/OER) in alkaline fuel cells 7

1.2.2 ORR electrocatalysts for acid proton exchange membrane fuel cells (PEMFCs) 9

1.2.3 Photocatalysts for light-activated OER/water oxidation: Preliminary studies 10

1.3 Outline of dissertation 13

Chapter 2 Experimental Setup and Methodology 15

2.1 Description of the LASiS/LASiS-GRR setup 15

2.2 Sample preparation using LASiS/LASiS-GRR 16

2.2.1 Synthesis of $CoO_x/Co(OH)_2$ 16

2.2.2 Synthesis $PtCo/CoO_x$ NCs 17

2.2.3 Synthesis of PtCo NAs 17

2.2.4 Synthesis of ZnO/TiO_2 embedded by Ag/Au 18

2.3 Experimental and theoretical characterization techniques 18

2.3.1 TEM related characterizations 18

2.3.2 Other physical characterizations 19

2.3.3 Electrochemical tests 21

2.3.4 Theoretical Modeling of Rate kinetics of LASiS-GRR 23

2.3.5 DFT calculation 25

Chapter 3 Synthesis of nanostructured oxides and hydroxides of cobalt using laser ablation synthesis in solution (LASiS) 26

3.1 Introduction 26

3.2 Results and discussion 27

3.2.1 Chemical pathway for the products during LASiS on Co 27
3.2.2 Effect of laser parameters during LASiS on Co 31
3.2.3 Effect of solution-phase pH during LASiS on Co 38
3.3 Summary 42
Chapter 4 Synthesis of $PtCo/CoO_x$ nanocomposites (NCs) via LASiS-GRR as ORR/OER bifunctional electrocatalysts in alkaline conditions 44
4.1 Introduction 44
4.2 Results and discussion 45
4.2.1 Mechanistic picture of LASiS-GRR 45
4.2.2 Structure and composition analysis for the $PtCo/CoO_x$ NCs 47
4.2.3 Investigation of ORR/OER catalytic activities 54
4.3 Summary 61
Chapter 5 Synthesis of PtCo nanoalloys (NAs) via LASiS-GRR as ORR electrocatalysts in acidic conditions 63
5.1 Introduction 63
5.2 Results and discussion 65
5.2.1 Synthesis and characterization of PtCo NAs 65
5.2.1.1 PtCo NAs synthesized with different Pt salt concentrations 65
5.2.1.2 PtCo NAs synthesized with different pH conditions 71
5.2.2 Investigation of ORR electrocatalytic activities 74
5.2.3 Reaction Pathways for PtCo NA formation: A discussion 78
5.2.4 Theoretical Modeling of Rate Kinetics 81
5.2.5 DFT calculation 84
5.3 Summary 86
Chapter 6 Future works with preliminary results: Synthesis of plasmonic nanocomposites for photocatalytic applications and other complex intermetallic nanomaterial systems 88
6.1 Synthesis of plasmonic nanocomposites for photocatalytic applications 88
6.1.1 Plasmonic nanocomposites: An introduction 88
6.1.2 Results 90
6.1.2.1 Synthesis of $Ag/Au@ZnO/TiO_2$ via LASiS/LASiS-GRR 90
6.1.2.2 Characterization of LSPR properties 93
6.2 Applications of LASiS/LASiS-GRR technique for the synthesis of other intermetallic NMs 95
6.2.1 LASiS on other metals 95
6.2.2 LASiS/LASiS-GRR in organic solvents 97
6.2.3 Other binary noble metal-transition metal nanoalloys 98

6.2.4 Ternary alloys 98
6.3 Post treatment after LASiS-GRR 100
6.4 Summary 101
Chapter 7 Summary 102
References 106
Appendices 122
Appendix A. Band gap/edge measurement 123
Experimental 123
Band gap measurement 123
Band edge measurement 124
Preliminary results 125
Appendix B. EELS study of the plasmonic Ag/TiO_2 NCs 127
Vita 129

List of Tables

Table 3.1 Comparison of standard and experimental d-spacing calculated from SAED 28
Table 3.2 Comparison of mean sizes and geometric standard deviations (GSD) of synthesized Co_3O_4 NPs under different laser fluence. 38
Table 4.1 Pt and Co concentrations from ICP-OES measurements for various $PtCo/CoO_x$ NCs synthesized by LASiS-GRR at different initial K_2PtCl_4 salt concentrations. 48
Table 4.2 Experimental d-spacing values calculated from the SAED results in Fig. 4.2. 49
Table 4.3 Calculated alloyed Pt:Co ratio from XRD results in Fig. 4.5. 53
Table 4.4 Comparison of OER and ORR overpotentials for $PtCo/CoO_x$ NCs, Co_3O_4 and the commercial Pt/C samples along with the respective combined overpotentials. 61
Table 5.1 Summary of degree of alloying for various PtCo NAs through LASiS-GRR. 65
Table 5.2 Summary of electrochemistry test results. 77
Table 5.3 pH progression during LASiS-GRR on Co in K_2PtCl_4 with different initial pH values. 83

List of Figures

Fig. 1.1 Schematic diagram for LASiS by a nanosecond laser [35] 4
Fig. 1.2 Schematic diagram of a regenerative alkaline fuel cell, cathode and anode correspond to the left and right hand sides respectively. 8
Fig. 1.3 Schematics for the proposed PS I-mediated bio-photoelectrochemical cell using intermetallic (IM) nanoalloy/nanocomposites (NA/NC) as HER electrocatalysts and bio-mimetic metal/metal oxide NC as WOC photocatalysts. 11
Fig. 1.4 Energy diagrams of phtoocatalytic water splitting based on (**a**) one-step excitation and (**b**) two-step excitation (Z-scheme).[132] 12
Fig. 2.1 Schematic diagram of the designed multi-functional LASiS setup 15
Fig. 2.2 Experimental setup showing the three-compartment rotating disk electrode (RDE) cell (Pine LLC) 21
Fig. 3.1 TEM images **(top)** and the corresponding SAED patterns **(bottom)** showing evolution of CoO_x NPs from LASiS by 532 nm laser at 1 J/cm^2: **(a), (c)** fresh sample; **(b), (d)** aged for three days. 29
Fig. 3.2 **(a), (b)** HRTEM images, and **(c), (d)** Raman spectra for CoO_x NPs prepared by 532 nm laser at laser fluence of 1 J/cm^2; **(a), (c)** fresh sample; **(b), (d)** aged for three days. 29
Fig. 3.3 **(a), (b), (c)**: Freshly prepared NPs from LASiS by 532 nm laser (1 J/cm^2) with N_2 purge generates hexagonal β-$Co(OH)_2$ crystals along with Co_3O_4 NPs; **(a)** Bright field STEM image; **(b)** SAED pattern indicating single crystal β-$Co(OH)_2$ NP on <001> zone axis (Inset: corresponding TEM image); **(c)** HRTEM image for β-$Co(OH)_2$ crystal showing the lattice d-spacing; **(d)** SAED pattern of the sample aged for three days indicating Co_3O_4 NPs. 30
Fig. 3.4 Chemical pathway for the formation of Co_3O_4 NPs via LASiS on Co with/without dissolved O_2. 31
Fig. 3.5 TEM images **(top)** and particle size distributions (PSD) **(bottom)** for 1064 nm laser ablated Co_3O_4 NPs at different laser fluences: **(a), (d)** 0.9 J/cm^2; **(b), (e)** 41 J/cm^2; **(c), (f)** 107 J/cm^2. The vertical axis of PSD shows the particle number concentration (PNC). 32
Fig. 3.6 TEM images **(top)** and particle size distributions (PSD) **(bottom)** for 532 nm laser ablated Co_3O_4 NPs at different laser fluences: **(a), (d)** 1.0 J/cm^2; **(b), (e)** 43 J/cm^2; **(c), (f)** 114 J/cm^2. The vertical axis of PSD shows the particle number concentration (PNC). 33
Fig. 3.7 **(a)** Specific area productivity of Co_3O_4 NPs per unit ablation time; **(b)** Focused laser energy (1064 nm) penetration (%) through a glass of DI-water at different laser fluences, where energy penetration (%) is the ratio of penetrated laser energy over the original laser energy; **(c)** NP concentration evolution in time for low laser fluence case of ~0.3 J/cm^2. **(d)** Unfocused

laser energy (1064 nm and 532 nm) penetration (%), through Co_3O_4 colloid as well as an equivalent column of DI-water. 35
Fig. 3.8 TEM images showing: **(a)** the original NPs generated by LASiS and the alterations in their sizes and shapes after re-ablation (laser energy of 170 mJ/pulse) with: **(b)** 1064 nm laser and **(c)** 532 nm laser; **(d)-(f)** indicate PSDs corresponding to the samples shown in **(a)**, **(b)**, and **(c)** respectively. 37
Fig. 3.9 **(a)-(c)** TEM images of Co_3O_4 NPs obtained from LASiS at: **(a)** pH=7; **(b)** pH=13; **(c)** pH=14; (532 nm laser at a fluence of ~1 J/cm^2); **(d), (e)** the corresponding HRTEM images for the case of: **(d)** pH=13 and **(e)** pH=14; (Insets: SAED patterns); **(f)** UV-Vis absorption spectra for colloidal NPs synthesized at different pH values. 39
Fig. 3.10 Pourbaix diagram for Cobalt-water system. 39
Fig. 3.11 Re-irradiation (RI) by 532 nm laser of Co_3O_4 NRs synthesized through LASiS at pH=13 **(top)** and pH=14 **(down)** for 30 min.....41
Fig. 4.1 Schematic representation of the tandem LASiS-GRR technique that synthesize PtCo/CoO_x nanocomposites (NCs). 46
Fig. 4.2 **a-d.** TEM images along with the corresponding SAED patterns (inset) for the PtCo/CoO_x NCs synthesized by LASiS-GRR with different Pt:Co atomic ratios of: **a.** 1:9 (PtCo-1); **b.** 1:4 (PtCo-2); **c.** 1:2 (PtCo-3); **d.** 1:1 (PtCo-4). The scale bar in for SAED patterns is 5 (1/nm); **e-h.** Corresponding size distributions for dark colored PtCo alloyed NPs in **a-d**.....50
Fig. 4.3 **a.** Representative HRTEM image of PtCo-2 sample with the corresponding positions marked b, c, d indicating the lattice fringes in the enlarged images for: **b.** Pt, **c.** Co_3O_4, and **d.** CoO respectively.....51
Fig. 4.4 EDX results for PtCo-3 sample along with: **a.** HAADF image, and elemental mappings for **b** Pt, **c.** Co and **d.** O respectively; **e, f.** Corresponding EDX spectra at the positions marked in **a.** (Cu and C signals are from the TEM carbon film with copper grids). 52
Fig. 4.5 Comparison of XRD patterns for PtCo/CoO_x nanocomposites with different Pt:Co ratios along with standard peak positions for Co_3O_4, CoO and Pt indicated by yellow, purple and green vertical lines respectively. The values marked in the figure indicate the PtCo (111) peak positions. 52
Fig. 4.6 Electrochemistry data for as-synthesized Co_3O_4 NPs and PtCo/CoO_x NCs compared to standard Pt/C samples using: **a.** Linear sweep voltammograms for ORR analysis in 1 M KOH electrolyte saturated with dissolved O_2 at 1600 rpm and scan rate of 5 mV/s; **b.** Tafel plots from **a**; **c.** Comparison of mass activities per unit Pt mass loading at 0.85 V vs. RHE; **d.** Koutecky-Levich plots from rotating disk voltammogram (RDV) data (shown in inset) for PtCo-3 at different potentials; **e.** Stability comparison for Co_3O_4, PtCo-3 and standard Pt/C through chronoamperometry (CA) tests.....56
Fig. 4.7 **a.** Linear sweep voltammograms for OER analysis on PtCo/CoO_x NCs compared to those for Co_3O_4 NPs and standard Pt/C samples; **b.** Corresponding Tafel plots in the potential range of 1.55 - 1.60 V. 58

Fig. 4.8 **a.** Comparison of bifunctional catalytic activities for both OER and ORR through Linear sweep voltammogram (LSV); **b.** Evolution of ORR, OER and combined overpotentials for catalytic samples understudy with the increase of Pt molar ratio. 59
Fig. 4.9 Schematic illustrating the mechanism ofthe "spill-over effect". 60
Fig. 5.1 **a-d.** TEM images along with the corresponding SAED patterns (insets) for the PtCo NAs: **a.** PtCo-1; **b.** PtCo-2; **c.** PtCo-3; **d.** PtCo-4 synthesized via LASiS-GRR at different initial K_2PtCl_4 concentrations (125 mg/l, 250 mg/l, 375 mg/l, 500 mg/l) with the respective ablation times of 4 min, 7 min, 13 min, 20 min. The scale bar in for SAED patterns is 5 (1/nm). 65
Fig. 5.2 Comparison of XRD patterns for various PtCo NAs synthesized at different initial K_2PtCl_4 concentrations and ablation times. The black dashed lines mark the standard 2 peak positions for the respective labeled species. 67
Fig. 5.3 HRTEM images of PtCo-2 (top) and the pH11 (down) samples. 69
Fig. 5.4 EDX (**a-c**) and EELS elemental mapping results (**d-h**) for PtCo-2 sample showing: **a.** HAADF-STEM image; **b, c.** EDX mapping of Pt and Co for **a** on a large scale; **d.** EELS spectrum of a single particle shown in inset; **e, f.** EELS mapping of the corresponding Pt and Co; **g.** EELS mapping indicating Pt/Co atomic ratio from **e** and **f**; **h.** Pt atomic ratio (%) distribution across the line shown in **g**. 69
Fig. 5.5 EELS spectrum at the particle edge: **a.** the Pt-$N_{2,3}$ edge has low intensity and small signal to noise ratio, while an oxygen-K edge is distinct, which is possibly due to random noise or unexpected oxygen signal; **b.** an clear Pt-$N_{2,3}$ edge peak with high signal to noise ratio at the right edge of the NP.70
Fig. 5.6 EELS spectrum (**a**) and mapping (**c**) of the particle using Pt M-$_{4,5}$ edge. 70
Fig. 5.7 Comparison of PtCo NAs synthesized via LASiS-GRR at acid (**a-d,** pH3) and alkaline (**e-h,** pH11) conditions. **a, e.** TEM images with the corresponding SAED patterns shown in the insets. (The scale bars in the insets are 5 /nm) **b, f**. HAADF STEM images; and **c, d, g, h.** the corresponding Pt and Co mappings for **b** and **f**. 71
Fig. 5.8 XRD patterns for PtCo NAs at pH11 without NaCl wash. The dash lines mark the standard peak positions for each species. The small peaks in the 2θ range from 15^o to 35^o are corresponding to the $PtCl_2$ signals. 72
Fig. 5.9 EDX images for PtCo NAs obtained at **a.** pH 3, **b**. pH7 (PtCo-2) and **c**. pH11. The Cu signal is from the substrate. The Co atomic ratios are quantified to be 5%, 21% and 38% respectively. 73
Fig. 5.10 XRD patterns for PtCo NAs at different pH conditions with same initial K_2PtCl_4 concentration and ablation time (250 mg/l and 7 min). The dash lines mark the standard peak positions for each species. 73
Fig. 5.11 Electrochemistry data indicating ORR activities of PtCo NAs made via LASiS-GRR when compared to commercial Pt/C samples using: **a.** Cyclic

voltammetry curves at a scan rate of 50 mV/S; **b.** Linear sweep voltammograms for ORR polarization curves in 0.1 M $HClO_4$ electrolyte saturated with dissolved O_2 at 1600 rpm and scan rate of 5 mV/s; **c.** Koutecky-Levich plots from rotating disk voltammogram (RDV) data (shown in inset) for PtCo-2 at different potentials (0.70-0.87 V) indicating four electron transport process for ORR; **d.** Corresponding Tafel plots; **e.** Comparison of mass activity and specific activity at 0.9 V vs. RHE; **f.** Cyclic voltammetry curves indicating the % ECSA values and Co ratio (%) in the alloy after various numbers of potential cycles at a scan rate of 100 mV/s...76

Fig. 5.12 Electrochemistry data for PtCo NAs made from LASiS-GRR at different pH conditions: **a.** Cyclic voltametry curves at a scan rate of 50 mV/S; **b.** Linear sweep voltammograms for ORR analysis in 0.1 M $HClO_4$ electrolyte saturated with dissolved O_2 at 1600 rpm and scan rate of 5 mV/s; **c.** The corresponding Tafel plots; **d.** Comparison of mass activity and specific activity at 0.9 V vs. RHE. 78

Fig. 5.13 Schematic diagram indicating the formation of PtCo NAs via tandem LASiS-GRR using different initial Pt^{2+} concentrations and pH conditions; pulsed laser produces seeding Co NPs which expand with the cavitation bubble and react with either Pt^{2+}, H^+ or reduced Pt (alloying process) at the bubble-liquid interface during collisional quenching. Based on the different Pt^{2+} concentration (low, medium, high) and pH conditions (acid, neutral, alkaline), different degrees of alloying for Co_{al} are obtained. 80

Fig. 5.14 Theoretical modeling of rate kinetics of LASiS-GRR on Co in K_2PtCl_4 solutions for the aforementioned four samples: **a.** PtCo-1; **b.** PtCo-2; **c.** PtCo-3; **d.** PtCo-4. The green hollow dots show the experimental [Pt^{2+}] evolution results, the blue lines reveal the atomic Co ratio in the PtCo alloy. 81

Fig. 5.15 Comparison of the theoretical and experimental values of atomic Co% in the four PtCo NAs.....82

Fig. 5.16 Theoretical modeling of rate kinetics of LASiS-GRR on Co in K_2PtCl_4 solutions at pH3 (**a**) and pH11 (**b**) conditions as well as with continuous supply of K_2PtCl_4, where the injection rates are 7 and 10.6 mg $L^{-1}min^{-1}$ for the (**c**) and (**d**) respectively. 84

Fig. 5.17 Solvated surface structures on CS-Pt/PtCo (22%Co) (111) in a 3 × 3 unit cell for O/OH adsorption at different positions: **b, c,** on top of Pt; **d, e,** at hollow positions. 85

Fig. 5.18 **a**, Comparison of free energy changes during ORR; **b**, Activity volcano plot for ORR as a function of ΔE_O. 86

Fig. 6.1 LASiS on Zn (**a** and **b**) and Ti (**c** and **d**) in water (1064 nm laser for 10 min). **b**, **d**, HRTEM images for the circled position in **a** and **b** respectively indicating the products are ZnO and Srilankite type TiO_2 (only for the spherical part). The insets show the SAED patterns. 90

Fig. 6.2 **a**, HAADF image of the sample synthesized via LASiS on Zn in $AgNO_3$;

b, c, d, the corresponding Ag, Zn and O EDX mappings. 91
Fig. 6.3 **a** HAADF image of the sample synthesized via LASiS on Ti in $AgNO_3$ after HNO_3 wash; **b, c** Enlarged HAADF image and EDX mapping of **a**; **d** Sample **a** after RI**; e, f** Enlarged HAADF image and EDX mapping of **d**. ...92
Fig. 6.4 XRD profile for the synthesized Ag/TiO_2 (**a**) and Ag/ZnO (**b**) NCs. 92
Fig. 6.5 UV-Vis absorbance of **a**, TiO_x/ZnO NPs with/without embedded Ag; **b**, acid washed Ag/TiO_x NCs after re-irradiated (RI) for different time scales..93
Fig. 6.6 **a**, TEM image of Au/TiO_2 NCs synthesized via LASiS-GRR, the insets at top and bottom exhibit the SAED of Au and TiO_2 respectively; **b**, Comparison of UV-Vis spectra of Ag/TiO_2 and Au/TiO_2. 94
Fig. 6.7 TEM images of LASiS on Cu in water: **a**, right after LASiS; **b**, after 3 days aging; **c, d,** the corresponding HRTEM images for the spherical NPs and NRs in **a**.....96
Fig. 6.8 LASiS on stainless steel in water: **a**, TEM images; **b**, SAED pattern; **c**, XRD data; **d**, EDX pattern. 96
Fig. 6.9 TEM and the corresponding SAED patterns of: **a, b,** LASiS on Zn in toluene; **c, d,** LASiS on Zn in toluene with $HAuO_4$. 97
Fig. 6.10 LASiS-GRR on Ni with K_2PtCl_4: **a-d,** EDX mapping; **e,** EDX spectrum; **f,** HRTEM. 98
Fig. 6.11 LASiS-GRR on Co with Na_2PdCl_4: **a, b, d, e,** EDX mapping; **c,** TEM image; **f,** EDX spectrum. 99
Fig. 6.12 EDX analysis of LASiS-GRR on Co with K_2PtCl_4 and Na_2PdCl_4.....99
Fig. 6.13 PtCo NA (synthesized at pH11) after TA at 700 C^o for 2h: **a**, HRTEM showing a core-shell structure with a very thin pure Pt shell and a Pt_3Co superlattice core; **b**, the corresponding XRD pattern.....100

Chapter 1 Tandem Laser Ablation Synthesis in Solution-Galvanic Replacement Reacton (LASiS-GRR): An Overview

1.1 Introduction of LASiS and LASiS-GRR

Nanomaterials (NMs) are defined as materials with single unit size ranging between 1 nm and 100 nm, which in general, comprise of aggregate of atoms or molecules from tens to thousands, and exhibiting large surface/interface to volume ratios. Metal NMs have attracted ever increasing interest from scientists and engineers from nearly all disciplines over the past several decades.[1–4] This interest has been generated largely due to various physico-chemical properties of NMs such as optical and magnetic properties, specific heats, melting points, and surface reactivity with size-dependent characteristics at the nanoscale that endows them a broad range of intriguing applications including information storage, catalysis, optics and electronics, optoelectronics, sensing materials, drug delivery etc.[5–8] Our research work in this dissertation is mainly focused on the synthesis, characterization and applications of various metal oxides, intermetallic NMs as well as complex nanocomposites (NCs), which have increasingly become prominent among the most important solid-state materials in modern science and technology.

1.1.1 Conventional routes for synthesizing NMs

Finding facile, economically viable and environmental friendly synthesis techniques of these aforementioned NMs is always of crucial importance. A variety of synthetic techniques have been developed so far, which in general can be divided into two categories, namely, the ‘‘top-down’’ routes, including the construction of nanoparticles from decomposition of a large solid by attrition, milling and pyrolysis,

etc.,[9–16] as well as the ‘‘bottom-up’’ approaches which entail the nucleation and condensation of atoms or molecules in either liquid or gas phase. With better environmental and process parameter controls, the latter approaches have attracted more research interests. Till date, NMs with diverse structures, compositions and morphologies have been developed within the ‘‘bottom-up’’ category, including chemical reduction or oxidation, hydrolysis, replacement reaction, microemulsions, as well as biomimetic synthesis, sol-gel method, etc.[9,17–26] However, most of those synthesis routes inevitably leave unwanted chemicals including surfactants (Sodium dodecyl sulfate (SDS), cetyltrimethylammonium bromide (CTAB), Polyvinylpyrrolidone (PVP), Dodecylamine, etc.), leftover reducing agents ($NaBH_4$, superhydride ($LiBEt_3H$), ascorbic acid, etc.) and different kinds of by-products on the surface of NMs that dramatically retard their applications, especially for catalytic performances.[27–33]As a consequence, it is imperative to seek for new synthesis techniques that are efficient, environmental friendly and economically viable.

1.1.2 Laser ablation synthesis in solution (LASiS)

Laser ablation synthesis in solution (LASiS) is a newly emerged, green synthesis technique for manufacturing nanoscale materials.[5,34–37] The general procedure of LASiS involves a high energy laser beam hitting on a metal target that is immersed in a liquid solution, which in turn creates colloidal nanoparticles in a meta-stable phase. The specific interest in LASiS arises due to its distinctive advantages of being a simple, elegant and yet chemical-free technique that requires minimal manual operation and low start-up cost.[35,38–42] In the past, LASiS has been used to synthesize various types of nanoparticles (NPs) comprising of heavy metals,[37,40] transition metals,[5,43] inter-metallic nano-colloids.[44,45] Additionally, a few morphologically complex nanostructures such as core-shell,[46,47] and hollow[48] NPs have also been synthesized using LASiS. Such synthesis routes become critical for fabrication of metal/intermetallic NPs with controlled size, shape, structure, and surface chemistry that finds wide applications in catalytic fields.[1,5,49,50]

The complex physics of laser-matter interactions involved during the nucleation of NPs via LASiS is still not clearly understood.[42,51] Unlike the relatively straight forward NP formation mechanism during laser ablation in gas phase,[52] the pulsed laser beam during LASiS creates a liquid-confined plasma plume with extremely high temperature and pressure on the metal target surface that results in thermal vaporization of the metal target and explosive boiling within the solvent.[51] Previous works have reported that the seeding NPs start to form inside an oscillating cavitation bubble resulting from the expanding plasma plume as well as undergo collisional quenching at the bubble-liquid interface when the bubbles collapse.[53] As can be seen from Fig. 1.1, the entire LASiS process can be divided into six stages within the first few milliseconds of the onset of ablation, i.e., laser pulse penetration in the liquid, absorption of laser pulse by target, ablated material detachment from target, plasma plume evolution and quenching, expansion and collapse of cavitation bubble, NP growth and aggregation.[35] Among all these stages, the detachment of ablated material plays a critical role in initiating the nucleation process, which is dominated by mainly three types of ablation mechanisms, vaporization, normal boiling and explosive boiling.[51] The onset of these mechanisms is controlled by the target surface temperature, which is dictated by laser fluence (laser energy per unit area) and pulse duration time. Specifically, vaporization refers to the emission of particles by sublimation or evaporation due to electron-phonon coupling, and theoretically, can occur at any laser fluence. Normal boiling, with low laser energy requirement usually induces heterogeneous nucleation and is strongly affected by the bubble diffusion. Finally, explosive boiling initiates the most efficient ablation mechanism at superheating conditions that results in homogeneous nucleation at a much higher energy threshold value than normal boiling.[35,51]

The structures, shapes and properties of NPs synthesized by LASiS are dictated by the laser parameters and environmental conditions of the experiment. The former includes laser fluence,[37,51] wavelength,[54] pulse duration time,[55] repetition rate, spot area, etc.

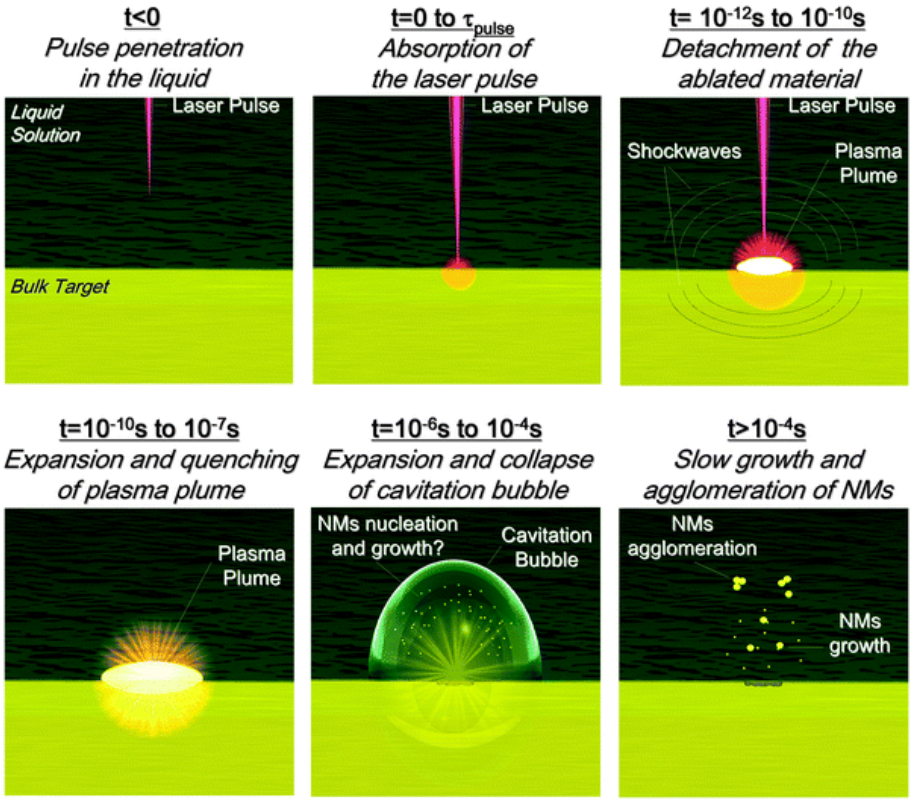


Fig. 1.1 Schematic diagram for LASiS by a nanosecond laser [35]

Both laser fluence and pulse duration time play the crucial role in determining how much heat can be absorbed by the target during the ablation process, thereby controlling the target surface temperature and the corresponding ablation mechanism.[37] The choice of laser wavelength mainly affects the laser energy penetration through the liquid column and the re-absorption by solution-phase colloidal NPs.[54] This, in turn, controls the extent of "re-radiation" of the already-formed NPs in solution, thereby modifying the final sizes and shapes of synthesized NPs. In this regard, shorter laser wavelengths usually bear larger impact on the re-structuring of solution phase NPs due to higher absorption by the particles.[51] On the other hand, the environmental parameters such as solution-phase oxygen content and pH value also influence the composition as well as the shape and size of the synthesized NPs by controlling the solution-phase ion concentration that dictates the nanocrystal growth directions.[56,57] To this end, previous studies by P. Blandin et al. indicated the ability to control size and surface oxidation of crystalline Si-based NPs

by tuning the amount of dissolved oxygen in water during LASiS.[58] On a similar note, previous work by S. C. Singh et al. have also shown that injecting solution phase oxygen during LASiS on Zn reduced the particle size and $Zn(OH)_2$/ZnO ratio but increased the crystallinity of products.[59]

1.1.3 Laser ablation synthesis in solution-galvanic replacement reaction (LASiS-GRR)

Although highly suited for its ability to fabricate controlled nanostructures in the absence of any external chemical reagents and/or, surfactants/ligands, LASiS bears the disadvantages of relatively low productivity and poor control on shape/size and composition.[35,42] Nanoparticles with multi-metal compositions, uniform morphology and narrow size distributions can function as building blocks for constructing alloys with higher order superlattices that show joint properties of individual metal nanoparticles. Hence, we hypothesize that the extreme physicochemical conditions of LASiS,[60] when interfaced with chemical reduction routes such as galvanic replacement reactions (GRR), can initiate unique non-equilibrium thermodynamics and kinetics at the plasma-liquid interface. Such reaction pathways can generate novel nanostructures or, nanocomposites with tailored morphologies, compositions and metastable structures, heretofore not observed while being potentially promising for catalytic performances. To the best of our knowledge, few works have investigated structure-property relations (specifically for catalytic studies) in nanostructured materials emerging from complex plasma interactions/chemical reactions during LASiS.

On the other hand, galvanic replacement reaction (GRR) offers an effective and versatile approach for synthesizing various NMs with the premise that the oxidant has a higher redox potential than the reductant.[61–63] In specific, the conventional GRR process involves the oxidation of one metal that is usually referred as a sacrificial template by another metal salt ion with higher reduction potential. Upon contacting each other in a solution phase, the metal template will be oxidized and then dissolute

in the solution; meanwhile the other metal salt quickly get reduced and plated onto the outer shell of the template, in which case the final product typically keeps the original shape of the first metal template.[64–66] In addition, during the reactivity selected GRR process, the oxidation and dissolution of the template metal atoms preferentially occur at some certain sites/facets due to the difference in kinetic battier and the shielding effect, therefore results in formation of nanostructures with various shapes and structures including hollow, porous, and core-shell structures.[64,67,68] To this end, the motivation of combining LASiS and GRR in tandem arises from the superior ability for GRR to control the size, shape, composition and morphology of the resultant NPs along with the intrinsic charge screening effect provided by LASiS which prevent NPs from forming severe aggregations without the need for additional chemicals including surfactants and stabilizing agents that are potentially harmful for the NP applications.

1.2 Applications of LASiS-GRR for the synthesis of functional NMs

In recent years, increasing demand for sustainable energy has escalated the research on clean, highly efficient and environmentally benign energy conversion and storage technologies.[69–71] Our specific interest for the application of the synthesized NMs in this study lies on the state-of-the-art electrocatalysts and photocatalysts for the proton exchange membrane fuel cells (PEMFCs) and solar fuel cells respectively. The former refers to the $PtCo/CoO_x$ nanocomposites as a bifunctional regenerative alkaline fuel cell catalyst along with Platinum-transition metal nanoalloys (PtM NAs) for acid fuel cell catalyst; while the latter comprises the nanocomposites of Ag/Au NPs embedembedded in different metal oxide matrices that provide localized surface Plasmon resonance (LSPR) effect as absorbance-enhanced photocatalysts. All the aforementioned catalysts are synthesized via our proposed LASiS-GRR technique.

1.2.1 Bifunctional electrocatalysts for oxygen reduction/evolution reactions (ORR/OER) in alkaline fuel cells

Specifically, the regenerative alkaline fuel cell involve two sluggish electrochemical reactions at the cathode, namely, the oxygen reduction reaction (ORR) and oxygen evolution reaction (OER) for discharging and charging process respectively,[71–78], as listed below

$$\text{Discharging (ORR): } O_2 + 2H_2O + 4e^- \rightarrow 4OH^-$$

$$\text{Charging (OER): } 4OH^- - 4e^- \rightarrow O_2 + 2H_2O$$

The whole schematic mechanism is illustrated in the left side of Fig. 1.2. The two reactions are sluggish mainly because of the complicated four electron transfer processes involved that drastically raise the activation energies. As a consequence, in the past decades or so, various nanoparticle (NP) based catalysts have been extensively researched and developed in an effort to efficiently and economically enhance those two reactions.[21,72,73,79–81]

Typically, Pt-based NPs are widely used as efficient catalysts to provide complete four-electron transport pathways with remarkably reduced overpotentials during ORR processes in alkaline fuel cells and other electrochemical systems.[76,79,82–84] However, the high cost and poor stability of Pt under harsh alkaline conditions of electrochemical cells[85] has led to the search for active non-precious metal/metal oxide catalysts that can replace Pt.[72,76,86–88] As a consequence, people have synthesized Pt-M nanoalloys with various atomic structures and morphologies that manifest similar or even better ORR catalytic performances than Pt.[21,79,88–91] The improved activity is attributed to the combination of geometric and electronic effects where the former refers to the shrunken Pt lattice constants while, the latter refers to higher 5d orbital vacancies in the electronic structure of Pt-M alloys.[79,88] Besides, recent years have seen a surge in mixed valence oxides of transition metals with

spinel structures (Co_3O_4, Mn_3O_4, NiO, etc.) as ORR electrocatalysts, which remarkably cut down the price, in spite of their catalytic activities being relatively low and limited only for alkaline ORR catalysis.[72,88,92,93]

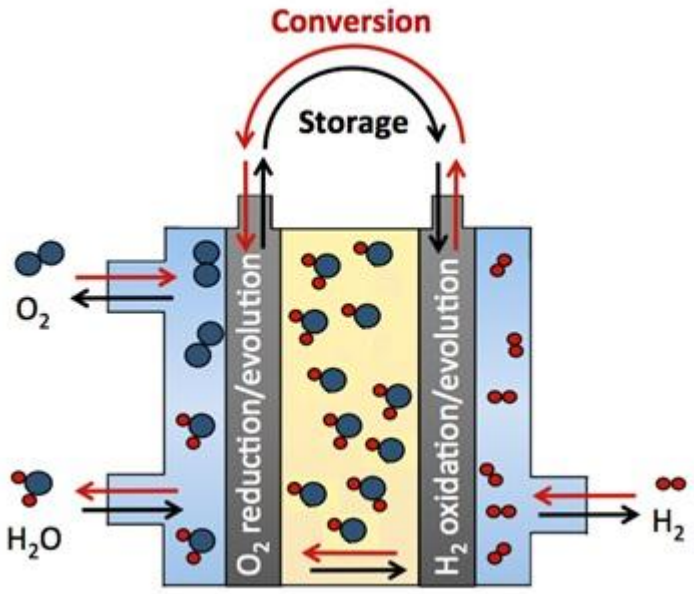


Fig. 1.2 Schematic diagram of a regenerative alkaline fuel cell, cathode and anode correspond to the left and right hand sides respectively.

On the other hand, OER plays a critical role in charge processes in rechargeable fuel cells/batteries (electrochemical OER) or, the water splitting processes during solar fuel fabrication (photochemical OER), which will be discussed latter.[71,80,81,94] It is thus understandable that electrodes in ideal regenerative electrochemical devices should have high conversion rates for both ORR and OER processes. Unlike the ORR systems, transition metal oxides (e.g., CoO_x, NiO_x, TiO_2, IrO_2, etc.) or perovskites are typically considered as excellent catalytic candidates for OER on account of their high activities and good photo-stability.[95–101] Therefore, for alkaline fuel cells, the key challenge in the design of ideal reversible fuel cell is in the low-cost, reproducible synthesis of bi-functional catalysts that can outperform both the ORR and OER activities of commercially available electrocatalysts. A few recent attempts have synthesized designer nanocomposites (NCs) made from the best of both ORR (Pt NPs) and OER catalysts (transition metal oxides) that make use of the synergic “spillover”

effects to influence the adsorption/desorption behavior of intermediate species at the catalyst surfaces, thereby driving the rate determining steps in each of the respective reactions.[102–104]

1.2.2 ORR electrocatalysts for acid proton exchange membrane fuel cells (PEMFCs)

The acid proton exchange membrane fuel cells (PEMFCs) are also known as polymer electrolyte membrane fuel cells, where a polymer membrane such as perfluorosulphonic acid polymer is placed between two Pt impregnated porous electrodes. This membrane has to be resistant to the harsh environment to both anode and cathode sides, while it should have high proton conductivity but must not be permeable to electrons or gases as that will result in the so called "short circuit" or "gas crossover" problems. For electrodes, hydrophobic compound such as TeflonR are coated to form a wet proof coating that interconnects the electrolyte and catalysts for the gas transportation (permeation). To function, H_2 is oxidized into protons at the anode and simultaneously releases electrons that transport through the external circuit to the cathode. The generated protons solvate with water molecules and diffuse through the membrane to react with O_2 while accepting electrons to form water. Similar to the alkaline fuel cell, the energetically expensive oxygen reduction reactions (ORR) at the cathode have been the rate determining step and hence, a severe hindrance to efficient and clean electrochemical energy conversions in acid PEMFCs[90,91,105–109]. In such a case Pt based nanocatalysts have largely been used commercially to promote the ORR activities. However, the cost of precious metal based catalysts added to the lack of stability and durability of Pt under the highly corrosive and acidic conditions of fuel cell operations have prompted a large volume of research in recent years geared towards the development of transition metal based alloys and/or, intermetallic materials with low Pt-loading[108,110–118]. Specifically, recent U.S. DRIVE fuel cell technical roadmap has established the 2020 target for the total loading of Pt group metals (PGM) to be ~0.125 mg/cm^2 electrode area for PEMFC

electrocatalysts[119]. To this end, alloyed nanocatalysts have gained tremendous research interest in the past decade due to their unique geometric and/or electronic characteristics that dramatically enhance their catalytic activities, while reducing the net PGM content[29,120–125]. Alloying Pt with 3-d transition metals such as Co, Ni, Fe, etc have been found to effectively shrink the lattice constant (geometric effect) and downshift the d-band center (electronic effect), resulting in a reduced oxygen binding energy (eV) and consequently improved specific and mass activities for electrocatalyitc ORR processes.[91,121,126–130]

1.2.3 Photocatalysts for light-activated OER/water oxidation: Preliminary studies

As mentioned earlier, photochemical OER is a critical step in the water splitting processes involving artificial photosynthesis for solar fuel production. As illustrated in Fig. 1.3, with appropriate catalysts, solar fuel can be harvested using a photoelectrochemical to achieve sunlight-assisted water splitting that, in turn, produces protons and electrons separated into the conduction and valence bands by band-gap excitations. Such a photoactivated charge separation, under suitably poised redox potentials, can produce hydrogen and oxygen at the cathode and anode of the device respectively. Our current research will facilitate future incorporation of nanocatalysts synthesized via LASiS-GRR into biologically inspired photoelectrochemical cell (see Fig. 1.3) that uses: 1. metal-oxide photocatalysts coupled with Photosystem I (PS I), the photosynthetic protein, to enable sunlight assisted water oxidation at the photoanode (OER/WOC), and 2. non-precious and/or, low precious metal loading intermetallic nanoalloy/nanocomposites (IM NAs/NCs) as electrocatalysts to enable catalytic proton reduction for hydrogen production at the cathode (HER).

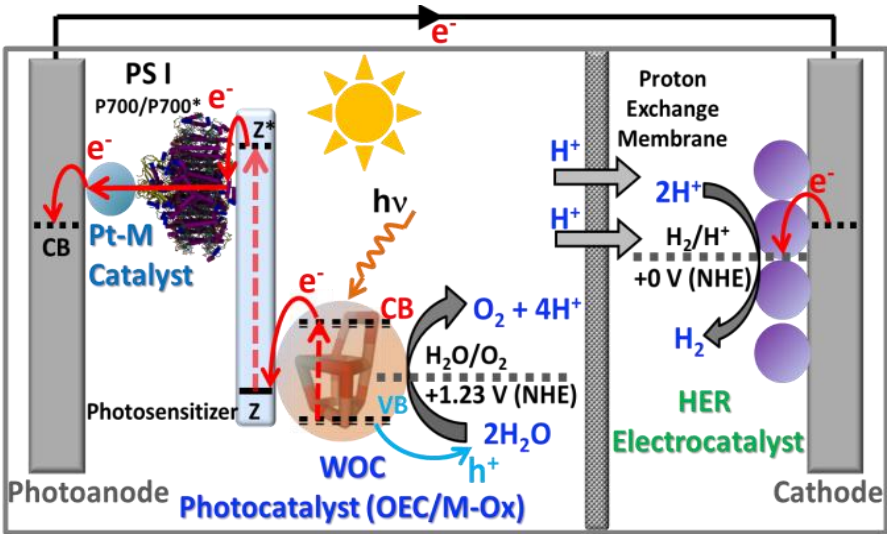


Fig. 1.3 Schematics for the proposed PS I-mediated bio-photoelectrochemical cell using intermetallic (IM) nanoalloy/nanocomposites (NA/NC) as HER electrocatalysts and bio-mimetic metal/metal oxide NC as WOC photocatalysts.

However, photocatalytic OER is a reaction involving a four-electron transfer process that results in a Gibbs free energy increase of 237 kJ mol^{-1}.[131,132] Therefore, for achieving an efficient solar-to-fuel conversion device, finding a robust and highly active catalyst is imperative. Generally speaking, there are two types of photocatalytic water splitting systems, namely, one-step excitation system and two-step excitation system, which is also referred as Z-scheme, as illustrated by Fig. 1.4 (a) and (b) respectively.[132] For one-step phosocatalysts, the band gap of the semiconductor has to straddle the oxidation and reduction potentials for water, i.e., O_2/H_2O, 1.23 V vs. normal hydrogen electrode (NHE) and H^+/H_2, +0 V vs. NHE at pH 0. In most cases, it is extremely challenging for a single semiconducting material to exhibit such a large band gap while absorbing in the visible range of the solar spectra. Alternatively, two catalysts can be connected in tandem with reversible redox shuttles. In such a case reduction of water to hydrogen and oxidation of reduced redox mediators occur on one photocatalyst (referred as p-type catalyst), meanwhile the oxidized redox mediator get reduced on the other catalyst (referred as n-type catalyst) together with oxidation of water to oxygen.

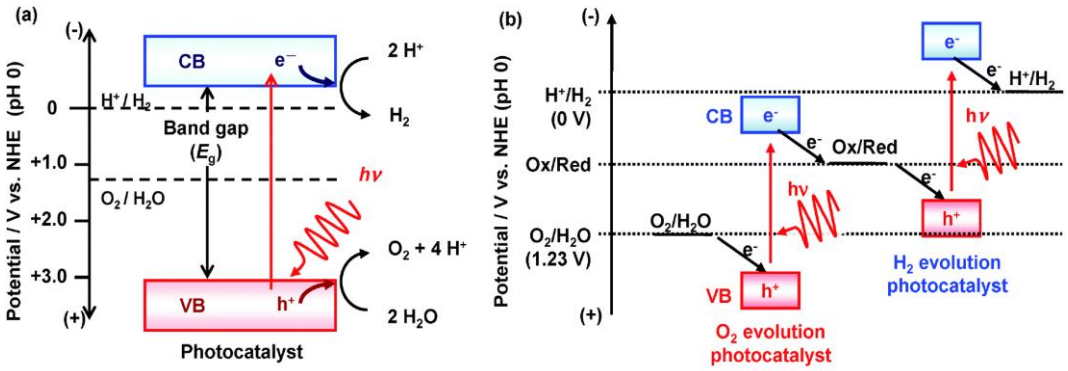


Fig. 1.4 Energy diagrams of phtoocatalytic water splitting based on (**a**) one-step excitation and (**b**) two-step excitation (Z-scheme).[132]

In light of the aforementioned challenges in the rational design of efficient photocatalysts, the current thesis presents some preliminary research on photocatalytic materials that includes efforts towards band-gap and band edge measurements for the catalytic products synthesized through LASiS or LASiS-GRR, thereby revealing the potential application for those NMs in the photocatalytic field, i.e., whether they can be serve as n-type, p-type semiconductor catalyst or can be used in the one-step water-splitting system. The methods for the band gap and edge measurements, known as diffusive reflectance measurement and electrochemical impedance spectroscopy, will be discussed in the experimental part latter.

Another obstacle for efficiently splitting water is the poor harness of visible light by the photocatalysts. For solving this problem, a number of research works have reported utilizing localized surface Plasmon resonance (LSPR) to enhance light absorbance hence improve the efficiency based on the incorporation of the well-known plasmonic materials Ag and Au in photocatalysts.[133–138] Here, the crucial concept for LSPR is that conduction electrons act as a harmonic oscillator in response to an oscillating electric field such as light due to re-distribution of the electron density, which in turn, generate another electric field both inside and outside the metal NP that is opposite to the electric field of the incident light.[139] By incorporation of LSPR effect into the solar fuel system, over 66 folds improvement of the OER efficiency can be achieved.[140]

1.3 Outline of dissertation

This chapter is the overview of the whole project, which entails the background knowledge of the proposed synthesis technique (LASiS-GRR), basic mechanisms, as well as the introduction of the potential applications of the resultant products. Chapter 2 describes the methodologies including the introduction of the in-house designed LASiS-GRR setup along with detailed experimental steps as well as relevant knowledge for each small project, as will be discussed latter from chapter 3-7. Chapter 3 presents the work of LASiS on Co (without GRR) in water with different laser parameters (laser fluence, wavelength, ablation time etc.) and environmental conditions (solution phase oxygen content, pH, ageing time, etc.). The results and experience from these researches will benefit us in the latter LASiS-GRR work for choosing optimized laser/environmental parameters and therefore synthesizing the ideal products. In chapter 4, we carried out the project of LASiS on Co with K_2PtCl_4 salts, which results in the formation of $PtCo/CoO_x$ nanocomposites (NCs) with excellent bifunctional ORR/OER catalytic activities, as is ascribed to the synergic "spillover" effect. In chapter 5, after acid treatment of the products from LASiS on Co with K_2PtCl_4, we obtained PtCo NAs with various alloying degrees and atomic ratios with outstanding ORR catalytic activities in acid. This is contributed by the core-shell structure with a Pt-rich shell and a uniform PtCo alloy core, as demonstrated by electron energy loss spectroscopy (EELS) mapping. Chapter 6 will briefly touch upon future applications of LASiS-GRR towards the synthesis of plasmon coupled photocatalysts and other higher-order intermetallic nanomaterials. To this end, preliminary proofs-of-concept results are presented for the synthesis and characterization of Ag/Au embedded ZnO/TiO_2 NCs with enhanced surface Plasmon resonance (SPR) properties that can have possible applications as photocatalytic materials in future. The effect of laser re-irradiation (RI) on the structural re-arrangements and plasmonic properties of the aforementioned NC materials will also be investigated and discussed. Furthermore, preliminary results for a wide range

of complex binary/ternary intermetallic nanomaterials synthesized under various experimental conditions of LASiS-GRR are also discussed to demonstrate the versatility of the technique.

Chapter 2 Experimental Setup and Methodology

2.1 Description of the LASiS/LASiS-GRR setup

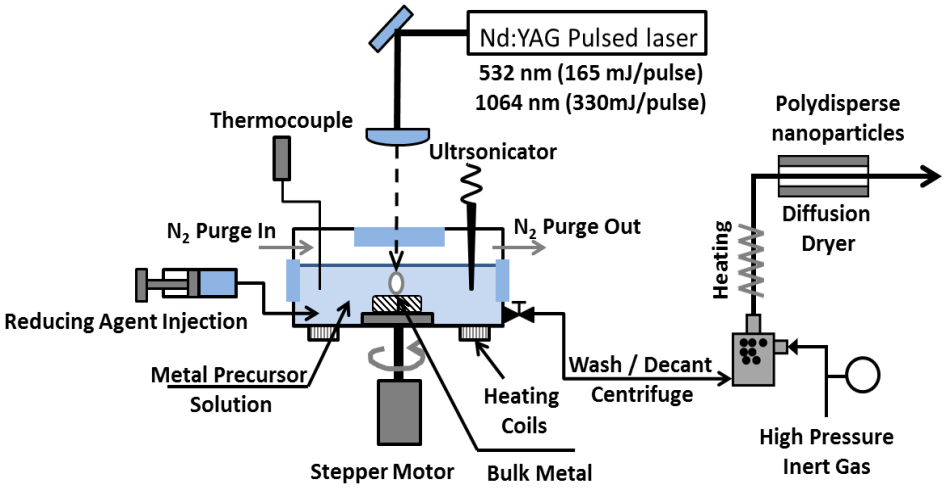


Fig. 2.1 Schematic diagram of the designed multi-functional LASiS setup

The in-house built setup for carrying out LASiS and LASiS-GRR is shown by the schematic in Fig. 2.1, which houses a Q-switched Nd:YAG pulsed laser (Manufacturer: Brilliant Inc.; Model: Brilliant Easy) equipped with 1st and 2nd harmonic generators that provide 532 nm and 1064 nm wavelengths of 165 and 330 mJ/full pulse energy, respectively at 10 Hz repetition rate and 4 ns pulse duration. The laser beam is focused at the surface of a metal target immersed in a desired liquid medium inside a sealed stainless steel reactor cell. In the current design, the laser beam is focused with a convex lens (focal length: 75 mm), and the focused beam passes through a high damage threshold tested laser window on the cell. The cell is provided with four side-viewing windows to accurately view and adjust the laser focal point. A gas inlet and outlet on the cell allows for suitable purging with inert gases. The metal target platform, mounted on a stepper motor, rotates continuously to enable uniform ablation from the surface. The reactor cell is also provided with heating rods along with a thermocouple for accurate monitoring of solution temperature and a sonic dismembrator for in situ de-agglomeration of the synthesized NPs. Additionally,

a programmable injection unit is attached to the cell that allows for simultaneous introduction of metal salt precursor solutions for the tandem LASiS-GRR.

2.2 Sample preparation using LASiS/LASiS-GRR

2.2.1 Synthesis of $CoO_x/Co(OH)_2$

The Co pellets bought from Kurt J. Lesker (99.95% purity, 1/4" diameter×1/4" height) were used as targets, which were covered by 35 ml of de-ionized water (DI-water; Purity = 99.9%; Conductivity = 18.2 MΩ/cm at 25°C) during laser ablation. The distance between the target and water surface was measured to be 5 cm, and the corrected focal length was estimated to be 85 mm upon taking into account the refraction through water. Based on these measurements, the lens to surface distance (LTSD) was accurately determined for both laser wavelengths. For comparison of Co NPs generated via LASiS at different laser fluences, all samples were ablated for 15 min at room temperature. All experiments were conducted with simultaneous ultrasonication. The Co target was rotated by the stepper motor at a speed of 0.3 rpm during ablation (this rotating speed keeps the same for all the laser ablation work in this dissertation). The aging test was conducted in standard ambient temperature and pressure, i.e., 298.15 K and 101 kPa. For O_2 free LASiS, N_2 was purged in water for 30 min before experiments and purged above water surface during experiments. The oxygen concentration in solution measured before and after ablation process is 0.32 mg/L and 0.35 mg/L respectively as compared to the corresponding value of ~5 mg/L for dissolved O_2 at atmospheric pressure in unpurged solution. The small increase of O_2 concentration is attributed to the minor contamination during the measurement using the oxygen meter. The resulting oxygen to NP weight ratio is calculated to be around 1:100. For re-ablation experiments, NP colloids were transferred to a 30 ml vial, and subsequently, ablated with the laser beam being focused at the center of the solution. For NP productivity tests, ablation was carried out for different periods of time using the unfocused laser beam (0.3 J/cm^2 for both 1064 nm and 532 nm laser).

For different pH studies, HCl (Cole-Parmer, 36.5-38%) and KOH (Fisher Scientific, ＞85%) were used as the acid and base reagents for the desired acidic and alkaline conditions. The obtained colloidal solution was centrifuged at 5000 rpm for 15 min and then washed/decanted with DI-water for two times.

2.2.2 Synthesis PtCo/CoO_x NCs

Potassium tetrachloroplatinate (II) (K_2PtCl_4) (>99.9%) were bought from Sigma-Aldrich. All LASiS-GRR experiments were carried out in an in-house built cell equipped with facilities for simultaneous injection of metal salt solutions, temperature control as well as ultrasonication, as depicted in the section 2.1 (Fig. 2.1). For the synthesis of PtCo/CoO_x NCs via tandem LASiS-GRR technique, different amounts of K_2PtCl_4 salts were dissolved in 40 ml of DI-water to produce four different concentrations of K_2PtCl_4 solutions, namely 25, 60, 120 and 250 mg/l. Thereafter, each of the freshly prepared K_2PtCl_4 solution was transferred into the LASiS cell through the injection unit. The Co pellet was then ablated in those K_2PtCl_4 solutions for 20 min. The obtained colloidal solutions were aged for three days under ambient temperature and pressure conditions. Then, the samples were centrifuged at 5000 rpm for 15 min and decanted after washing with DI-water for two times. Both LASiS and tandem LASiS-GRR experiments were carried out at room temperature with simultaneous ultrasonication.

2.2.3 Synthesis of PtCo NAs

For the synthesis of PtCo nanoalloys via tandem LASiS-GRR technique at neutral conditions, four different concentrations of K_2PtCl_4 salt solutions (namely 125, 250, 375 and 500 mg/l) in de-ionized water were used along with the respective ablation times of 4, 7, 13 and 20 min. The ablation times were chosen for ~60% reduction of initial K_2PtCl_4 precursors in each of the cases (as determined from ICP-OES measurements). Thereafter, each of the freshly prepared K_2PtCl_4 solution

was transferred into the LASiS cell through the injection unit, bubbled with N_2 for 30min. The Co pellet was then ablated in those O_2-free K_2PtCl_4 solutions using unfocused 1064 nm laser (330 mJ/pulse, 10 Hz) for various time. Right after ablation, the pH of the produced colloidal solution was adjusted to 2 by adding HCl (1M) followed by aging in darkness for 24 hours. Finally, the PtCo NPs were collected by centrifuging at 4700 rpm for 15 min and decanted after washing with DI-water for two times. For LASiS-GRR at different pH, KOH and HCl were used for preparing the K_2PtCl_4 solutions (250 mg/l) under alkaline (pH=11) and acid (pH=2) conditions respectively. The synthesis and post treatment procedures were the same as followed earlier for the neutral condition case. Besides, all the LASiS-GRR experiments mentioned above were carried out at room temperature with simultaneous probe ultrasonication.

2.2.4 Synthesis of ZnO/TiO_2 embedded by Ag/Au

For the synthesis of Ag/Au embedded ZnO/TiO_2 NCs, 5 mg of $AgNO_3/HAuCl_4$ was first dissolved in 40 ml of water, then transferred into the LASiS cell through the injection unit, bubbled with N_2 for 30 min. The Zn/Ti pellet was then ablated in those O_2-free $AgNO_3/HAuCl_4$ solutions using unfocused 1064 nm laser (330 mJ/pulse, 10 Hz) for 10 min. For synthesizing core-shell TiO_2/Ag NPs, right after ablation, the pH of the produced colloidal solution was adjusted to 2 by adding HNO_3 (1M) followed by aging in darkness for 24 hours and centrifuging at 4700 rpm for 15 min, finally decanted after washing with DI-water for two times.

2.3 Experimental and theoretical characterization techniques

2.3.1 TEM related characterizations

A Zeiss Libra 200MC monochromated transmission electron microscope (TEM) was used with an accelerating voltage of 200 kV for regular TEM characterizations along with selected area electron diffraction (SAED) and high resolution transmission

electron microscopy (HRTEM) imaging. Large-scale and small-scale elemental mappings are obtained from energy dispersive X-ray spectroscopy (EDX) and electron energy-loss spectroscopy (EELS) analysis. Information limitation of HRTEM image is 0.1 nm. Spatial resolution of the STEM image is 0.4 nm. Resolution of EELS spectrum with monochromator is 0.1 eV measured at full width of half maximum (FWHM) of zero-loss peak in the vacuum.

Quantification of Pt:Co ratios of the NPs was performed by fitting the EELS spectrum image. The intensities of the Pt-$N_{2,3}$ edge and Co-$L_{2,3}$ ionization edge were determined after background subtraction with a combination of a power law and a polynomial: $E^{-r} + aE^2 + bE + c$， Here a, b, c and r are fitting parameter, E is energy. The Pt:Co intensity ratio are represented by:

$$\frac{I_{Pt}(\beta,\Delta)}{I_{Co}(\beta,\Delta)} = \frac{N_{Pt}(\beta,\Delta)}{N_{Co}(\beta,\Delta)} \times \frac{\sigma_{Pt}(\beta,\Delta)}{\sigma_{Co}(\beta,\Delta)} \times \frac{I_T}{I_T}. \qquad \text{Eqn. 2.1}$$

Where I is the ionization edge intensity, N is the absolute number of atoms per unit area (areal density), σ is the electron inelastic scattering cross-section, I_T is the total transmitted intensity, β and Δ represents the dependence of collection angle and integration energy window respectively. The I_T is canceled out and β is fixed during EELS spectrum image acquisition. The same Δ was used in the EELS spectrum image quantification. Therefore, Eq.1 can be rewritten to:

$$\frac{I_{Pt}}{I_{Co}} = \frac{N_{Pt}}{N_{Co}} \times \frac{\sigma_{Pt}}{\sigma_{Co}} \qquad \text{Eqn. 2.2}$$

2.3.2 Other physical characterizations

X-ray diffraction (XRD) was carried out on a Phillips X'Pert-Pro diffractometer equipped with a Cu Ka source at 40 kV and 20 mA. The mean crystal sizes of the NAs were calculated according to Scherrer equation:

$$d = \frac{0.9\lambda}{\beta \cos\theta} \qquad \text{Eqn. 2.3}$$

where d is the mean crystal size, λ is wavelength of the X-ray, β is the line broadening at half the maximum intensity (FWHM), θ is the Bragg angle.

The Co atomic fractions in the alloy (x) were evaluated using the Vegard's law,

$$x = [\frac{a - a_0}{a_s - a_0}] \cdot x_s \qquad \text{Eqn. 2.4}$$

where a_o and a_s are the lattice parameters of Pt (0.393 nm) and Pt_3Co (0.383 nm), and x_s is the Co atomic fraction (0.25) in the Pt_3Co catalyst. The degree of alloy, i.e. the alloyed Co (Co_{al}) to total Co in the catalyst (Co_{tot}) ratio can then be expressed by:

$$\frac{Co_{al}}{Co_{tot}} = \frac{xPt_{ICP}}{(1-x)Co_{ICP}} \qquad \text{Eqn. 2.5}$$

where Pt_{ICP} and Co_{ICP} are the integral atomic ratios of Pt and Co from ICP-OES measurements, respectively.

The NP size distributions in aerosol form were collected via scanning mobility particle sizer™ (SMPS™) spectrometer made by TSI Inc. (Model: 3936). The aerosolized NPs were generated using an atomizer operating at 30 psi (g) gas pressure. The sample flow rate and sheath flow rate were set to be 1.5 lpm and 15 lpm respectively. The accuracy of SMPS is reported to be 0.05 nm.

Raman spectra were measured via a Renishaw M1000 micro-Raman spectrometer with 532 nm, 900 μw laser excitation and 120 s acquiring time. Samples for Raman spectra were made by drop casting NP solution on an aluminum foil. The measured Raman shifts were calibrated against a cyclohexane standard.

Inductively coupled plasma optical emission spectroscopy (ICP-OES) (Perkin Elmer, Optima 4300 DV) was used to measure the concentration of NPs. Standard cobalt dichloride solution (≥99%) and K_2PtCl_4 solution (>99.9%) were used for calibration.

UV-Vis absorption measurement (Biotek, Synergy H1) was scanned over the wavelength range of 300nm to 900nm at a scan rate of 2 nm/step.

2.3.3 Electrochemical tests

The rotating disk electrode (RDE) setup was bought from Pine instrument company, LLC, as is shown in Fig. 2.2. A conventional, three-compartment electrochemical cell comprising of a saturated double junction Ag/AgCl electrode as the reference electrode, a glassy carbon RDE with diameter of 5 mm as the working electrode, and a platinum coil as the counter electrode.

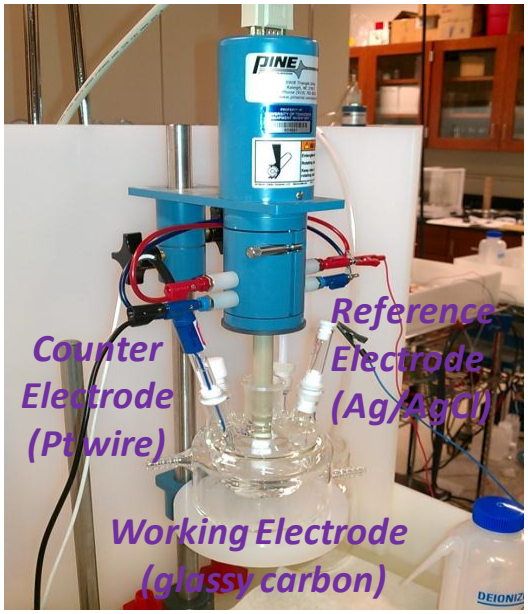


Fig. 2.2 Experimental setup showing the three-compartment rotating disk electrode (RDE) cell (Pine LLC)

For measuring the bifunctional ORR/OER catalytic activities of the PtCo/CoO_x NCs in alkaline conditions, all electrochemistry (EC) tests were carried out at room temperature in 1.0 M KOH solution with the reference electrode calibrated in response to the reversible hydrogen electrode (RHE). 30% Pt/C from BASF was used as the standard catalyst for comparison. For ORR tests, synthesized NPs were first mixed with Vulcan XC-72 carbon black (CB) powder (particle size 20–40 nm, procured from Cabot Company) in aqueous solution with a weight ratio of 1:4 (NP: CB). After 2 hours of ultrasonication, the slurry was stirred for 24 hours and then, completely dried in vacuum at 80 ℃. Thereafter, the catalyst ink was prepared by

suspending 2 mg of the dried mixture in 0.5 mL methanol and 25 μl of 5 wt% Nafion solution (Sigma-Aldrich, density 0.874 g/mL) via 30 mins of ultrasonication. For preparing the working electrode, 6 μL of the prepared catalyst ink was coated on the RDE where the NP loading density was calculated to be 24.5 $\mu g/cm^2$. As for the OER tests, synthesized NPs were deposited on the GCE directly by vacuum drying at room temperature, with a deposition density calculated as 2 $\mu g/cm^2$ for all the catalysts. Linear sweep voltammogram (LSV) for ORR and OER were conducted on the RDE set-up by sweeping the potential from +0.3 to +1.1 V (ORR) and +1.1 to +1.7 V (OER) respectively. For all the experiments, stable voltammogram curves were recorded after scanning for 15 cycles in the corresponding potential regions.

For the measurement of ORR activities of PtCo NAs in acid conditions, all EC tests were carried out at room temperature in 0.1 M $HClO_4$ solution with the reference electrode calibrated in response to the RHE. 20% Pt/C from BASF was used as the standard catalyst for comparison. For ORR tests, synthesized NPs were first mixed with Vulcan XC-72 CB powder (same as in alkaline condition) in aqueous solution with a weight ratio of 1:3 (NP: CB). After 2 hours of ultrasonication, the slurry was stirred for 24 hours and then, completely dried in vacuum at 80 ℃. Thereafter, the catalyst ink was prepared by suspending 2 mg of the dried mixture in 1 mL ethanol and 5 μl of 5 wt% Nafion solution (Sigma-Aldrich, density 0.874 g/mL) via 30 mins of ultrasonication. For preparing the working electrode, rotational drying method was applied, specifically, 10 μL of the prepared catalyst ink was casted on the surface of the GCE that was inversely placed on the RDE setup and rotated at 700 rpm for 5 min. The NP loading density was calculated to be 25 $\mu g/cm^2$. Cyclic voltammetry was conducted over a potential range from +0.05 V to +1.00 V at a scan rate of 50 mV/s after pre-scan the same potential range at 100 mV/s for 50 cycles. The ORR polarization curves were obtained by sweeping the potential from +0.05 to +1.02 V at a scan rate of 5 mV/s and a rotation rate of 1600 rpm.

The electrochemical surface area (ECSA) was determined by the hydrogen desorption area in the CV curve between 0.05 to 0.4 V vs. RHE based on the

following equation:

$$ECSA = \frac{Q_H}{m \times q_H} \quad \text{Eqn. 2.6}$$

where Q_H is the charge for hydrogen desorption, m is the loading amount of metal in the electrode, and q_H is the charge required for monolayer desorption of hydrogen on Pt (210 μC/cm^2).

The dynamics of the electron transfer process in ORR were analyzed through the rotating disk voltammetry (RDV) at different speeds (ranging between 400-2200 rpm) based on the Koutecky-Levich (KL) equation:

$$\frac{1}{J} = \frac{1}{J_K} + \frac{1}{J_L} = \frac{1}{J_K} + \frac{1}{B\omega^{1/2}} \quad \text{Eqn. 2.7}$$

$$J_K = nFkC_0; \quad B = 0.62nFC_0D_0^{2/3}\nu^{-1/6} \quad \text{Eqn. 2.8}$$

where J, J_K and J_L are the measured, kinetic and diffusion limiting current densities respectively, n is the electron transfer number, F is the Faraday constant (96 485 C mol^{-1}), C_o and D_o are the dissolved O_2 concentration the O_2 diffusion coefficient in the electrolyte respectively, ν is the electrode rotation rate in rpm. Tafel plots are generated using the kinetic current J_K as determined from:

$$J_K = \frac{J * J_L}{J_L - J} \quad \text{Eqn. 2.9}$$

2.3.4 Theoretical Modeling of Rate kinetics of LASiS-GRR

For LASiS-GRR on Co in K_2PtCl_4 solution, three main reactions are involved and can be illustrated as:

$$Pt^{2+} + Co_s = Pt_s + Co^{2+} \quad \text{Reaction 1 } (k_1)$$

$$Co_s + 2H^+ = Co^{2+} + H_2 \quad \text{Reaction 2 } (k_2)$$

$$Co + Pt = PtCo(alloy) \quad \text{Reaction 3}$$

For theoretical modeling, reaction 3 can be separated into two chemical processes, namely, Pt-Co bonding formation and Pt-Pt bonding formation, i.e.

$Pt_s + Co_s$ = Pt-Co (bonding process) (k_3)

$Pt_s + Pt_s$ = Pt-Pt (bonding process) (k_4)

Where Pt_s and Co_s represents seeding Pt and Co NPs in solution, k_1, k_2, k_3 and k_4 are the four reaction rate constants respectively. Together with the aforementioned two reactions, the complete reaction rates can be expressed as the following:

$$\frac{d[Pt^{2+}]}{dt} = -k_1[Pt^{2+}][Co_s] \quad \text{Eqn. 2.10}$$

$$\frac{d[Co_s]}{dt} = -k_1[Pt^{2+}][Co_s] - k_2[Co_s][H^+]^2 - k_3[Pt][Co_s] + b \quad \text{Eqn. 2.11}$$

$$\frac{d[Pt_s]}{dt} = k_1[Pt^{2+}][Co_s] - k_3[Pt_s][Co_s] - 2 \times k_4[Pt_s]^2 \quad \text{Eqn. 2.12}$$

$$\frac{d[Co^{2+}]}{dt} = k_1[Pt^{2+}][Co_s] + k_2[Co_s][H^+]^2 \quad \text{Eqn. 2.13}$$

$$\frac{d[Pt-Co]}{dt} = k_3[Pt_s][Co_s] \quad \text{Eqn. 2.14}$$

$$\frac{d[Pt-Pt]}{dt} = k_4[Pt_s][Pt_s] \quad \text{Eqn. 2.15}$$

where b is the production rate of seeding Co from laser ablation. Therefore, the above three equations form a non-linear differential equation set with known initial values, which can be solved using the Runge-Kutta method. The simulation results will be fitted by the experimental data so as to back calculate the four reaction rate constants. Such a simulation can reveal the relationship between the alloying ratio of Pt:Co and the initial values of $[Pt^{2+}]$, $[H^+]$, b. Such rate kinetics simulation will benefit the mechanism study as well as our future work of LASiS-GRR with continuous supply of K_2PtCl_4 salt. In future, the reaction pathways and rate constants developed from the current reaction modeling would help in the development of kinetic Monte-Carlo (KMC)-based simulations to model the nucleation of metal NPs from LASiS-GRR techniques.

2.3.5 DFT calculation

Density functional theory (DFT) is so far the most successful model to simulate the electronic structure of a matter, including atoms, molecules to nuclei, quantum and classical fluids. Such a computational simulation provides an effective route for the prediction of molecular structures, vibrational frequencies, ionization energies, electric and even reaction paths, etc. Generally speaking, DFT simplifies a system with many interacting electrons to a set of noninteracting electrons under an external potential, as shown by the Kohn-Sham (KS) equations[141,142]:

$$E[\rho(r)] = T_s[\rho(r)] + V_{e-nuc}[\rho(r)] + V_{e-e}[\rho(r)] + E_{xc}[\rho(r)] \qquad \text{Eqn. 2.16}$$

where $T_s[\rho(r)]$ is the kinetic energy, $V_{e\text{-}nuc}[\rho(r)]$ and $V_{e\text{-}e}[\rho(r)]$ are the Hartree energies which describe the electron to nuclear and electron to electron interaction respectively. $E_{xc}[\rho(r)]$ is the exchange-correlation energy, indicating the difference between the exact and non-interacting kinetic energies as well as the non-classical contribution to the electron-electron interactions. Two main types of exchange-correlation functionals are usually used in DFT simulation, namely, the local density approximation (LDA) and the generalized gradient approximation (GGA). The exchange-correlation functional we are using in our simulation is the RPBE functional within the GGA category.

For studying the current ORR activity, the basic mechanism established using DFT calculation is illustrated as the following[141,142]:

$$\frac{1}{2}O_2 + * \rightarrow O* \qquad \text{Eqn. 2.17}$$

$$O* + H^+ + e^- \rightarrow HO* \qquad \text{Eqn. 2.18}$$

$$HO* + H^+ + e^- \rightarrow H_2O + * \qquad \text{Eqn. 2.19}$$

where * denote a site on the surface. By constructing a (3×2) three-layer fcc (111) slab for the unit cell of the interested catalyst, the internal energies before and after oxygen and hydroxide adsorption can be calculated. Therefore the activation energies (activation barriers) for the above three steps can be calculated accordingly. Thereafter, the rate-determining step can be found for calculating the catalytic activities.

Chapter 3 Synthesis of nanostructured oxides and hydroxides of cobalt using laser ablation synthesis in solution (LASiS)

3.1 Introduction

In general, there are two oxidation states for cobalt oxide (CoO_x) NPs, namely cobalt (II) monoxide (CoO) and cobaltosic (II,III) oxide (Co_3O_4), both have attracted significant interest in the research community as one of the most promising earth-abundant transition metal oxides with catalytic activities towards water oxidation (photocatalysis), carbon monoxide (CO) oxidation, toluene oxidation, hydrogen evolution, etc.[1,5,76,143–146] Our specific interest in CoO_x NPs stems from their application as photocatalysts for solar water-splitting in an effort to mimic the photosynthetic systems.[1,5,147,148] On the other hand, β-cobalt hydroxide (β-$Co(OH)_2$), an intermediate en route to Co_3O_4 formation, has high energy density and bears great potential for its use as electronic capacitors and electrode materials in Li-Ion batteries.[7,149,150] Previous studies have reported chemical routes for the synthesis of CoO_x NPs[18,143,145,151–153] and β-$Co(OH)_2$ nanocrystals[154,155] of various sizes and shapes. However, such synthesis routes inevitably leave unwanted chemicals including surfactants, leftover reducing agents and different kinds of by-products on the catalyst surface that dramatically retard their performances.[32,33]

In recent years, laser ablation techniques have been successfully utilized to synthesize Co_3O_4 NPs that indicate higher catalytic activities for water oxidation, as compared to the ones synthesized via wet chemical techniques. Such enhancement in catalytic activities is mainly attributed to the green synthesis route of LASiS that prevents any surface contamination from excess chemicals. However, few studies

have explored in details the role of experimental and laser parameters in fine-tuning the laser ablation mechanism to enable systematic tailoring of the shape, structure and chemical composition of CoO_x/β-$Co(OH)_2$ NPs synthesized via LASiS.

The present study uses an in-house designed LASiS setup to investigate the capabilities of LASiS to synthesize CoO_x/β-$Co(OH)_2$ nanostructures with tailored size, morphology and composition by tuning various solution-phase experimental as well as laser parameters. Specifically, the role of laser wavelengths (1064 and 532 nm), laser fluences, aging time, ablation time, oxygen content and pH conditions in solution are systematically studied to provide a detailed mechanistic picture behind the controlled synthesis of various nanostructures using LASiS.

3.2 Results and discussion

3.2.1 Chemical pathway for the products during LASiS on Co

The products from LASiS (532 nm laser) on Co with different aging time and dissolved oxygen amount were first investigated. TEM images and corresponding selected area electron diffraction (SAED) patterns for fresh and aged NPs produced via LASiS on cobalt (shown in Fig. 3.1) indicate large networks of heavily coalesced nanostructures for freshly synthesized products, as seen from Fig. 3.1 (a). Corresponding SAED pattern in Fig. 3.1 (c) exhibits four diffraction rings with diameters of 8.1, 9.39, 13.3, and 15.4 (1/nm) that agrees well with the (111), (200), (220) and (311) lattice planes of cobalt monoxide (CoO) (JCPDS #43-1004), as indicated in Table 3.1 comparing the transformed d-spacings with the respective standard values. However, after three days of ageing, the aforementioned nanostructures transform into dendritic agglomerates of spherical NPs (Fig. 3.1 (b)). The respective SAED patterns indicate the diffraction rings for CoO to evolve into those for cobaltosic oxide (Co_3O_4) (JCPDS #43-1003), as demonstrated in Fig. 3.1 (d) and Table 1. The above phenomena indicate that LASiS on Co initially produces CoO that, over a period of time, further oxidizes to Co_3O_4 in the colloidal solution. These

results reveal the chemical pathway for the formation of Co_3O_4 via intermediate oxidization states during LASiS, as expected under extreme temperature conditions (>1000 ^oC) and is contrary to the commonly reported Co_3O_4 as the direct product of LASiS on Co.[5] The findings are further confirmed by the respective d-spacings from HRTEM images in Fig. 3.2 (a) and (b) as well as Raman spectra in Fig. 3.2 (c) and (d), where the two main peaks for Raman shifts at ~693 cm^{-1} and ~484 cm^{-1} correspond to the Raman active modes (E_g and A_{1g}) for Co(II, III)O_x.. Specifically, the peak at ~523 cm^{-1} is assigned to Raman active mode of A_{2g}, a distinctive peak for Co_3O_4,[156] as also supported by standard Raman spectra for CoO and Co_3O_4[60]. The obvious A_{2g} peak at 524 cm^{-1} in Fig. 3.2 (d) indicates the strong presence of Co_3O_4 in the sample aged for three days as compared to a weak presence of the peak in Fig. 3.2 (c). The two small peaks for typical Co_3O_4 sample missing at 197 nm and 624 nm for the aged sample in Fig. 3.2 (d) is possibly due to the low sample deposition amount. Bearing in mind that the standard Raman spectra is for bulk Co_3O_4 samples, the signal intensities for the 197 nm and 624 nm spectral lines most probably have been too small to be detected above the background noise in the spectral profile. For all those characterizations, the presence of a small portion of Co_3O_4 NPs for the fresh sample can possibly be a result of some oxidation during sample deposition.

Table 3.1 Comparison of standard and experimental d-spacing calculated from SAED

Standard d-spacing (Å)		**Experimental d-spacing (Å)**	
CoO	Co_3O_4	Fresh sample	Aged for three days
	2.86 (220)		2.85
2.46 (111)	2.44 (311)	2.47	2.43
2.13 (200)	2.02 (400)	2.13	2.01
1.51 (220)	1.56 (333)	1.50	1.56
1.29 (311)	1.43 (440)	1.30	1.43

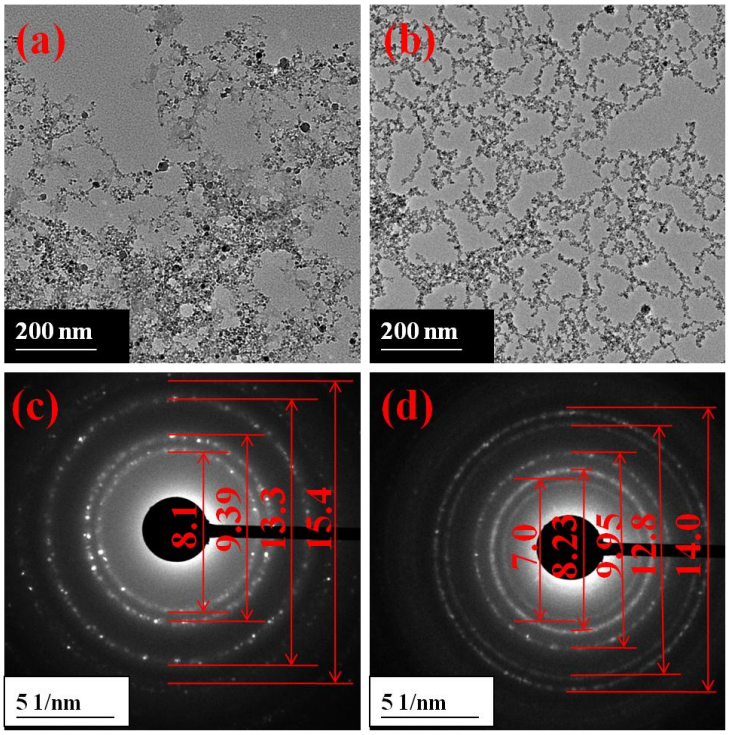


Fig. 3.1 TEM images **(top)** and the corresponding SAED patterns **(bottom)** showing evolution of CoO_x NPs from LASiS by 532 nm laser at 1 J/cm^2: **(a), (c)** fresh sample; **(b), (d)** aged for three days.

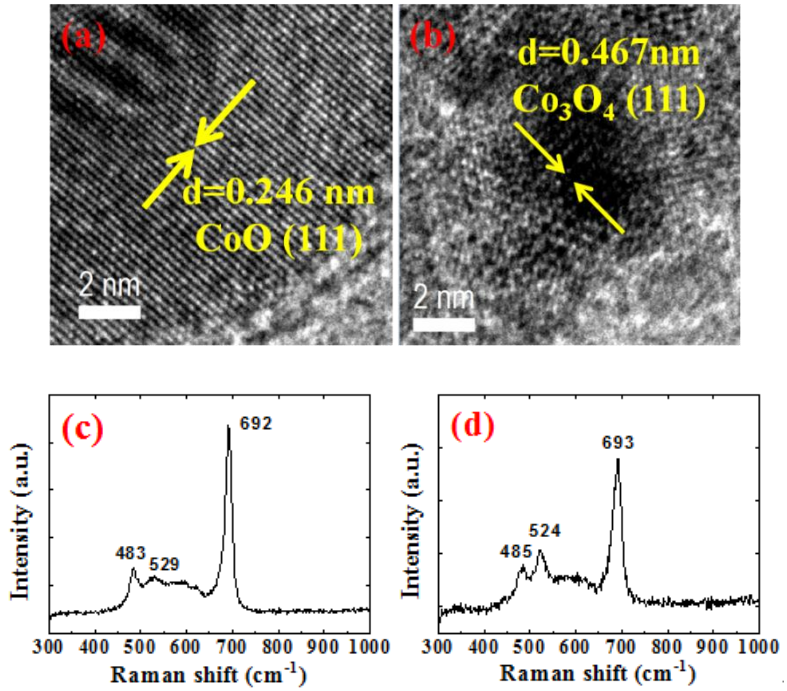


Fig. 3.2 **(a), (b)** HRTEM images, and **(c), (d)** Raman spectra for CoO_x NPs prepared by 532 nm laser at laser fluence of 1 J/cm^2; **(a), (c)** fresh sample; **(b), (d)** aged for three days.

It needs to be highlighted here that the aforementioned syntheses were carried out in aqueous solutions containing O_2. In order to investigate the role of dissolved O_2 on CoO_x NP formation during LASiS, control experiments were carried out in O_2 free DI-water by purging N_2 throughout the experiment. The results, as seen from dark field images of scanning mode TEM (STEM) in Fig. 3.3 (a), exhibit the formation of much larger hexagonal sheets (50-400 nm in diameter) that are confirmed to be single crystal β-$Co(OH)_2$ (JCPDS #30-0443) NPs from SAED and HRTEM analyses, as indicated in Fig. 3.3 (b) and (c). Again, the presence of a small amount of Co_3O_4 NPs in these images is suspected to arise due to oxidation during TEM sample preparations. The formation of this metastable β-$Co(OH)_2$ intermediate is primarily ascribed to the lack of O_2 in water that promotes the reaction pathway between ablated Co^{2+} ions and OH^- from water. However, after aging for three days, all the metastable β-$Co(OH)_2$ single crystals get fully oxidized into stable Co_3O_4 NPs in the colloidal solution, as indicated by the SAED patterns in Fig. 3.3 (d).

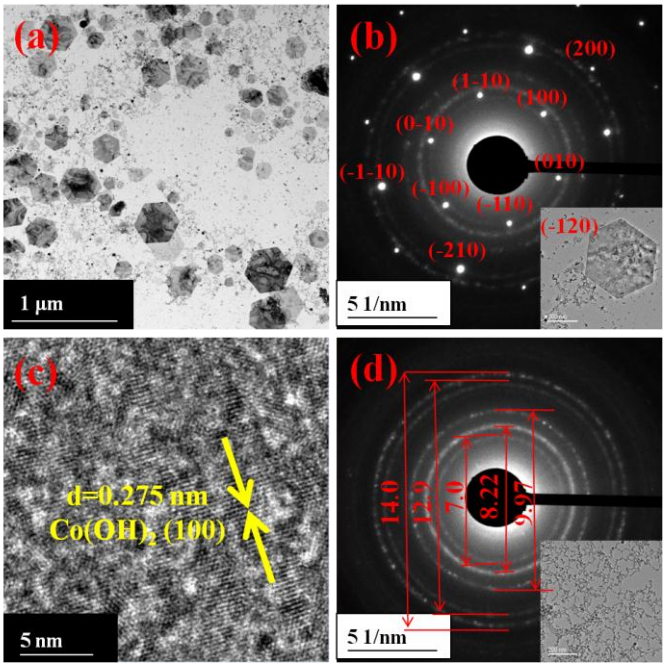


Fig. 3.3 **(a), (b), (c)**: Freshly prepared NPs from LASiS by 532 nm laser (1 J/cm^2) with N_2 purge; **(a)** Bright field STEM image; **(b)** SAED pattern indicating single crystal β-$Co(OH)_2$ NP on <001> zone axis (Inset: corresponding TEM image); **(c)** HRTEM image for β-$Co(OH)_2$ crystal showing the lattice d-spacing; **(d)** SAED pattern of the sample aged for three days indicating Co_3O_4 NPs.

The chemical pathways, depicted schematically in Fig. 3.4, for the products evolution during LASiS on Co is believed to initiate the formation of two metastable reaction intermediates, i.e., CoO and β-$Co(OH)_2$, in the presence and absence of dissolved O_2 in the aqueous solution respectively. The formation of the intermediate Co^{2+} oxidation state can be ascribed to the ultrafast quenching rate due to the extreme temperature differences between plasma plume and liquid environment that initiates the partially oxidized and metastable crystallization states. Consequently, both intermediates transform to the final product of Co_3O_4 NPs through direct oxidation and/or thermal decomposition during the ageing process in aqueous solutions even at standard ambient conditions. The chemical pathways discussed above also apply to the 1064 nm laser, as can be seen in our published paper [60].

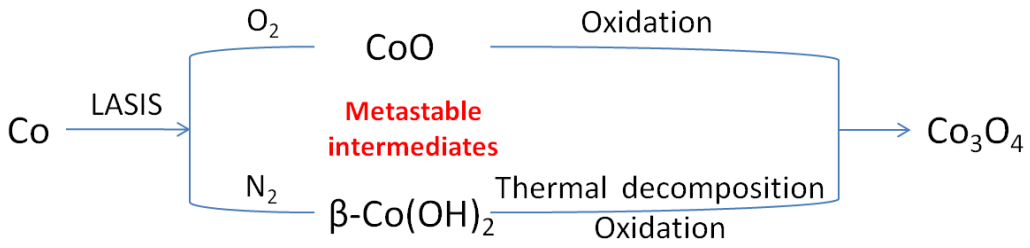


Fig. 3.4 Chemical pathway for the formation of Co_3O_4 NPs via LASiS on Co with/without dissolved O_2.

3.2.2 Effect of laser parameters during LASiS on Co

A detailed investigation on the evolution of final products during LASiS on Co is presented for two laser wavelengths (1064 nm and 532 nm) and diffferent laser fluences through TEM images and PSD data in Fig. 3.5 and 3.6. The results presented here are for the final products of Co_3O_4 NPs after the ageing process. It is observed that ablation with 1064 nm laser at low fluence (0.9 J/cm^2) produces sparsely distributed NPs that have smaller sizes but irregular shapes. Corresponding particle size distribution (PSD) data from SMPS measurements on the aerosolized colloidal suspensions of NPs indicate a bimodal distribution with the dominant peak at ~8 nm

and a secondary minor peak at ~30 nm, as seen from Fig. 3.5 (d). The observed size and morphology characteristics are indicative of vaporization and normal boiling as the dominant ablation mechanism, as explained later. In contrast, higher fluence (41 and 107 J/cm^2) ablation generates large concentration of agglomerates (Fig. 3.5 (b) and (c)) that comprises of spherical NPs with mono-modal size distribution (median size ~12 and 14 nm respectively). The respective PSDs in Fig. 3.5 (e) and (f) corroborate these observations by indicating the bimodal peaks being replaced by mono-modal peaks.

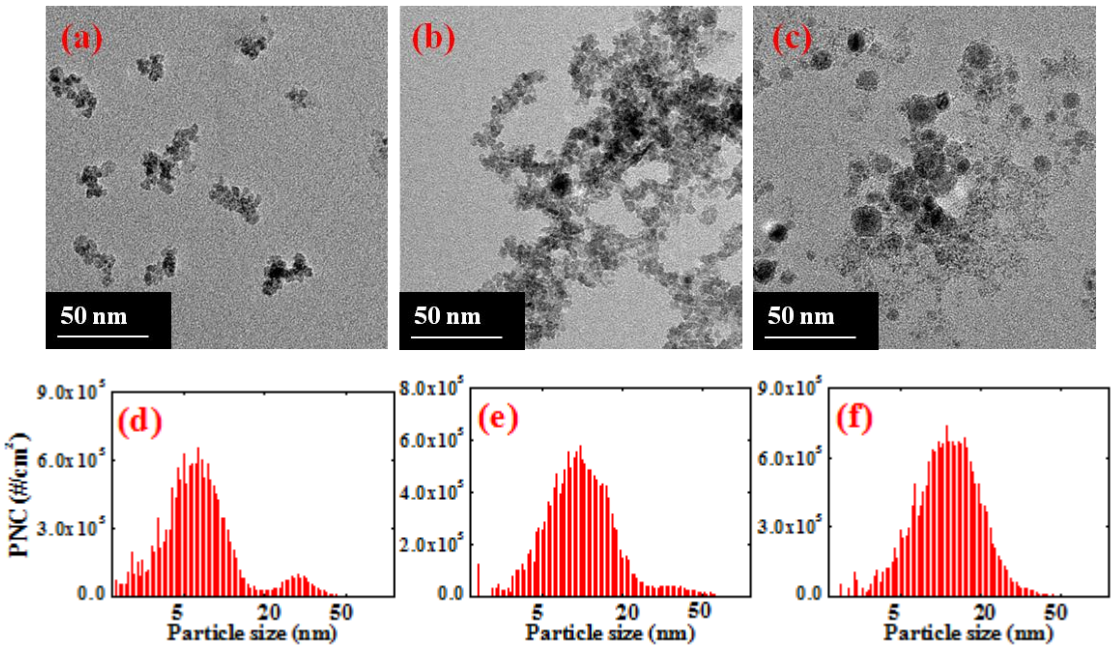


Fig. 3.5 TEM images **(top)** and particle size distributions (PSD) **(bottom)** for 1064 nm laser ablated Co_3O_4 NPs at different laser fluences: **(a), (d)** 0.9 J/cm^2; **(b), (e)** 41 J/cm^2; **(c), (f)** 107 J/cm^2. The vertical axis of PSD shows the particle number concentration (PNC).

LASiS with 532 nm laser exhibit similar trends in NP morphology as observed for 1064 nm laser (TEM images in Fig. 3.6 (a)–(c)) except that the low laser fluence ablation generates dendritic NPs, as shown by Fig. 3.6 (a). The formation of dendritic NPs can probably be explained by the higher absorbance of 532 nm laser as compared to that of 1064 nm laser which promote extensive re-ablation and restructuring

leading to neck formations among the already formed colloidal CoO_x NPs in the solution. The higher absorbance level of 532 nm is also indicated by UV-Vis spectroscopy data in the supporting documents and will be discussed later. Furthermore, the corresponding PSD data for 532 nm indicates a familiar shift, as observed in earlier 1064 nm case studies, from bimodal to mono-modal distribution upon transitioning from low (1 J/cm^2) to high (43 and 114 J/cm^2) laser fluence cases respectively, as seen from Fig. 3.6 (d)-(f). The only observable difference in this case is that the NPs produced by 532 nm LASiS exhibits a higher average particle size (~13–22 nm) than the ones synthesized with 1064 nm laser (~10–14 nm). A possible explanation for the larger average particle sizes in this case is the coalescence and restructuring resulting from the re-ablation of already formed colloidal NPs by the highly absorptive 532 nm laser.

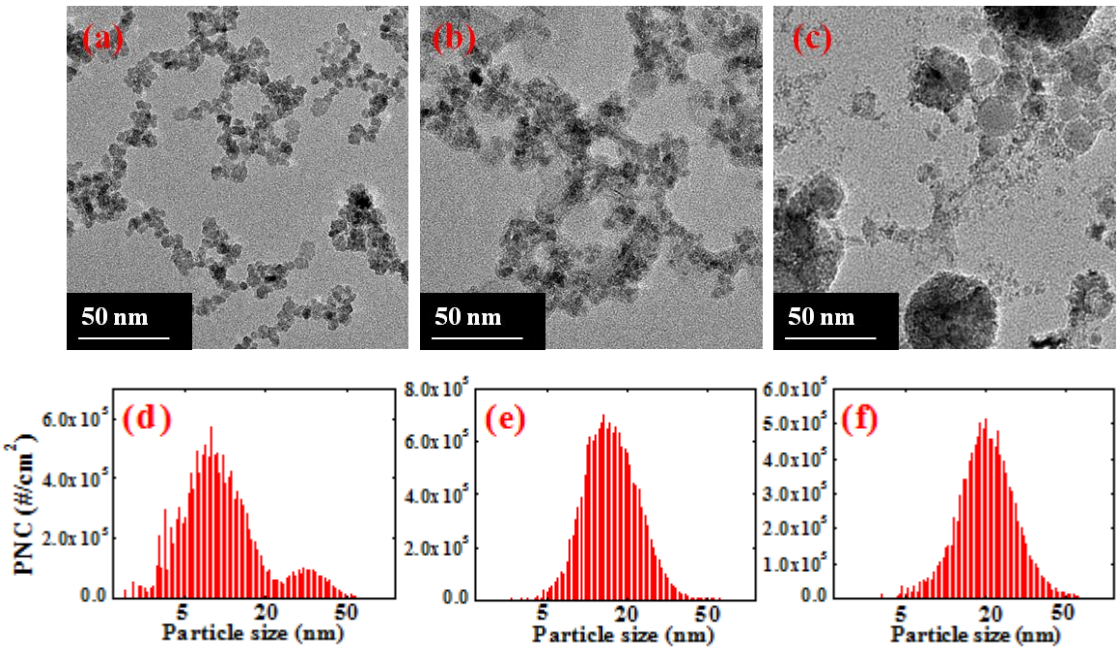


Fig. 3.6 TEM images **(top)** and particle size distributions (PSD) **(bottom)** for 532 nm laser ablated Co_3O_4 NPs at different laser fluences: **(a), (d)** 1.0 J/cm^2; **(b), (e)** 43 J/cm^2; **(c), (f)** 114 J/cm^2. The vertical axis of PSD shows the particle number concentration (PNC).

The aforementioned results are believed to be mainly consequences of the different ablation mechanisms. The commonly observed shifts in the PSDs from

bi-modal to mono-modal peaks for low to high laser fluences, as reported above for 532 and 1064 nm LASiS cases, is possibly related to the onset of the more efficient explosive boiling as the ablation mechanism at higher laser energy. To be more specific, it is observed that during low fluence ablation, small bubbles form on the surface of the Co target, but the ablation process does not affect the bulk of the water body. This indicates vaporization and normal boiling as the two dominant ablation mechanisms under low laser fluence, wherein the nucleation of NPs are partly initiated by electron-phonon coupling within the plasma plume. This process largely produces charged NPs that do not undergo much aggregation and growth due to electrostatic repulsion.[35] At higher laser fluence, the dominant and more efficient explosive boiling generate much higher thermal energy in the plasma plume, as also physically observed by the drastic splashing of water around the laser beam accompanied by audible percussions. We believe that such high energy processes promote aggregation and coalescence that result in the mono-modal distribution of the primary NPs, as indicated earlier.

Furthermore, calculated NP productivity per unit ablation area from ICP-OES measurement on NPs synthesized from LASiS using 1064 nm and 532 nm lasers, are compared in Fig. 3.7 (a). The NP generation increases with laser fluence up to a critical value of ~ 20-40 J/cm^2, beyond which the productivity of NPs starts to decrease for both 1064 nm and 532 nm lasers. The initial increase at low laser fluence is due to the transfer in ablation mechanism from vaporization and normal boiling to the more effective explosive boiling. However, any further increase of the laser fluence induces secondary plasma at the liquid air interface which self-absorbs much of the laser power, thereby weakening the amount of energy that finally reaches the metal target.[37] In order to confirm this phenomenon, focused laser energy reaching the target after penetrating through an equivalent column of water was measured using a power meter. The results, as seen from Fig. 3.7 (b), reveal that the laser energy reaching the target surface indeed starts diminishing beyond a laser fluence of ~30 J/cm^2, which corresponds to the laser fluence of peak productivity in Fig. 3.7 (a).

However, the percentage of penetrated energy over the original laser energy starts decreasing at even lower fluence (~15-20 J/cm^2). These measurements clearly support the explanation for the onset of self-absorption of laser energy by secondary plasma at liquid-air interface beyond the laser fluence of ~15-20 J/cm^2.

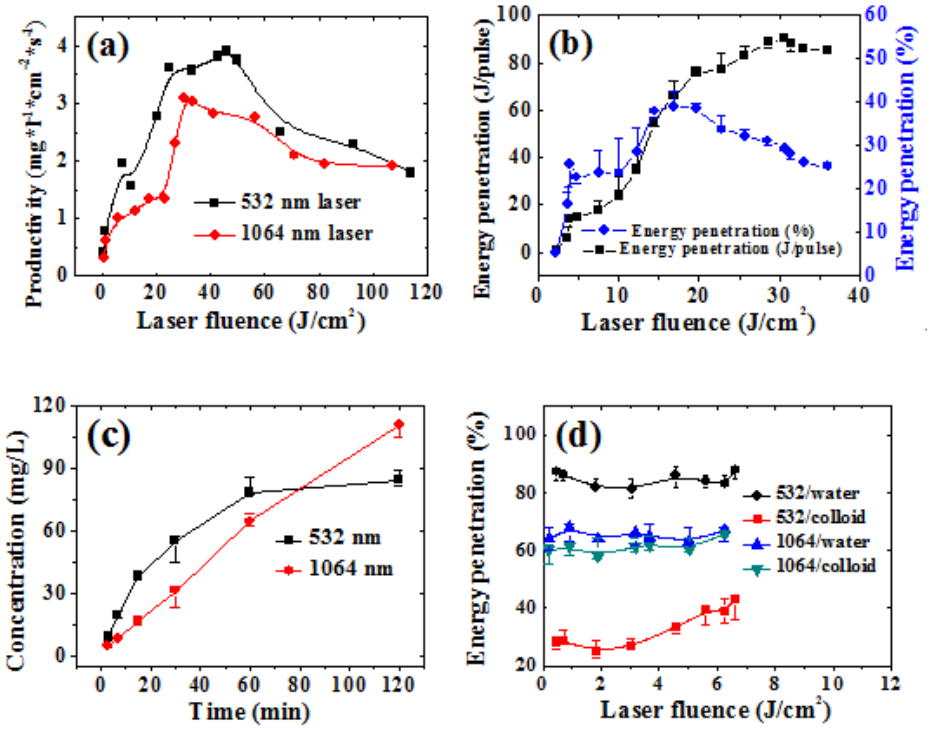


Fig. 3.7 **(a)** Specific area productivity of Co_3O_4 NPs per unit ablation time; **(b)** Focused laser energy (1064 nm) penetration (%) through a glass of DI-water at different laser fluences, where energy penetration (%) is the ratio of penetrated laser energy over the original laser energy; **(c)** NP concentration evolution in time for low laser fluence case of ~0.3 J/cm^2. **(d)** Unfocused laser energy (1064 nm and 532 nm) penetration (%), through Co_3O_4 colloid as well as an equivalent column of DI-water.

In relation to productivity, Fig. 3.7 (a) also indicates that at any laser fluence, 532 nm laser promotes a relatively higher ablation efficiency than 1064 nm laser. This is in agreement with previous studies indicating that LASiS with smaller wavelength lasers have a greater ability to ablate metal sub-surfaces, thereby providing higher ablation efficiency.[35] Here, it needs to be noted that the results are only for the first 15 minutes of ablation. For a detailed investigation on the effects of laser wavelengths on the ablation efficiency, NP concentrations are measured over longer periods of

ablation time. The results, as shown in Fig. 3.7 (c), clearly demonstrate that the 532 nm laser produces higher NP concentration and larger ablation efficiency than 1064 nm laser during the first hour, which is in accordance with Fig. 3.7 (a). However, while LASiS with 1064 nm laser exhibits a continuous linear increase in NP concentration in time, LASiS with 532 nm laser indicates an increase in NP concentration up till an upper limiting value of ~80 mg/l, beyond which it plateaus off. Hence, continued ablation for two hours led to a distinctly higher concentration of NPs produced by 1064 nm laser as compared to those produced by the 532 nm laser. These results also corroborate our earlier theory that the high absorption of 532 nm laser by the suspended Co_3O_4 NPs in solution can significantly retard the ablation process.

A detailed investigation of the physics behind the aforementioned observations is presented in Fig. 3.7 (d), indicating a comparison for the percentage of unfocused laser energy that penetrates through the colloidal suspension of CoO_x NPs in solution as well as an equivalent amount of DI-water for both 1064 nm and 532 nm lasers. The results indicate that for 1064 nm laser, ~65% of the original beam energy penetrates through the DI-water, as compared to ~85% of the beam energy that penetrates for 532 nm laser. The greater energy penetration (%) for 532 nm laser in water is mainly due to its higher photon energy, while a large amount of the 1064 nm laser energy is lost in thermal heating of the water. In contrast, for laser beams passing through colloidal solutions, the laser energy penetration (%) for 1064 nm laser barely changes as compared to only 30-40% of the 532 nm laser energy that reaches the target through the colloidal solution. These observations further demonstrate the higher absorbance of 532 nm laser by the colloidal NPs than that for 1064 nm laser. Such phenomenon can be attributed to the higher photon energy in 532 nm laser that is able to overcome the band gap barrier for electronic excitations in the colloidal NPs thereby accounting for the absorbance energy loss.

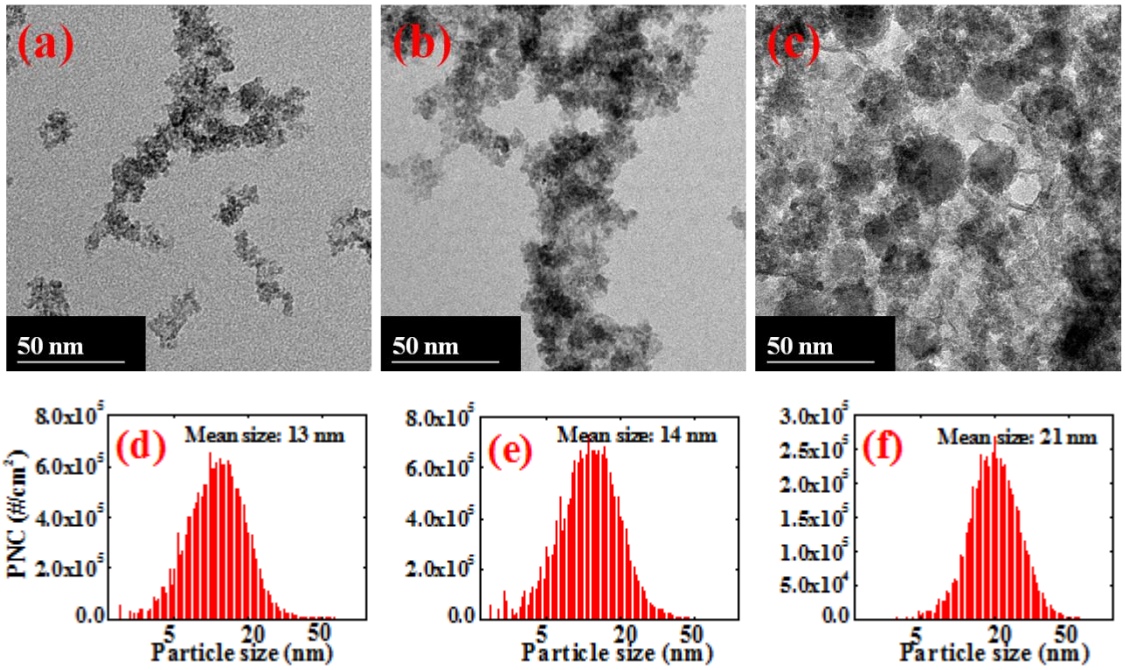


Fig. 3.8 TEM images showing: **(a)** the original NPs generated by LASiS and the alterations in their sizes and shapes after re-ablation (laser energy of 170 mJ/pulse) with: **(b)** 1064 nm laser and **(c)** 532 nm laser; **(d)-(f)** indicate PSDs corresponding to the samples shown in **(a)**, **(b)**, and **(c)** respectively.

The mechanistic picture behind the effect of the re-ablation process due to the enhanced absorbance of 532 nm laser by colloidal NP suspensions is revealed through a series of re-ablation experiments conducted using 1064 nm and 532 nm lasers on identical NP solution samples. The results as shown by TEM images in Fig. 3.8 (a)-(c), compares the TEM image of an original LASiS generated NP sample in Fig. 3.8 (a) with TEM images of the same sample after 15 min of re-ablation using 1064 nm and 532 nm lasers, as seen from Fig. 3.8 (b) and (c) respectively. The TEM images along with the corresponding size distributions in Fig. 3.8 (d)-(f) collected from SMPS measurements, indicate that re-ablation by 532 nm laser generates spherical NPs with increased sizes (see Fig. 3.8 (c) and (f)). In contrast, colloidal NPs re-ablated by 1064 nm laser exhibit similar shape (Fig. 3.8 (b)) and size distributions (Fig. 3.8 (e)) as the ones in the original sample (Fig. 3.8 (a) and (d)). These observations are in accordance with our average size comparison results (Table 3.2), and agree well with our earlier hypothesis that re-ablation by the more absorptive 532 nm laser can

restructure and coalesce the colloidal NPs into uniform spherical shapes, thereby increasing the peak NP sizes while weakening the primary ablation at the target surface. Such processes lower the overall productivity of NPs, but promote the restructuring of solution phase NPs into more uniform size and shapes.

Table 3.2 Comparison of mean sizes and geometric standard deviations (GSD) of synthesized Co_3O_4 NPs under different laser fluence.

1064 nm laser			**532 nm laser**		
Fluence (J/cm^2)	Mean size (nm)	GSD	Fluence (J/cm^2)	Mean size (nm)	GSD
0.9	10.2	1.38	1	13.1	1.47
41	12.1	1.45	43	16.5	1.41
107	14.3	1.46	114	21.56	1.4

3.2.3 Effect of solution-phase pH during LASiS on Co

In this final section, the effect of solution phase protonation on the ablation mechanism is studied by carrying out LASiS on Co target at different pH values of pH=7, pH=13 and pH=14 respectively. TEM images in Fig. 3.9 indicate that unlike the regular dendritic Co_3O_4 NPs formed at pH=7 (Fig. 3.9 (a)), the alkaline condition of pH=13 produces a large amount of Co_3O_4 nanorods (NRs) with average diameter of ~5 nm and length of ~100-200 nm (Fig. 3.9 (b)). Upon increasing the alkalinity to pH=14, the average diameter of the NRs increases to ~15 nm while keeping the similar length (Fig. 3.9 (c)). The corresponding HRTEM images and SAED patterns, as shown in Fig. 3.9 (d) and (e), demonstrate that both the NR structures at pH = 13 and 14 are composed of pure Co_3O_4, with (111) surface (d=0.466 nm) exposed to the surface.

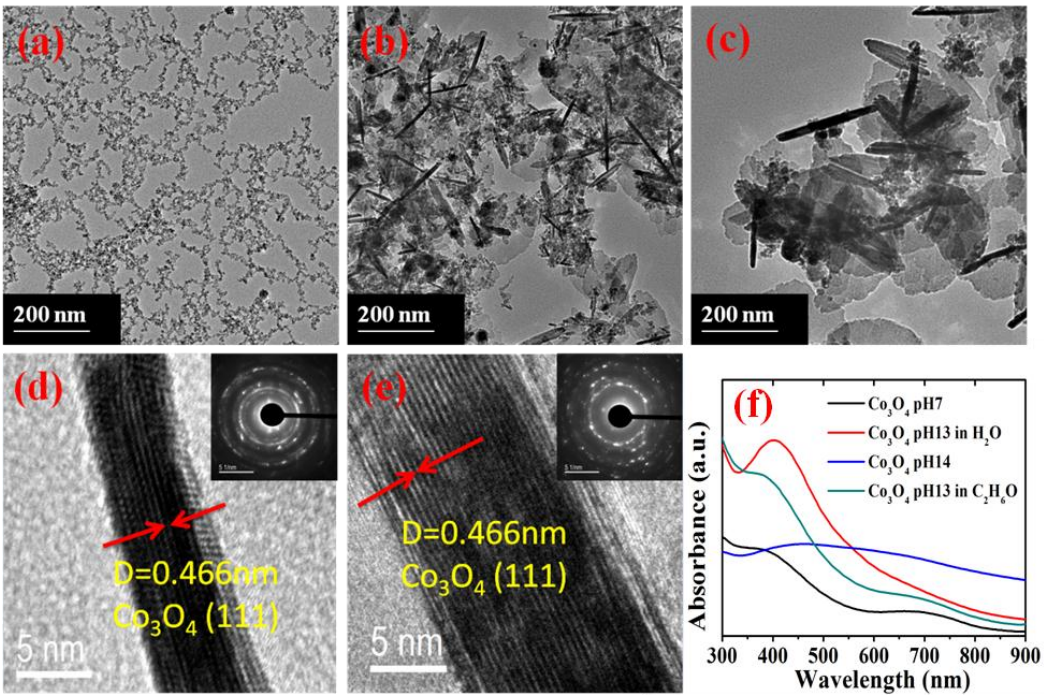


Fig. 3.9 **(a)-(c)** TEM images of Co_3O_4 NPs obtained from LASiS at: **(a)** pH=7; **(b)** pH=13; **(c)** pH=14; (532 nm laser at a fluence of ~1 J/cm^2); **(d), (e)** the corresponding HRTEM images for the case of: **(d)** pH=13 and **(e)** pH=14; (Insets: SAED patterns); **(f)** UV-Vis absorption spectra for colloidal NPs synthesized at different pH values.

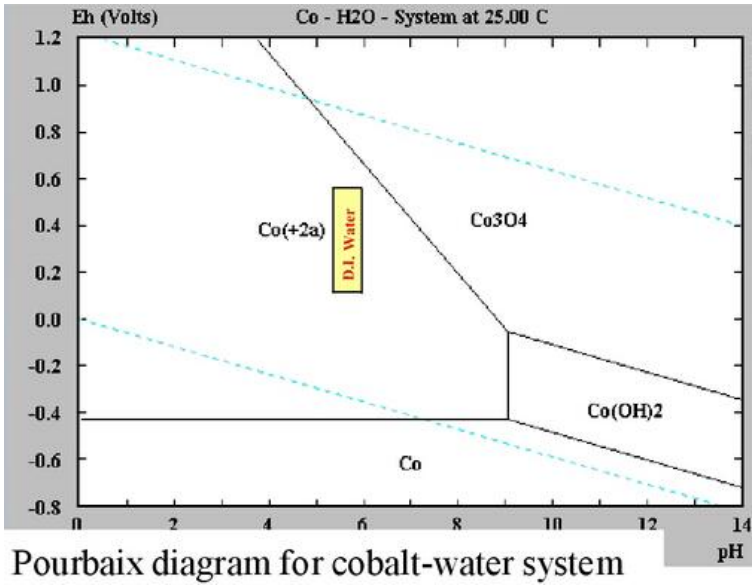


Fig. 3.10 Pourbaix diagram for Cobalt-water system.
(http://www.metallographic.com/Data%20Storage/Corrosion.htm)

Our proposed chemical pathway for Co_3O_4 formation is depicted as following: first of all, both β-$Co(OH)_2$ and Co_3O_4 are more stable and prone to be formed in alkaline condition due to the reduced redox potential (see the Pourbaix-diagram of Co in Fig. 3.10). Secondly, the low solubility of $Co(OH)_2$ in alkaline condition promotes the thermal decomposition of the insoluble $Co(OH)_2$ into Co_3O_4 under LASiS conditions. The presence of β-$Co(OH)_2$ crystals is shown in Fig. 3.9 (b) and (c), as also confirmed by HRTEM images and SAED patterns for the crystal lattices.[60] Finally, the presence of large alkali metal K^+ ions in solution induces electrostatic interactions with closely-packed (111) lattice planes of Co_3O_4, that promotes the growth of β-Co_3O_4 NRs along the selective direction of the (111) plane.[19] Since decrease of redox potentials and presence of K+ ions are both facilitated by the solution-phase alkaline conditions, the growth of Co_3O_4 nanorods is predicted to be induced in the free liquid outside the laser induced cavitation bubble. The optical properties of the NP/NR samples produced under different pH conditions are revealed by the UV-Vis absorption spectra shown in Fig. 3.9 (f). Here, we have confirmed through ICP-OES measurements that all three samples measured contain the same Co concentrations. The results indicate that the overall absorbance for all the NP/NR samples is enhanced as pH increases from 7 to14, which is partially due to the relative stability of Co_3O_4 NPs under alkaline conditions. However, the dramatic improvement in the absorption peak at ~410 nm (~3 eV), specifically for pH=13 sample, can be ascribed to the intensified LSPR that is strongly affected by sizes and shapes of nanostructured materials.[157] It is well-known that critical values for NP sizes dictate the enhancement or dampening of LSPR. Specifically, the LSPR peak for NRs is strongly impacted by the length-to-diameter-ratio (LTDR).[157] In this regard, the specific size and LTDR (~20-40) for the NRs (diameter of ~5 nm and length of ~100-200 nm) formed at pH=13 promotes the LSPR peak at 410 nm, as compared to the absence of the similar peak for the ones formed at pH=14 with an average diameter of 15 nm, as seen in Fig. 3.9 (e). Instead, the absorbance for the NRs at pH=14 case exhibits an overall higher absorbance at longer wavelengths of ~500–700

nm, which can be possibly attributed to its much smaller LTDR (~7-13). Also, we have dispersed the NRs in ethanol solution and ran the UV-Vis test. As is shown in Fig. 3.9 (f), the NRs in ethanol exhibits a absorption peak located at 390 nm, which is different than the NRs in water (410 nm), indicating the absorption peak is from plasmonic other than inter-band transition.

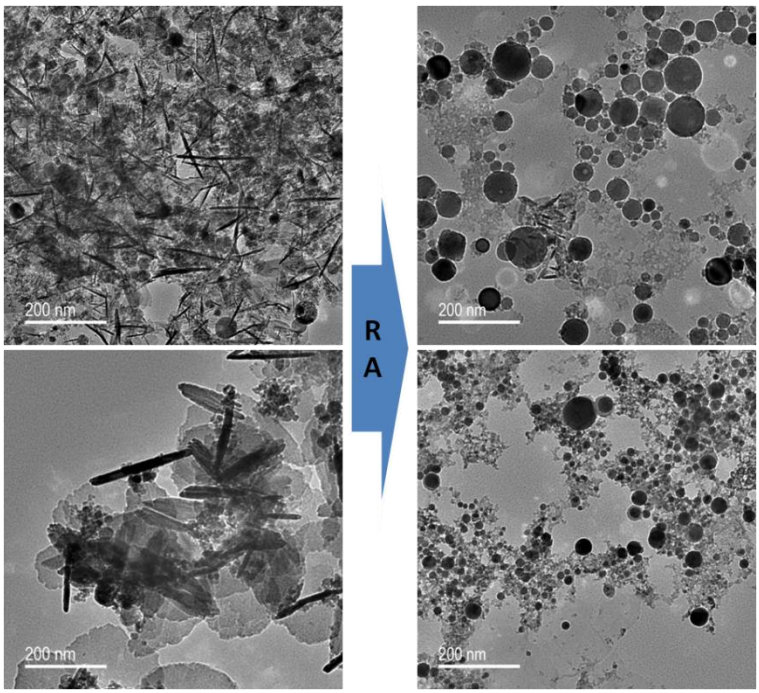


Fig. 3.11 Re-irradiation (RI) by 532 nm laser of Co_3O_4 NRs synthesized through LASiS at pH=13 **(top)** and pH=14 **(down)** for 30 min.

It needs to be pointed out here that the Co_3O_4 NRs are observed to form only at low laser fluence (<5 mJ/cm^2) cases in alkaline conditions. High fluence LASiS or RI completely reshapes them into spherical NPs (see Fig. 3.11). These observations further support the formation of the NRs as a result of ripening processes in the free liquid at an optimal temperature after the collapse of the cavitation bubble, since the solution-phase high temperatures induced by the otherwise high laser fluence conditions make them thermally unstable. Besides, we have also investigated LASiS on Co at other pH values, i.e., pH=2, 3, 10, and 12.[60] However, our TEM results for LASiS products under low pH conditions (pH=2, 3) indicate similar morphologies for

the NPs as obtained under pH=7 conditions, with the exception that the productivity is dramatically reduced due to the instability of metal oxides/hydroxides in acidic conditions. The pH=10 sample also shows similar NP morphology. On the other hand, sparse distribution of nanorods (NRs) are seen in the products under pH=12 conditions, thereby indicating that pH=12 is the threshold for NR formation. Our on-going investigations are focused on understanding and tuning the chemical physics behind the formation of the NRs, in order to tailor their structure-property relations for their applications as water splitting catalysts or as doping materials for enhanced light absorption in photocatalysts.

3.3 Summary

In this chapter, we have presented a facile route for tailored synthesis of nanostructured oxides/hydroxides of Co using an in-house designed laser ablation synthesis in solution (LASiS) set-up that can be tuned for various experimental parameters. Specifically, we investigate the effects of laser parameters (wavelength, laser fluence) and solution phase properties (O_2 content, pH) on the size, shape, structure and composition of the resultant nanostructured materials produced from LASiS on bulk Co targets in aqueous solutions. Our results indicate that the chemical pathway during LASiS on Co in water leads to the formation of metastable intermediates such as CoO and single crystal β-$Co(OH)_2$ NPs in the presence and absence of solution-phase O_2 respectively. Both intermediates transform into Co_3O_4 NPs as the final products through oxidation and/or thermal decomposition in solution phase. In addition, we establish the role of the physics behind the different ablation mechanisms in tailoring the size and morphology of the final Co_3O_4 NPs. For both 1064 and 532 nm lasers, vaporization and normal boiling mechanism during LASiS at low laser fluence (<20 mJ/cm^2) dictates the formation of sparsely agglomerated NPs of bimodal size distribution. In contrast, the more efficient and explosive boiling presides as the dominant mechanism over the former two during LASiS at higher laser fluences that results in mono-modal size distributions of spherical shaped

primary NPs in the agglomerates formed. Furthermore, we demonstrate that the high absorbance of 532 nm laser by solution-phase colloidal NPs promotes their re-ablation into spherical structures with increased average sizes. This is evident from the higher mean particle sizes (~13–22 nm) for NPs produced by 532 nm LASiS as compared to the ones synthesized with 1064 nm LASiS (~10–14 nm). To this end, we conclude that although the 532 nm laser indicates higher energy penetration through the aqueous solutions, its self-absorption by colloidal NPs renders it less productive than ablation with 1064 nm laser over extended period of time. Finally, LASiS on Co in alkaline aqueous solutions (pH≥13) and low laser fluence conditions (<5 mJ/cm^2) produce Co_3O_4 nanorods (NRs) that exhibit enhanced LSPR properties in the visible range of ~400-410 nm wavelength. The aforementioned understanding of the chemical physics of laser ablation for different laser and solution phase parameters is fundamental to our critical design of LASiS for tailored synthesis of a wide variety metal/metal oxide nanostructured materials in future. In turn, the ability to synthesize such tailored complex nanostructures with unique optical properties via a facile, "green" synthesis route, as presented here, is promising for tuning their structure-property relations for applications such as photocatalysis and doping materials in nanocomposites with enhanced light absorption properties.

Chapter 4 Synthesis of $PtCo/CoO_x$ nanocomposites (NCs) via LASiS-GRR as ORR/OER bifunctional electrocatalysts in alkaline conditions

4.1 Introduction

As mentioned earlier in overview, the regenerative alkaline PEMFCs involve two sluggish reactions, namely, ORR and OER for the respective discharging and charging processes. In such a regenerative battery system, it is of critical importance to design efficient, stable and environmental friendly bi-functional catalysts for both the ORR/OER processes in a cheap and reproducible manner. In recently years, the complex of noble metal-transition metal oxides (NM-TMO) system has drawn people's attention due to the synergic "spillover" effects. Such nanocomposites dramatically influence the adsorption/desorption behavior of intermediate species at the catalyst surfaces, meanwhile promote the electron transport from TMO to NM, thereby facilitating the rate determining steps in each of the respective reactions.[102–104]

However, clean synthesis of these complex nanocatalysts in a facile and economically available method still remains elusive. Most synthesis techniques for metal and metal oxide NPs involve wet chemical routes that require intricate experimental steps involving indispensable chemicals such as surfactants, organic ligands, reducing agents, etc. that block their active surface catalytic sites.[78,79,90,158] Many metal/metal oxide NCs are made from perkovsite based oxides that are complicated to synthesize and require multi-step processes with harsh chemical conditions and residues.[98,99,104] Finally, removal of organic encapsulation (ligands and/or surfactants) from metal/metal oxide NPs itself is a challenging and critical step in their preparation.[159] To this end, we proposed using LASiS in tandem with galvanic replacement reactions (GRR) as an alternative cheap, one-step, one-pot route to synthesize those complex NCs as bifunctional ORR/OER electrocatalysts.[160] Here, the

inherent charge screening effect within from LASiS promotes the production of uniformly dispersed colloidal NPs[53] without the need for any surfactants/stabilizing agents that are usually indispensable in chemical synthesis routes and yet, potentially harmful for surface catalytic activities. On the other hand, incorporating chemical reduction kinetics such as GRR provides superior control on NP composition and morphology (especially, for binary or ternary intermetallic NPs) that overcomes the inherent drawbacks of LASiS mentioned earlier.[35] In such a combination, unique non-equilibrium thermodynamics and kinetics at the plasma-liquid interface is anticipated to potentially generate novel nanostructures or, nanocomposites with tailored morphologies, compositions and metastable structures.

For conventional GRR process, important parameters that affect the structure/morphology of the final products include initial salt concentration, reaction temperature and time, and solution phase pH.[65,161] It has been reported by some research groups that excess metal salt might induce the de-alloying of initially formed metal alloys and lead to the formation of pure metal NPs (reduced second metal);[64,162] while Noel K. et al indicated that the solution phase pH largely impact the core-shell structure of the resultant PtCo NPs.[75] For the current research project, we will first investigate the aforementioned laser and environmental parameters for LASiS on different pure metals, then combine with the GRR process for a systematic study. In such a case parameters including initial metal salt concentration, ablation time, laser fluence and solution phase pH, aging and washing conditions will be tuned to imply their impact on the detailed composition, structure, alloying degree as well as their potential applications as ORR and OER bifunctional catalysts.

4.2 Results and discussion

4.2.1 Mechanistic picture of LASiS-GRR

In the current tandem LASiS-GRR technique, the galvanic replacement reaction (GRR) between K_2PtCl_4 and Co occurs in the above-mentioned system based on the

respective redox potentials for Co/Co^{2+} (-0.28 V vs. SHE) and $PtCl_4^{2-}/Pt$ (0.76 V vs. SHE) as:

$$PtCl_4^{2-} + Co \rightarrow Pt + Co^{2+}$$

However, it is obvious that further oxidation of Co^{2+} to Co^{3+} cannot be initiated by the simultaneous reduction of solution phase Pt^{2+} ions since the mid-point potential for Co^{2+}/Co^{3+} is much higher (1.82 V vs. SHE). Theoretically, the displacement reaction can occur between $PtCl_4^{2-}$ and any metal with redox potential $<$ 0.76 V vs. SHE (for $PtCl_4^{2-}/Pt$).

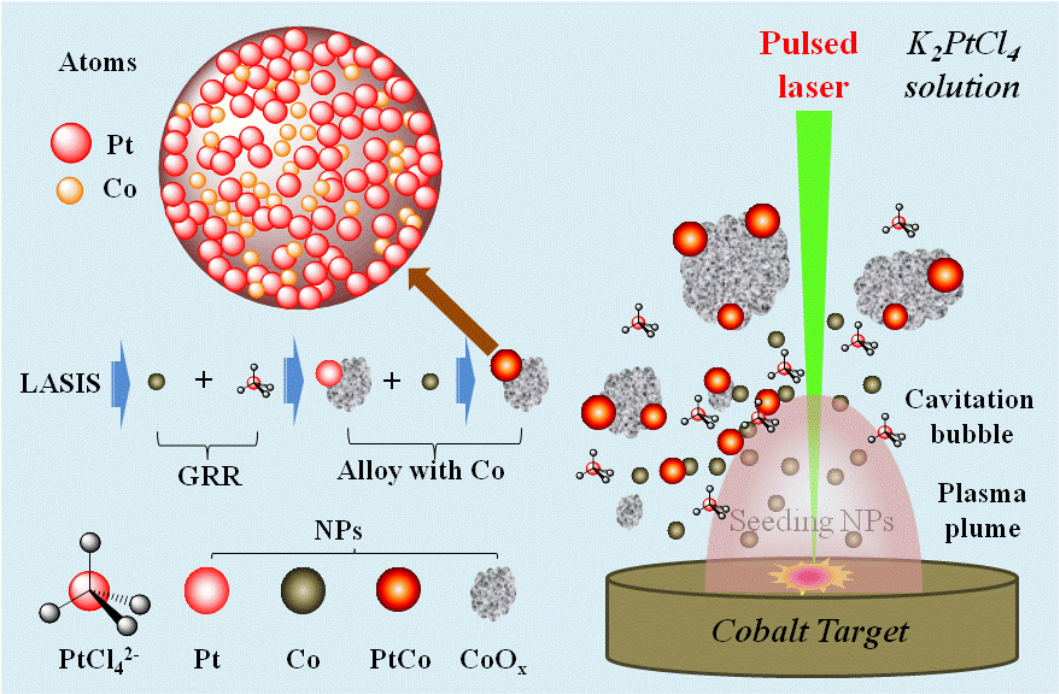


Fig. 4.1 Schematic representation of the tandem LASiS-GRR technique that synthesize $PtCo/CoO_x$ nanocomposites (NCs).

Fig. 4.1 shows the schematic for the reaction pathways during LASiS-GRR that lead to the NC formation. Pulsed laser beam creates a liquid confined plasma plume with extremely high temperature and pressure on the Co surface that results in thermal vaporization of the metal target. Large amount of seeding NPs then start to form inside an oscillating cavitation bubble resulting from the expanding plasma plume. Thereafter, the seeding NPs undergo collisional quenching and redox reactions with

the solution phase ionic species at the bubble-liquid interface upon the bubbles collapse. However, only part of those seeding Co NPs can go through GRR with K_2PtCl_4 due to the high local concentration but limited reaction rate, thereby leaving the rest of them either coalesce (alloy) with reduced Pt or get oxidized by the solution phase O_2/H^+. The newly formed intermetallic PtCo NPs then continue to coalesce with each other into large spherical NPs that are partially embedded into the CoO_x matrices.

4.2.2 Structure and composition analysis for the PtCo/CoO_x NCs

In our recent work explaining the mechanism of LASiS, it was shown that LASiS on bulk cobalt produces meta-stable CoO, which further oxidizes rapidly into stable Co_3O_4 in the aqueous solution.[60] In the current work, we carried out LASiS on cobalt with four different initial K_2PtCl_4 concentrations (*i.e.*, 25 mg/l, 60 mg/l, 120 mg/l and 250 mg/l) to produce four different NP colloidal samples labeled here onwards as PtCo-1, PtCo-2, PtCo-3 and PtCo-4 respectively. The corresponding Pt and Co NP concentrations in each of the samples, as revealed from ICP-OES measurements, were summarized in Table 4.1. The results indicate that ~60-70% of the precursor Pt salt is transformed into Pt NPs upon ablation at 60 J/cm^2 fluence for 30 min. The Pt:Co molar ratios was calculated to be 1:9, 1:4, 1:2 and 1:1 for PtCo-1 to PtCo-4 respectively. The unreacted residual K_2PtCl_4 as well as any excess KCl formed are washed away during the centrifugation step. This is also confirmed by the TEM images, as shown in Fig. 4.2 (a-d), indicating that mainly two types of nanostructures are found in all four samples, namely individual spherical NPs (darker contrast) embedded in a large amount of highly porous "sponge-shaped" nanostructures (lighter contrast). These structures are expected to be CoO_x (lighter) and Pt and/or PtCo intermetallic (darker) NPs respectively, where the different contrasts in the transmitted electron intensities are due to their different mass to charge ratios. The size distributions for the darker spherical Pt-based NPs (which are later revealed to be Pt-Co nanoalloys) are shown in Fig. 4.2.e-h, where the mean sizes

increase from 8.5 nm to 17.7 nm with the increase of the Pt:Co ratios. This is ascribed to the enhanced coalescence due to increased concentrations of Pt NPs. The existence of Pt and CoO_x NCs are further confirmed by the identification of their respective crystalline structures in the SAED patterns (shown in the insets of Fig. 4.2.a-d) along with calculated d-spacing values (provided in Table 4.2). However, in our earlier work[60] with LASiS on bulk Co (without any K_2PtCl_4), we had shown that initially formed metastable CoO upon three days of ageing underwent complete oxidization into Co_3O_4 by the solution phase O_2 and H^+. In contrast, the present study indicates that LASiS on Co in the presence of K_2PtCl_4 salt solution, when exposed to the identical ageing process, results in both Co_3O_4 and CoO nanostructures coexisting in the final products. This is possibly due to the highly non-equilibrium processes where the seeding Co NPs emerging from the cavitation bubble undergo ultra-fast quenching and reactions with the solution phase metal salt ions at the liquid front. Thus, during ablation in the aqueous solution with K_2PtCl_4 salts, a large portion of Co is converted to CoO through galvanic replacement reaction (GRR) rather than direct oxidation, since the redox potential for $Pt^{2+} \rightarrow Pt^0$ (0.76 V vs. SHE) is even higher than $O_2 \rightarrow O^{2-}$ (0.4 V vs. SHE). The relatively higher stability of these CoO NPs could possibly be due to this inherently different formation mechanism**.** As a result, it is difficult for the CoO NPs to further get oxidized into Co_3O_4 or the oxidation rate is much slower.

Table 4.1 Pt and Co concentrations from ICP-OES measurements for various $PtCo/CoO_x$ NCs synthesized by LASiS-GRR at different initial K_2PtCl_4 salt concentrations.

	Initial K_2PtCl_4 Conc. (mg/l)	**Pt Conc. (mg/l)**	**Co Conc. (mg/l)**	**Molar Pt/Co ratio**
PtCo-1	25	7.3	20	1:9
PtCo-2	60	19	23	1:4
PtCo-3	120	42	25	1:2
PtCo-4	250	81	25	1:1

Table 4.2 Experimental d-spacing values calculated from the SAED results in Fig. 4.2.

Experimental d-spacing (Å)							
PtCo-1		**PtCo-2**		**PtCo-3**		**PtCo-4**	
2.86	*Co_3O_4 (220)*	**2.47**	*CoO (111)*	**2.26**	*Pt (111)*	**2.27**	*Pt (111)*
2.43	*Co_3O_4(311)*	**2.27**	*Pt (111)*	**1.95**	*Pt (200)*	**1.96**	*Pt (200)*
2.1	*CoO (200)*	**1.95**	*Pt (200)*	**1.39**	*Pt (220)*	**1.39**	*Pt (220)*
1.95	*Pt (200)*	**1.5**	*CoO (220)*				
1.55	*Co_3O_4 (333)*	**1.39**	*Pt (220)*				
1.29	*CoO (311)*						

In addition, high resolution TEM images (HRTEM) indicate the three different areas marked as b, c, d in Fig. 4.3.a that correspond to Pt (111) (d=2.26 Å), Co_3O_4 (220) (d=2.86 Å) and CoO (200) (d=2.13 Å) exposed to the surface, as shown in Fig. 4.3.b, c, d respectively. Lastly, control experiments were also carried out for laser irradiation on the K_2PtCl_4 solution only (without any Co target), in which case no Pt NPs are formed[160], confirming that the formation of Pt NPs is largely due to the galvanic replacement reactions (GRR).

In order to further investigate the elemental composition and distribution in the products, EDX tests were carried out for the STEM mode images. The results from the high-angle annular dark-field (HAADF) image, as shown in Fig. 4.4.a specifically for the PtCo-3 sample, reveal the corresponding elemental mappings for Pt, Co and O, (Fig. 4.4.b, c, d respectively). These images show that Pt is mainly distributed in the bright spherical NPs in the HAADF image (*i.e.*, the four large NPs at the center). In contrast, Co is mostly distributed in the background gray areas although its presence is strongly noted inside the brighter NPs (see Fig. 4.4.c), while O is found to be uniformly distributed in the whole image. Furthermore, detailed EDX spectra in Fig. 4.4.e and f which correspond to the areas marked e and f respectively in Fig. 4.4.a indicate strong Pt and Co peaks along with weak O peak inside the bright spherical particle (Fig. 4.4.e).

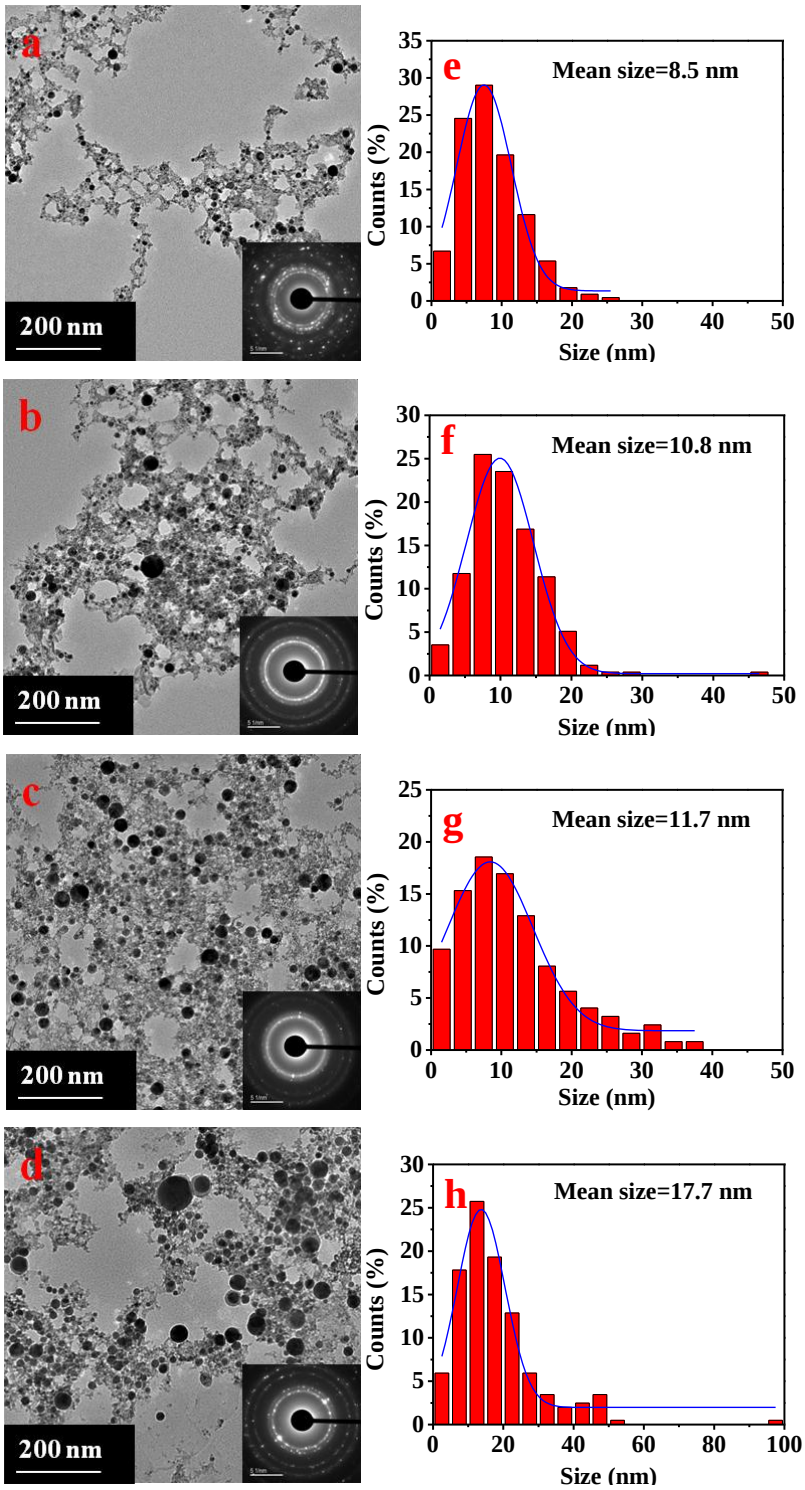


Fig. 4.2 **a-d.** TEM images along with the corresponding SAED patterns (inset) for the PtCo/CoO_x NCs synthesized by LASiS-GRR with different Pt:Co atomic ratios of: **a.** 1:9 (PtCo-1); **b.** 1:4 (PtCo-2); **c.** 1:2 (PtCo-3); **d.** 1:1 (PtCo-4). The scale bar in for SAED patterns is 5 (1/nm); **e-h.** Corresponding size distributions for dark colored PtCo alloyed NPs in **a-d**.

In comparison, Fig. 4.4.f indicates negligible Pt peak along with a relatively strong O peak in the background areas. It is noted here that the Cu and C signals in the spectra are from the TEM carbon film with copper grids. The absence of any other detectable elements in the EDX data indicates that all the residual chemicals such as K_2PtCl_4 and KCl have been washed away by the centrifuging process. The aforementioned results for the elemental mappings of Pt, Co and O in Fig. 4.4.b, c and d, along with the EDX spectral intensities in Fig. 4.4.e and f, clearly suggest the formation of PtCo nanoalloy inside the bright spherical NPs (marked as the areas e in Fig. 4.4.a). This also validates our earlier assumption that the as-synthesized nanocomposites are made of PtCo nanaolloy (the brighter NPs) embedded in the CoO/Co_3O_4 matrices.

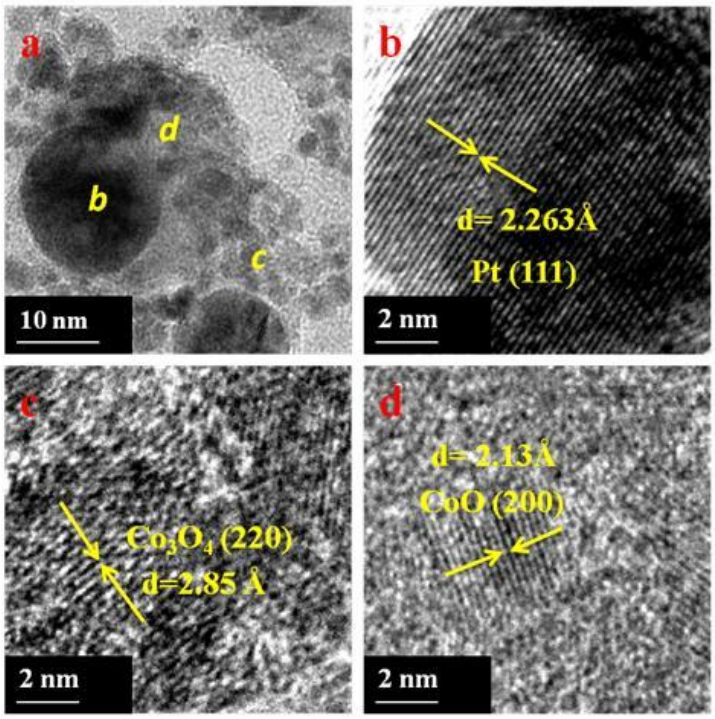


Fig. 4.3 **a.** Representative HRTEM image of PtCo-2 sample with the corresponding positions marked b, c, d indicating the lattice fringes in the enlarged images for: **b.** Pt, **c.** Co_3O_4, and **d.** CoO respectively.

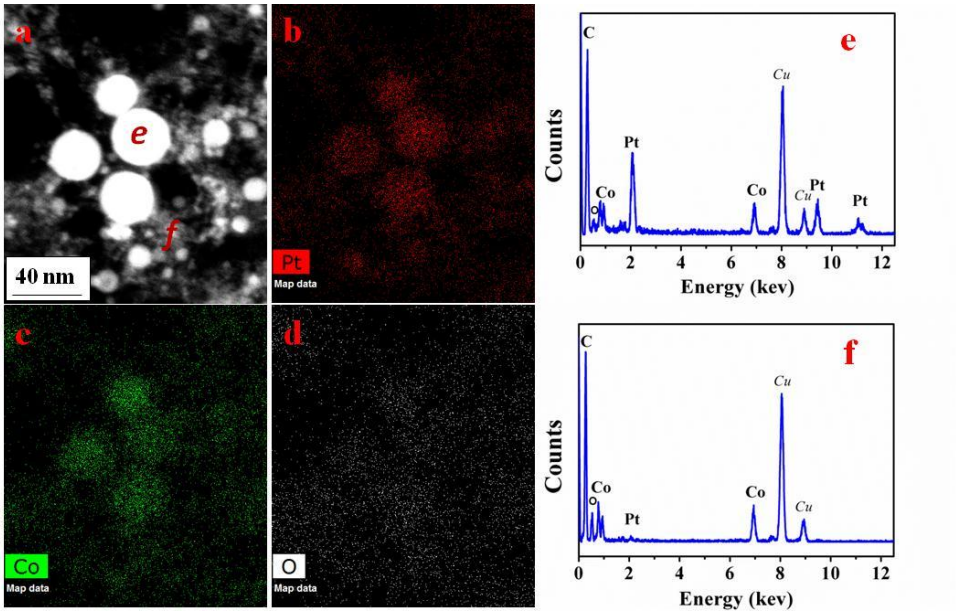


Fig. 4.4 EDX results for PtCo-3 sample along with: **a.** HAADF image, and elemental mappings for **b** Pt, **c.** Co and **d.** O respectively; **e, f.** Corresponding EDX spectra at the positions marked in **a.** (Cu and C signals are from the TEM carbon film with copper grids).

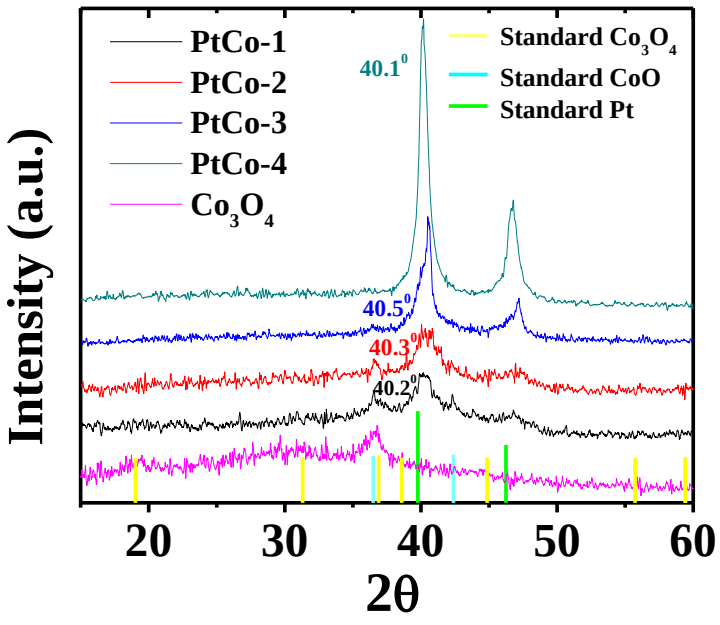


Fig. 4.5 Comparison of XRD patterns for PtCo/CoO_x nanocomposites with different Pt:Co ratios along with standard peak positions for Co_3O_4, CoO and Pt indicated by yellow, purple and green vertical lines respectively. The values marked in the figure indicate the PtCo (111) peak positions.

Table 4.3 Calculated alloyed Pt:Co ratio from XRD results in Fig. 4.5.

Sample	2θ (°)	Lattice constant (Å)	Pt: Co
PtCo-1	40.2	3.88	8.6: 1
PtCo-2	40.3	3.87	6.7: 1
PtCo-3	40.5	3.85	4.6: 1
PtCo-4	40.1	3.89	11.5: 1

To corroborate the abovementioned results, Fig. 4.5 summarizes the XRD data for all the PtCo/CoO_x NCs dispersed in carbon black, where the sample from LASiS on Co (without the K_2PtCl_4 salt) displays the distinct Co_3O_4 (311) peak (PDF-#42-1467) at 2θ=36.9° but does not show any characteristic peak for CoO (PDF-#43-1004). In contrast, the PtCo-1 sample indicates a CoO (200) peak at 2θ=42.4° along with a minor peak at 2θ=~36.6° which is assigned as an overlapped peak of CoO (111) (2θ=36.5°) and Co_3O_4 (311) (2θ=36.9°). These results further confirm our previous SAED data in Fig. 4.2.d that the CoO gets partially conserved in the PtCo/CoO_x NCs that do not undergo further oxidation during the ageing process. Meanwhile, two distinct characteristic peaks are also observed for this sample at 2θ=40.2° and 2θ=46.7° that are assigned to the (111) and (200) peaks for PtCo alloy. Here, one needs to note that the 2θ values for standard Pt are 39.8° (111) and 46.2° (200) (PDF-#04-0802). The shift of these peaks to higher angles is attributed to the Pt alloying with Co that result in a shrunken lattice constant calculated to be ~3.88 Å as compared to 3.92 Å for standard Pt. Besides, Fig. 4.5 also reveals that the alloyed PtCo peaks quickly become dominant with the increase of Pt:Co ratio. Specifically, for the case of PtCo-3 and PtCo-4 (Pt-Co ratio equals to 1:2 and 1:1), the CoO_x peaks are barely discernable, which is ascribed to the much higher crystallinity and hence, the diffraction pattern intensity for Pt alloyed with Co as compared to that for CoO_x. It needs to be noted here that this phenomenon is also supported by the previous SAED patterns in the insets of Fig. 4.2.a-d. The alloyed Pt:Co ratios from PtCo-1 to PtCo-4 are estimated to be 8.6:1, 6.7:1 and 4.6:1 and 11.5:1 respectively according to the Vegard's law,[75] as summarized in Table 4.3. As also described earlier in Fig. 4.1, the seeding Co NPs from the cavitation bubble go through two competing reactions,

namely, either GRR with Pt^{2+} or oxidation by solution phase O_2 and H^+. When the initial K_2PtCl_4 concentration is low, a large portion of Co will react with solution phase O_2/H^+, thereby leaving few available seeding Co NPs to alloy with Pt formed via GRR mediated reduction by Co. Hence, the Co:Pt ratio in the PtCo alloys rises at first with increasing initial K_2PtCl_4 concentrations in the solution. However, beyond a critical value, further increase of Pt^{2+} ion concentrations leads to oxidation of Co atoms in the initially formed PtCo alloy. Such a de-alloying process will reduce the amount of alloyed Co in the PtCo nanoalloys, and has already been reported by some other works.[162]

4.2.3 Investigation of ORR/OER catalytic activities

The catalytic activities for both pure Co_3O_4 NPs and PtCo/Co_3O_4 NCs were tested with the aid of the rotating disk electrode (RDE) measurement in O_2-saturated 1M KOH solution, as shown in Fig. 4.6. In order to overcome the electronic conductivity limitations and increase the catalytic surface area for ORR experiments, all the synthesized NCs were dispersed in CB (Vulcan XC-72R, weight ratio NP:CB=1:4). It needs to be mentioned that linear sweep voltammograms (LSV) on pure Co_3O_4 NPs generated from high fluence (HF, 60 J/cm^2) and low fluence (LF, 1 J/cm^2) LASiS in chapter 3[60] indicated that half-wave potentials and diffusion limiting currents for HF Co_3O_4 samples are better than those for LF Co_3O_4 samples (*i.e.*, 770 mV and 3.25 mA/cm^2 vs. 740 mV and 2.75 mA/cm^2 for HF vs. LF samples respectively). This is attributed to the uniform sizes and spherical shapes of HF Co_3O_4 NPs obtained from the explosive boiling mechanism of LASiS at high laser energy. Hence, the choice for all catalytic studies presented in the present article are for the Co_3O_4 and PtCo/CoO_x samples synthesized at HF (60 J/cm^2) conditions. We also noted that the measured ORR catalytic activities for our Co_3O_4 NPs itself compared extremely well with those observed by other peer works.[76,82,92,93] We believe that the clean, one-step synthesis process for LASiS plays a role here in generating these NPs devoid of any additional chemicals (surfactants, reducing agents, etc.) that can retard

or poison their catalytic activities. Fig. 4.6.a compares the ORR catalytic performance for each of the catalyst samples under study through the LSV test. The results indicate a remarkable improvement for the ORR activities with the increase of Pt to Co ratio from 1:9 (PtCo-1) to 1:2 (PtCo-3). Specifically, the half-wave potential for the PtCo-3 sample is improved to 860 mV, which is almost comparable to the corresponding values for standard Pt/C samples (870 mV). The ORR overpotential for this sample is calculated to be 370 mV based on the standard potential for reduction of oxygen to water being 1.23 V. However, as the Pt:Co ratio further increases to 1:1 for PtCo-4, the half-wave potential slightly reduces to 850 mV, with the overpotential calculated to be 380 mV. Besides, Fig. 4.6.b compares the Tafel plots for the abovementioned samples generated from Fig. 4.6.a over the low overpotential regions. The measured Tafel slope values are 53.0, 42.2, 40.3, 39.2 and 54.6 mV/dec respectively as compared to ~66.2 mV/dec for standard Pt/C samples, thereby indicating higher charge transfer coefficients for the as-synthesized catalysts. Fig. 4.6.c further compares the mass activities per unit Pt loading amount at 0.85 V vs. RHE for the $PtCo/CoO_x$ NCs studied. The results indicate a much higher mass activity for PtCo-3 sample (0.73 mA μg^{-1} Pt) than the commercial Pt/C (0.54 mA μg^{-1} Pt). The other three samples (PtCo-1, PtCo-2 and PtCo-4) demonstrate lower but comparable mass activities, although the PtCo-4 sample with an increased amount of Pt indicates a marked drop in the ORR activity. The excellent ORR activities for these materials are mainly attributed to the following reasons. Firstly, the formation of alloyed PtCo nanostructures shrinks the Pt lattice constants and decreases the effective sites for OH^- adsorption. Added to that, it enhances the Pt-O bonding due to higher 5d orbital vacancies in its electronic structure that promotes the donation of π electrons from O_2 to Pt.[79,88] Hence, the sites on the PtCo alloy NPs (known for their ORR activities) preferentially promote both O_2 adsorption and OH^- desorption, both benefit the ORR efficiency. Secondly, the NC of the metal-transition metal oxide (NM-TMO) system further benefits the ORR process by providing a synergic "spill-over" effect.[102,159]

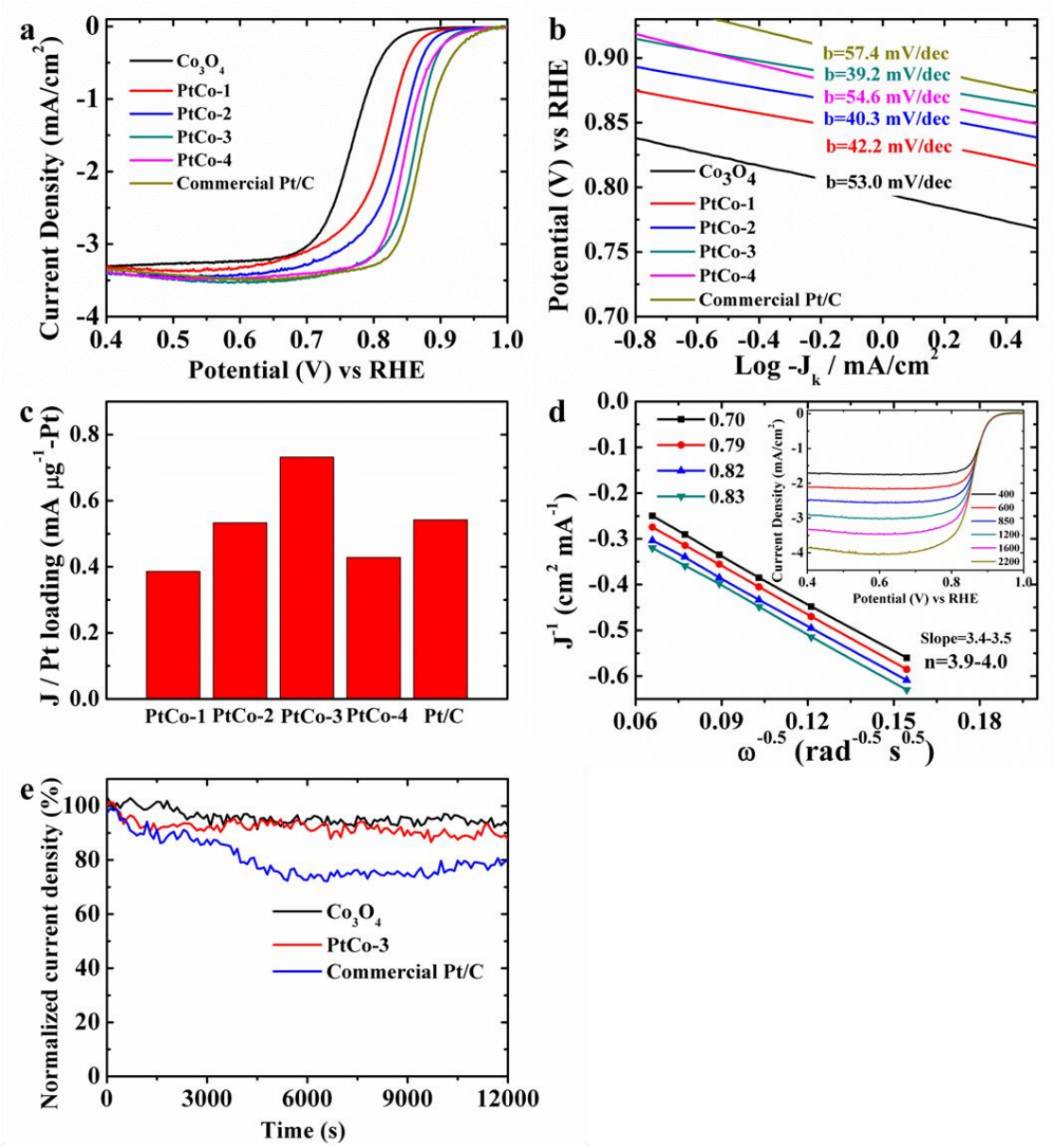


Fig. 4.6 Electrochemistry data for as-synthesized Co_3O_4 NPs and PtCo/CoO_x NCs compared to standard Pt/C samples using: **a.** Linear sweep voltammograms for ORR analysis in 1 M KOH electrolyte saturated with dissolved O_2 at 1600 rpm and scan rate of 5 mV/s; **b.** Tafel plots from **a**; **c.** Comparison of mass activities per unit Pt mass loading at 0.85 V vs. RHE; **d.** Koutecky-Levich plots from rotating disk voltammogram (RDV) data (shown in inset) for PtCo-3 at different potentials; **e.** Stability comparison for Co_3O_4, PtCo-3 and standard Pt/C through chronoamperometry (CA) tests.

Specifically, the OH^- reduced from O_2 is readily desorbed from the active PtCo sites and transferred to the sponge-shaped CoO_x sites which are less active according to their respective M-O bonding strength and intermolecular affinities. Thus, the best ORR activity is promoted by the PtCo-3 catalyst with optimal Pt content (33.3 molar %, 62.3 wt. %) that leads to higher degree of Pt-Co alloy formation (confirmed by Fig. 4.5 and Table 2) with more lattice shrinkage and appropriate sizes (mean size=11.7 nm), as well as by the balanced PtCo to CoO_x ratio that potentially maximizes the synergic "spill-over" effects.

The dynamics of the electron transfer process during ORR activities of the aforementioned catalysts are analyzed using the Koutecky-Levich (KL) equation for rotating disk voltammetry (RDV) measurements carried out at different speeds. Fig. 4.6.d shows the slopes for the KL plots generated from rotation-rate dependent current-potential curves (inset in Fig. 4.6.d) for the PtCo-3 NCs in the range of 0.70 – 0.83 V. The slopes estimate the number of electrons transferred (n) to be 3.9-4.0, thereby indicating an ideal four-electron transport process for the ORR activity. (Detailed RDV data and KL plots for PtCo-1, PtCo-2 and PtCo-4 NCs can be found in our recent published paper where the corresponding electron transfer numbers are 3.8-4.0 for all of them.[160]

In addition to the good ORR catalytic activities, chronoamperometric (CA) measurements also reveal excellent stabilities for the PtCo-3 NC samples. Fig. 4.6.e compares the normalized current density (%) at the corresponding half-wave potentials for the Co_3O_4, PtCo-3, and standard Pt/C samples. As can be seen from the results, the ORR current densities decay by less than 15% over 12000s of continuous operation for both the Co_3O_4 and PtCo-3 samples. In contrast, the standard Pt/C sample indicates a ca. 28% current density reduction over the same period of time. The decay in the catalytic activities of standard Pt/C samples is attributed to its surface oxidation as well as particle dissolution and aggregation in the alkaline electrolyte[85], which hardly occur for the metal oxides (Co_3O_4/CoO). In fact, in the case of the PtCo/CoO_x NCs, the existence of the sponge-shaped CoO_x serve as a

matrix material that protects the PtCo alloyed NPs from aggregation or dissolution. Meanwhile, the alloyed PtCo structure also helps to slow down the oxidation of Pt due to the much higher electron negativity of Co.

Finally, the OER catalytic activities for the PtCo NC samples are investigated by comparing with the results for pure Co_3O_4 and standard Pt/C samples, as shown in Fig. 4.7. For comparing the OER overpotentials, all potential measurements were carried out with 10 mA/cm^2 as the metrics due to its relevance to solar fuel characterizations[74].

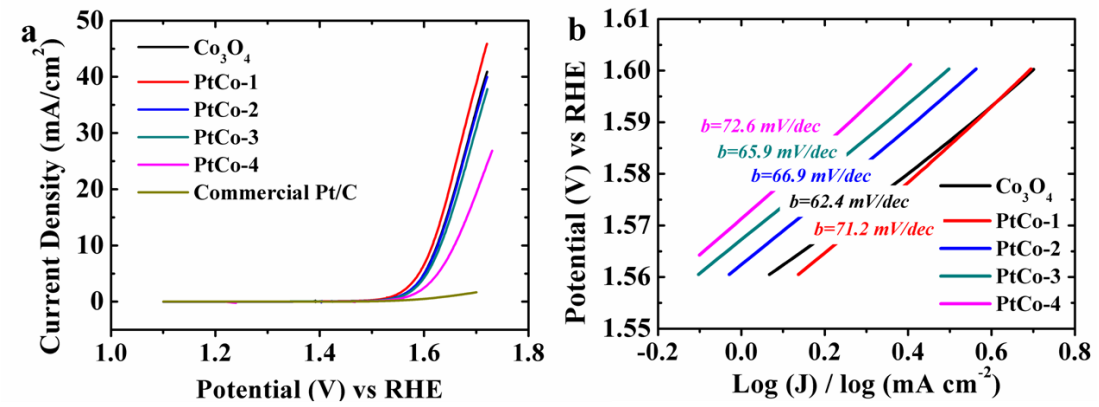


Fig. 4.7 **a.** Linear sweep voltammograms for OER analysis on $PtCo/CoO_x$ NCs compared to those for Co_3O_4 NPs and standard Pt/C samples; **b.** Corresponding Tafel plots in the potential range of 1.55 - 1.60 V.

The results reveal that, with an overpotential of 385 mV (Fig. 4.7.a) and a measured Tafel slope of 62.4 mV/dec, the LASiS generated Co_3O_4 itself is comparable or, even better than other reported OER catalysts.[74,76,80,98,99,104] As expected, the standard Pt/C sample shows the worst OER activities (with an overpotential of ~640 mV). As also mentioned earlier, the high OER activity for our Co_3O_4 NPs is attributed to the clean synthesis route of LASiS that produces the sponge-like nanostructures with enhanced surface area that do not have any surface contamination from unwanted chemicals during the preparation. But, the most significant observation from Fig. 4.7.a is that the PtCo-1 sample exhibits an even smaller OER overpotential (380 mV) than the Co_3O_4 sample that is typically well-known for OER activities. In fact, the overpotentials for PtCo-2 and PtCo-3 are

also comparable (~385 and 386 mV respectively), indicating that these PtCo/CoO_x NCs exhibit good OER catalytic activities as well. Here we also note that the PtCo-4 sample displays a relatively poorer activity (overpotential of ~ 435 mV) that could be possibly due to the scarcity of CoO_x in the NC catalyst. It is also noted here though that Tafel slopes for the PtCo NCs are slightly larger (~71-72 mV/dec for PtCo-1 and PtCo-4 whereas, ~66-67 mV/dec for PtCo-2 and 3) as compared to those for pure Co_3O_4 (~ 62.4 mV/dec) as seen from Fig. 4.7.b. The enhanced OER performance can also be attributed to the aforementioned synergic "spillover" effect for specific NM-TMO systems, where the produced O_2 is desorbed from active CoO_x surfaces and transferred to relatively inert PtCo nanoalloy sites with higher O_2 affinity. For better understanding, a schematic in Fig. 4.9 illustrates the detailed mechanistic picture behind the synergic "spill-over" effects responsible for the site-specific adsorption/desorption of the desired species to promote the bifuncitonal catalytic performances in the aforementioned NCs. For both ORR and OER, the PtCo sites and CoO_x matrices provide synergic support for each other wherein each of the sites provides refuge for the undesirable species from the other sites, thereby promoting both the reactions.

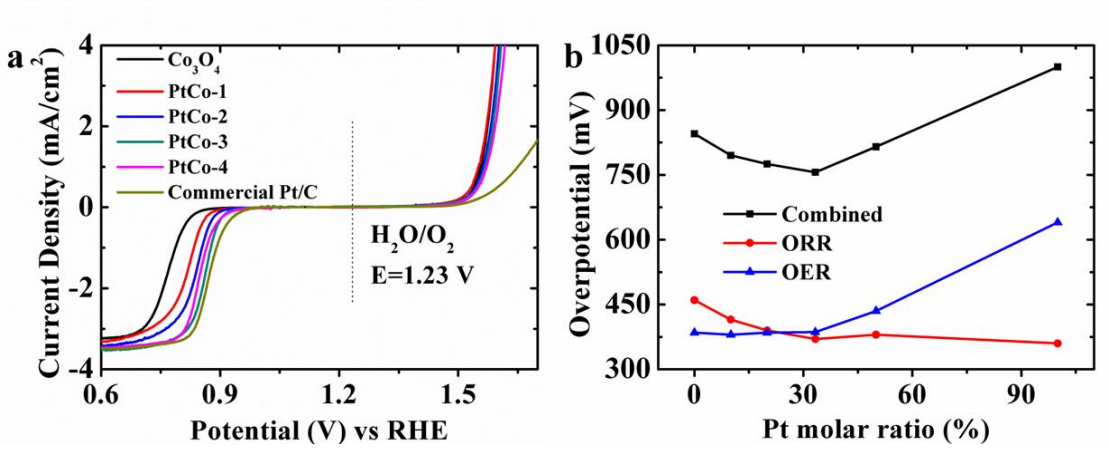


Fig. 4.8 **a.** Comparison of bifunctional catalytic activities for both OER and ORR through Linear sweep voltammogram (LSV); **b.** Evolution of ORR, OER and combined overpotentials for catalytic samples understudy with the increase of Pt molar ratio.

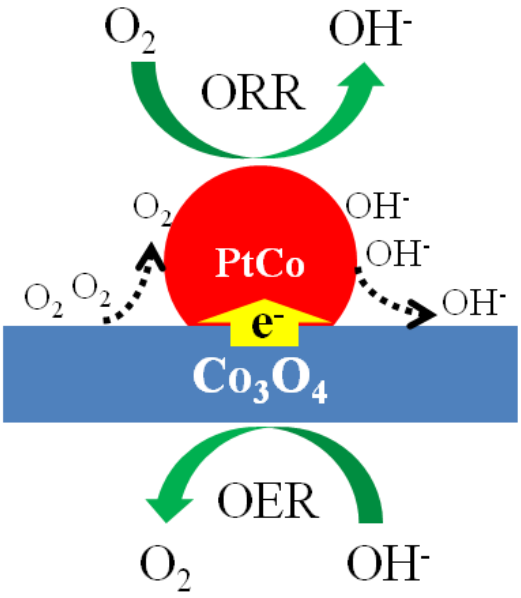


Fig. 4.9 Schematic illustrating the mechanism of the "spill-over effect".

The combined overpotentials for PtCo-1 to PtCo-4 are calculated to be 795, 775, 756, and 815 mV respectively, which remarkably outperform the overpotentials for either Co_3O_4 or the commercial Pt/C (*i.e.*, 845 mV for Co_3O_4 and 1000 mV for commercial Pt/C), as shown in Fig. 4.8.a and b as well as reported in Table 4.4. These results indicate that the synthesized PtCo NCs exhibit superior bifunctional catalytic performances for both ORR and OER processes, especially for the PtCo-3 sample with an optimal Pt amount (33.3 molar %, 62.3 wt. %). Overall, we attribute the excellent bifunctional catalytic properties of the PtCo/CoO_x NCs to the unique heteronanostructuring of alloyed PtCo NPs embedded in the sponge-shaped CoO_x matrices which, while contributing to the enhanced ORR and OER behaviors due to the synergic "spillover" effects, prevent the PtCo NPs from aggregation and dissolution in the alkaline media.

Table 4.4 Comparison of OER and ORR overpotentials for $PtCo/CoO_x$ NCs, Co_3O_4 and the commercial Pt/C samples along with the respective combined overpotentials.

Sample	ORR OP (mV)	OER OP (mV)	Combined OP (mV)
Co_3O_4	460	385	845
PtCo-1	415	380	795
PtCo-2	390	385	775
PtCo-3	370	386	756
PtCo-4	380	435	815
Pt/C	360	640	1000

4.3 Summary

We presented a novel one-pot, one-step, "green" synthesis route that combines laser ablation synthesis in solution in tandem with galvanic replacement reactions (tandem LASiS-GRR) to manufacture complex $PtCo/CoO_x$ nanocomposites (NCs) with outstanding ORR and OER catalytic activities. The transformative concept here is the ability to synthesize such complex heteronanostructures in one step without the need for any harsh chemical reagents and/or, surfactants. This is made possible by the non-equilibrium thermodynamic conditions emerging from extreme physicochemical conditions of high energy LASiS operating in tandem with chemical reduction processes (GRR in this case). The synthesized PtCo NCs exhibited excellent yet, stable catalytic activities for both oxygen reduction reactions (ORR) and oxygen evolution reactions (OER) in alkaline media. Specifically, we reported a combined overpotential of 756 mV vs. RHE for the PtCo-3 NC (33.3 molar %, 62.3 wt. %), which is the highest value ever reported using carbon black as the supporting material. This excellent bifunctional activity is attributed to the structural and electronic properties of PtCo nanoalloy that promote oxygen adsorption, as well as to the sponge-shaped CoO_x matrices in which the PtCo NPs are embedded that bring about the synergic "spillover" effects to facilitate both ORR and OER activities. Added to this, the CoO_x matrix also prevents the PtCo NPs from aggregation and dissolution in alkaline electrolytes. Encouraged by the current results, we have work in progress to

extend the aforementioned clean yet, facile synthesis routes for the future design of various complex intermetallic NCs in a rapid and cost-effective fashion.

Chapter 5 Synthesis of PtCo nanoalloys (NAs) via LASiS-GRR as ORR electrocatalysts in acidic conditions

5.1 Introduction

Pt-transition metal nanoalloys (Pt-M NAs) have been considered as the most efficient ORR electrocatalysts for PEMFCs in acid condition. Among all types of Pt-M NAs, PtCo system has attracted the most attention due to its relatively higher activity and stability for the ORR process[79,107,163–169]. The nominal Pt:Co ratio as well as the degree of alloying in these nanocatalysts play a critical role in tuning the nanoscale crystalline structures and band structures which in turn dictate the aforementioned geometric and electronic effects responsible for tailoring their ORR catalytic activities [79,106,170,171]. Conventional PtCo alloys were usually prepared by simultaneous reduction of cobalt salts (e.g., $Co(NO_3)_2$, $CoCl_2$) and platinum precursors ($Pt(acac)_2$, K_2PtCl_4, H_2PtCl_4) in either organic or aqueous conditions, and almost always involve the use of external and indispensible stabilizing agents (CTAB, PVP, oleylamine etc.) [105,167,171]. Recently, a wide range of synthesis techniques have been developed that include impregnation [79], solvothermal method [172], tandem decomposition and chemical reduction [123], polyol method [173], reverse micelle method [174], replacement reaction [75], etc. Yet, most of those synthesis techniques involve wet chemical routes that require intricate steps and even these techniques inevitably use harsh unwanted chemicals in the form of surfactants and/or, stabilizing agents. These organic residues on the NP surface are detrimental to their interfacial catalytic properties and eventually, systematic removal of those organic encapsulations from these alloyed/intermetallic NPs becomes a challenging and critical step in itself for large-scale production of nanocatalysts. Besides, a fine control of the Pt:Co atomic ratios and alloying degrees for systematic synthesis of a wide range of nanocatalysts still remains elusive in most of these techniques, thereby restricting the application of

these ORR catalysts to only limited environmental conditions [107,170,173–175]. As a consequence, clean synthesis of PtM alloyed NPs that allows precise construction of inter-atomic structure and extent of alloying in a facile, cheap, and reproducible manner is imperative.

To this end, in Chapter 4 we reported using LASiS-GRR as a green synthesis technique for the synthesis of PtCo/CoO_x NCs as excellent bifunctional catalysts for both ORR and OER in alkaline media. While in the current chapter we built on a modified LASiS-GRR technique to synthesize pure PtCo alloys (no CoO_x NPs) that exhibit excellent ORR activities in acid electrolyte solutions. In principle, LASiS involves a liquid-confined plasma plume expanding with extremely high temperatures and pressures (c.a. 10^3 K and 10^9 Pa respectively) [35] that thermally vaporizes a metal target and initiates ultrafast propagation of cavitation bubbles. Typically, these cavitation bubbles contain the nucleated seeding NPs that finally undergo rapid collisional quenching at the bubble-liquid interface [34,35,50,51,176,177], while initiating simultaneous chemical reduction reactions with the solutions phase precursors/species. The current work involves the LASiS-GRR process in the presence of $PtCl_4^{2-}$ ions as the solution-phase metal precursors. In such a setup, seeding Co NPs from within the cavitation bubble go through two competing reactions at the liquid front, namely: 1. reactions with the solution-phase H^+ ions from water and/or, 2. GRR with $PtCl_4^{2-}$ ions from the precursor salt. The latter results in the formation of Pt NPs that rapidly alloy with the remaining seeding Co NPs in the solution to form the NAs. In the results presented here, the aforementioned reaction pathways are systematically driven by tuning the initial Pt salt concentrations and solution phase pH to synthesize Pt-Co nanoalloys with controllable size, atomic ratio and alloying degrees. In turn, we investigate the structure-property relations in a wide range of as-synthesized PtCo NAs by establishing the underlying relationship between their alloyed structures, compositions and ORR activities.

5.2 Results and discussion

5.2.1 Synthesis and characterization of PtCo NAs

5.2.1.1 PtCo NAs synthesized with different Pt salt concentrations

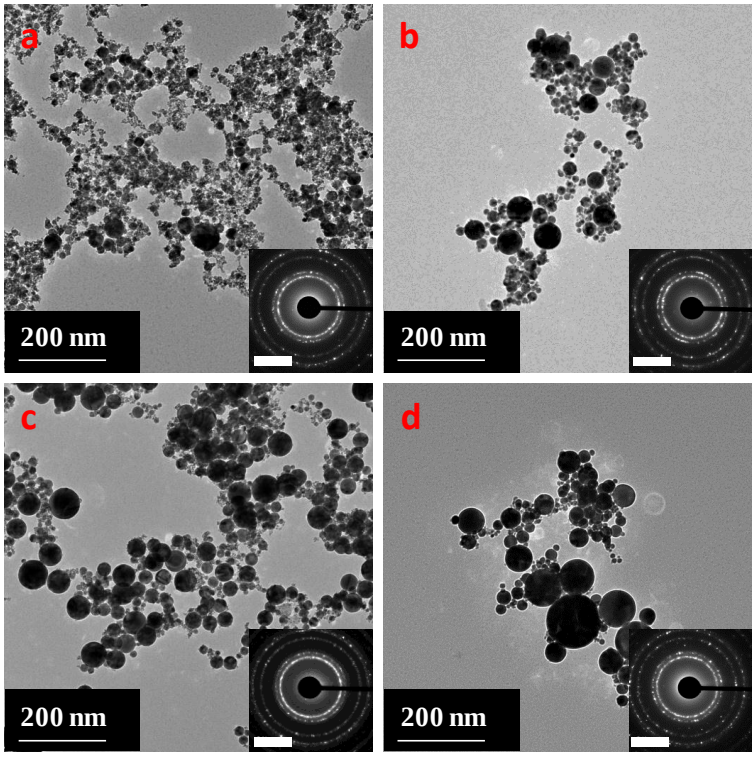


Fig. 5.1 **a-d.** TEM images along with the corresponding SAED patterns (insets) for the PtCo NAs: **a.** PtCo-1; **b.** PtCo-2; **c.** PtCo-3; **d.** PtCo-4 synthesized via LASiS-GRR at different initial K_2PtCl_4 concentrations (125 mg/l, 250 mg/l, 375 mg/l, 500 mg/l) with the respective ablation times of 4 min, 7 min, 13 min, 20 min. The scale bar in for SAED patterns is 5 (1/nm).

Table 5.1 Summary of degree of alloying for various PtCo NAs through LASiS-GRR.

	K_2PtCl_4 C (mg/l)	**Co ratio % (ICP-OES)**	**2θ (111)**	**Crystallite size (nm)**	**a (Å)**	**x**	**degree of alloying (%)**
pH 3	250	6.4	39.81	17.98	3.919	0.03	44.77
pH 7	125	20.6	40.20	3.16	3.882	0.12	53.33
	250	22.1	40.29	4.70	3.874	0.14	58.01
	375	19.9	40.13	9.00	3.889	0.10	46.57
	500	15.5	40.05	10.06	3.896	0.09	51.70
pH 11	250	38.1	40.85	4.15	3.828	0.26	55.96

The PtCo NA samples of PtCo-1, PtCo-2, PtCo-3, and PtCo-4, as synthesized by LASiS-GRR for various K_2PtCl_4 concentrations and ablation times (as described in the methods section), are depicted in the TEM images in Fig. 5.1 along with the corresponding SAED patterns (inset). It is noted here that the initial products from the LASiS-GRR synthesis were found to be alloyed PtCo NPs embedded in sponge shaped CoO_x matrices. As mentioned in the methods section of chapter 2, post-treatment of the as-synthesized $PtCo/CoO_x$ nanocomposite suspensions with HCl acid solutions at pH2 for 20 hours led to the complete removed of all CoO_x matrices leaving behind the pure spherical PtCo nanoalloys (NAs). These spherical PtCo NAs are found to exhibit clean PtCo characteristic diffraction rings as seen from SAED patterns in Fig. 5.1 insets. The particles are largely found to be spherical due to the surface atom reconstruction induced by laser irradiation [178]. TEM images in Fig. 5.1.a-d also indicate a systematic increase in the average particle sizes between the samples PtCo-1 and PtCo-4. Detailed mean crystallite sizes, as estimated from XRD data, are found to be ~3.16, 4.7, 9.00 and 10.06 nm for PtCo-1, PtCo-2, PtCo-3 and PtCo-4 samples respectively (Table 5.1). Mean crystallite sizes are calculated from the full width half maximum (FWHM) of the PtCo (111) peak in the XRD patterns (Fig. 5.2) by applying the Scherrer equation (described in details in the methods section). The augmentation of mean particle sizes with higher initial $[Pt^{2+}]$ is due to the larger degree of coalescence/Ostwald ripening among the seeding PtCo NPs due to faster reduction rates of the K_2PtCl_4 salt by the seeding Co NPs [60]. The alloying of Co into Pt is demonstrated by the clear shift of PtCo characteristic peaks to higher angles in the XRD patterns in Fig. 5.2, when compared to the corresponding 2θ values for pure Pt peaks. Specifically, the Pt (111) peak shifts from 39.8 ° for pure Pt to 40.20 °, 40.29 °, 40.13 ° and 40.05 ° for PtCo-1, PtCo-2, PtCo-3 and PtCo-4 NAs respectively is in accordance with the evolution of Co atomic ratios (%) of 20.6, 22.1, 19.9 and 15.5 in the respective alloys, as calculated from ICP-OES measurements (shown in Table 1). Table 5.1 also summarizes the values of Co atomic fractions in the alloys (x) and the ratio of alloyed Co (forming Pt_3Co) to total Co (Co_{al}/Co_{tot}), as

calculated from Vegard's law and ICP-OES measurement (details in the method section). These calculations reveal the alloying degrees to vary from ~44% to ~58% for the aforementioned respective PtCo NAs synthesized. Besides, the high resolution TEM image in Fig. 5.3.a indicates the surface facets of the specific PtCo-2 particle are dominated by the PtCo (111) that is well-known for its lower oxygen binding energy and hence, higher ORR activity [79,179,180].

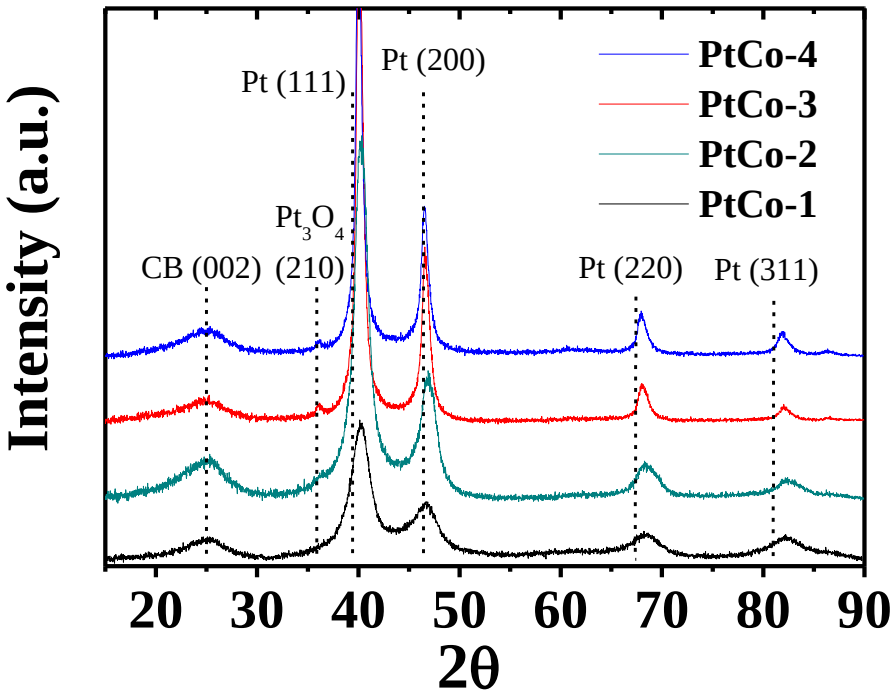


Fig. 5.2 Comparison of XRD patterns for various PtCo NAs synthesized at different initial K_2PtCl_4 concentrations and ablation times. The black dashed lines mark the standard 2 peak positions for the respective labeled species.

In an effort to further investigate the elemental distributions within the NAs from large-scale as well as detailed elemental mappings respectively, both energy dispersive X-ray spectroscopy (EDX) and electron energy loss spectroscopy (EELS) measurements are shown in Fig. 5.4 for the PtCo-2 sample. The EDX mapping results in Fig. 5.4.a-c reveal that both Pt and Co are uniformly distributed in all the NPs. Fig. 5.4.d shows a representative EELS spectrum taken from a single NP (shown in the inset), where the two groups of peaks with onsets located at ~519 and 779 eV are

ascribed to the Pt-$N_{2,3}$ and the Co-$L_{2,3}$ edges respectively. The corresponding Pt and Co EELS mapping for this particle are exhibited in Fig. 5.4.e and f, where the Pt distribution area (Fig. 5.4.e) is found to be slightly larger than that for Co (Fig. 5.4.f). For better comparison, the Pt:Co ratio mapping along with a representative line scan across the particle is shown in Fig. 5.4.g, and the corresponding Pt atomic (%) distribution across this line scan is shown in Fig. 5.4.h. These results reveal a thin Pt-rich layer (c.a. a few nanometers) as the particle shell wherein the Co (%) increases gradually towards inner layers. In contrast, the center of the NP bears a relatively uniform but lower Pt:Co ratio (Pt:Co = ~4.5:1). Here it needs to be mentioned that in spite of the higher accuracy of the EELS technique, the inclusion of other signals (e.g. O-K edge at 532 eV) and random noises in the broad Pt-$N_{2,3}$ peak from EELS data can contribute to the slightly higher value of the Pt:Co ratios as calculated from EELS measurements, when compared to that from EDX/ICP-OES quantifications.

In order to check the Pt:Co ratio at the edge of this NP, the EELS spectra at the top left corner and right edge of the NP in the EELS ratio mapping (Fig. 5.4.g) are illustrated separately in Fig. 5.5.a, b. The weak Pt-$N_{2,3}$ peak with small signal to noise ratio is found at the top left corner in addition with a suspected oxygen peak at 532 eV (K edge), therefore indicating the high Pt:Co ratio depicted by red color in that area is probably due to a small cluster of Pt atoms. In comparison, the signal to noise ratio in the EELS spectra of the Pt $N_{2,3}$ peak at the right edge is found to be much larger, thereby confirming the existence of high Pt:Co ratio at that spot. Besides, the Pt distribution in this particle is also confirmed by EELS mapping using Pt $M_{4,5}$ edge at ~2122 eV (Fig. 5.6). Overall, the result matches well to the Pt $N_{2,3}$ mapping with only 1-2 Å shift that is possibly due to the mechanical drifting.

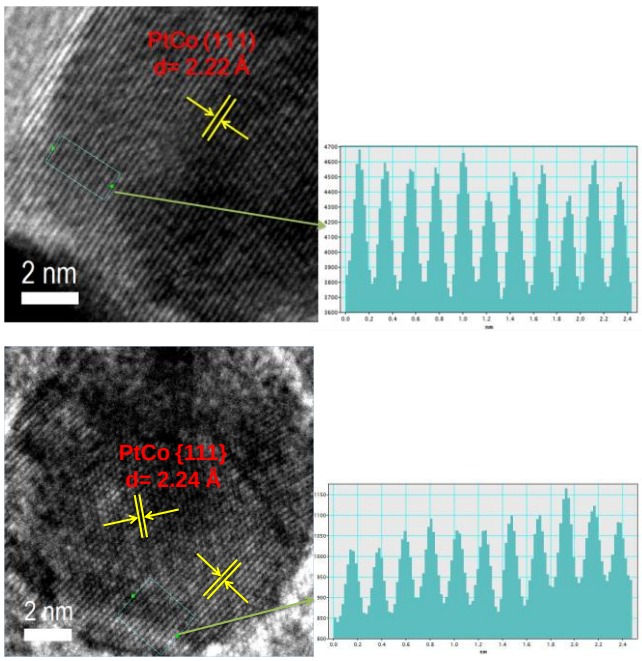


Fig. 5.3 HRTEM images of PtCo-2 (top) and the pH11 (down) samples.

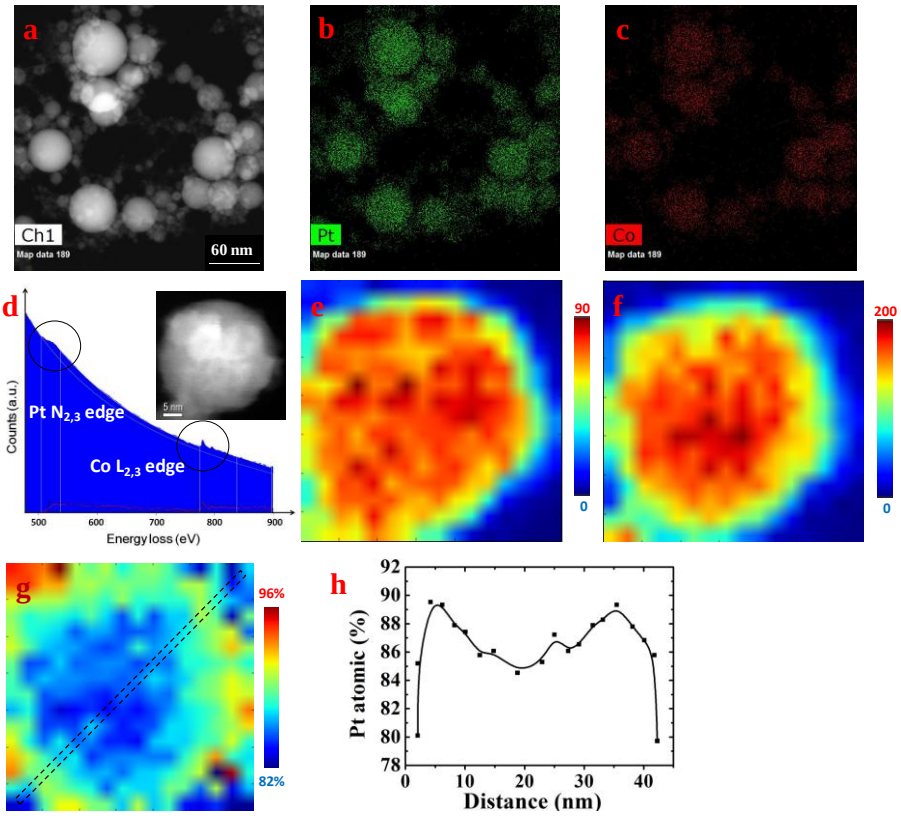


Fig. 5.4 EDX (**a-c**) and EELS elemental mapping results (**d-h**) for PtCo-2 sample showing: **a.** HAADF-STEM image; **b, c.** EDX mapping of Pt and Co for **a** on a large scale; **d.** EELS spectrum of a single particle shown in inset; **e, f.** EELS mapping of the corresponding Pt and Co; **g.** EELS mapping indicating Pt/Co atomic ratio from **e** and **f**; **h.** Pt atomic ratio (%) distribution across the line shown in **g**.

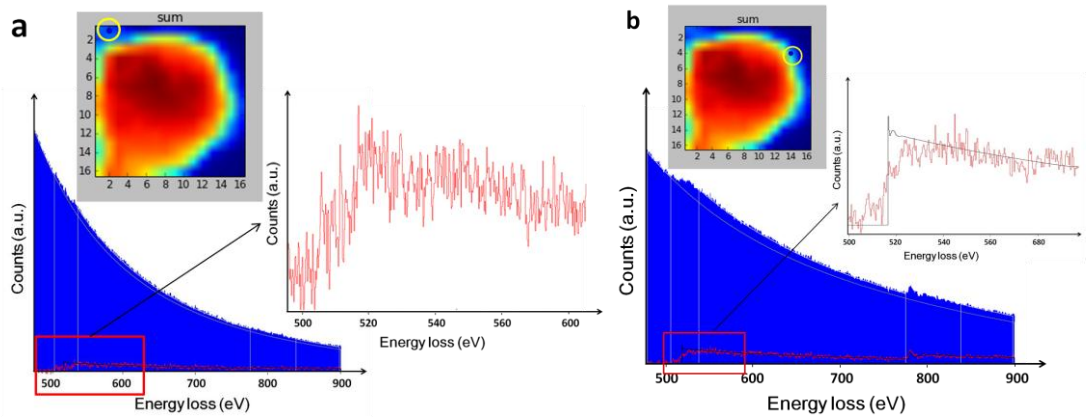


Fig. 5.5 EELS spectrum at the particle edge: **a.** the Pt-$N_{2,3}$ edge has low intensity and small signal to noise ratio, while an oxygen-K edge is distinct, which is possibly due to random noise or unexpected oxygen signal; **b.** an clear Pt-$N_{2,3}$ edge peak with high signal to noise ratio at the right edge of the NP.

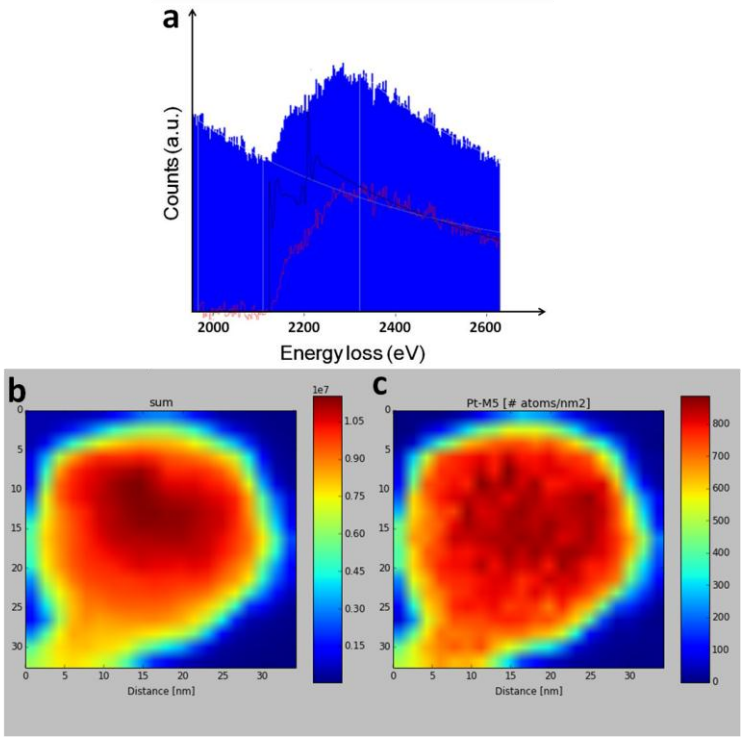


Fig. 5.6 EELS spectrum (**a**) and mapping (**c**) of the particle using Pt M-$_{4,5}$ edge.

5.2.1.2 PtCo NAs synthesized with different pH conditions

For investigating the impact of the solution phase [H^+] on the structure and composition of the resultant NAs, similar experiments were carried out at pH3 and pH11 conditions respectively (with initial [K_2PtCl_4] of 250 mg/l, and ablation time of 7 min) followed by HCl treatment at pH2 conditions. The PtCo NAs synthesized at pH3 show a much larger mean crystallite size (~17.98 nm) as compared to those at pH11 condition (~4.15 nm), as revealed by TEM images in Fig. 5.7.a, e and Table 5.1. This is due to the higher degree of coalescence for the Pt NPs in acid condition arising from the severe retardation in CoO_x formation. In contrast, under alkaline condition (pH11), part of the Pt^{2+} reacts with OH^- to generate $Pt(OH)_2$ that ends up forming $PtCl_2$ precipitates, as demonstrated by the XRD result in Fig. 5.8, following which both Pt formation and agglomeration rates are reduced. Specifically in this case, saturated NaCl solution was added into the products followed by centrifugation for two times to remove the unwanted $PtCl_2$ salts.

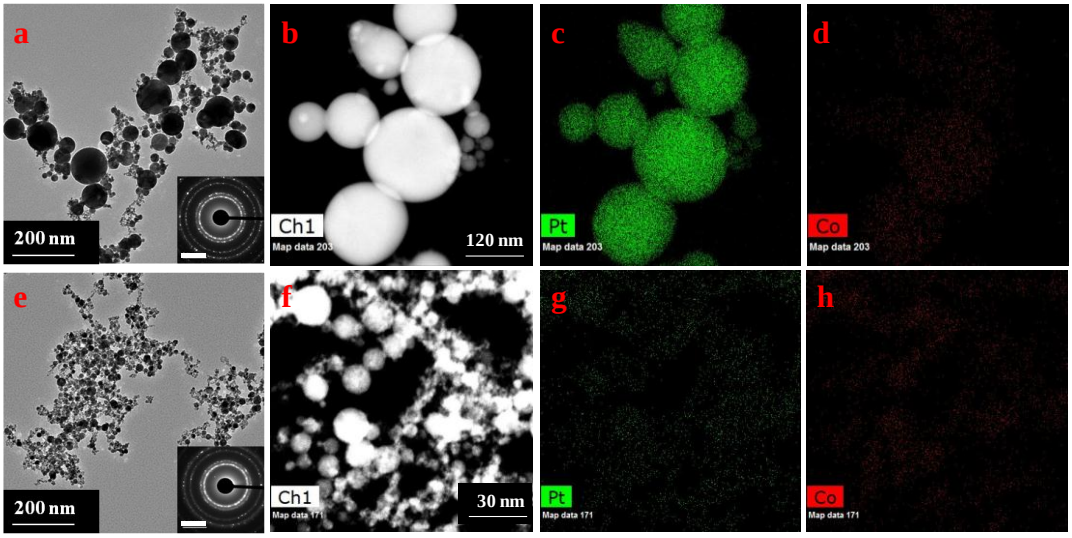


Fig. 5.7 Comparison of PtCo NAs synthesized via LASiS-GRR at acid (**a-d,** pH3) and alkaline (**e-h,** pH11) conditions. **a, e.** TEM images with the corresponding SAED patterns shown in the insets. (The scale bars in the insets are 5 /nm) **b, f**. HAADF STEM images; and **c, d, g, h.** the corresponding Pt and Co mappings for **b** and **f**.

The EDX elemental mapping indicates a much stronger intensity for Pt than Co for the pH3 sample in Fig. 5.7.b-d, as compared to the relatively stronger Co than Pt signal for the pH11 sample in Fig. 5.7.f-h. Detailed EDX spectra indicate the Co molar ratios to be 5%, 21% and 39% for the NAs obtained at pH3, pH7 (PtCo-2) and pH11 conditions respectively, as shown in Fig. 5.9.

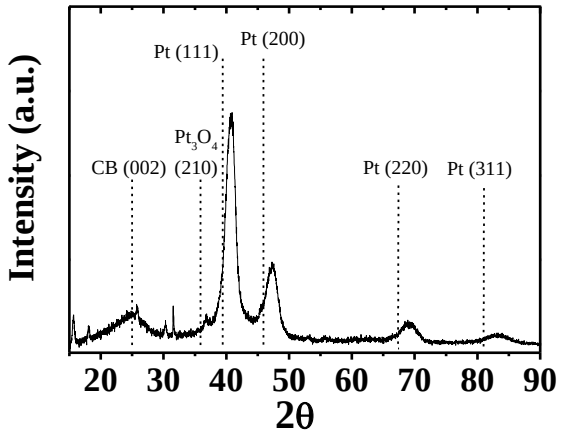


Fig. 5.8 XRD patterns for PtCo NAs at pH11 without NaCl wash. The dash lines mark the standard peak positions for each species.

Furthermore, the XRD profiles (Fig. 5.10) indicate negligible shift in 2θ value (39.81 °) for the characteristic PtCo (111) peak in the pH3 sample as compared to the remarkable positive shift (40.85°) in 2θ values for the PtCo alloy formed at pH11, that is much higher than those for the PtCo-2 sample (40.29 °) as well as for standard Pt_3Co (40.53 °) alloys. In such a case Pt_1Co_1 alloy (41.4 °) with tetragonal crystalline structure might have been partially formed. The aforementioned results for different and yet, directed alloying under different pH conditions are achieved by controlling the relative concentrations of Pt^{2+}, Co and H^+ in the system, as also discussed in details in the next section. Specifically, in acid condition, majority of the Co NPs undergo direct oxidation by solution phase [H^+], which results in fewer amounts of Co available for Pt^{2+} reduction and even less available for alloying with Pt. On the other hand, at pH11 condition, direct oxidation of Co is hindered due to the extremely low [H^+] in solution. As a consequence, large amount of Co take part in GRR with Pt^{2+} and in turn alloying with Pt, leading to a much higher Co_{al} in the final products.

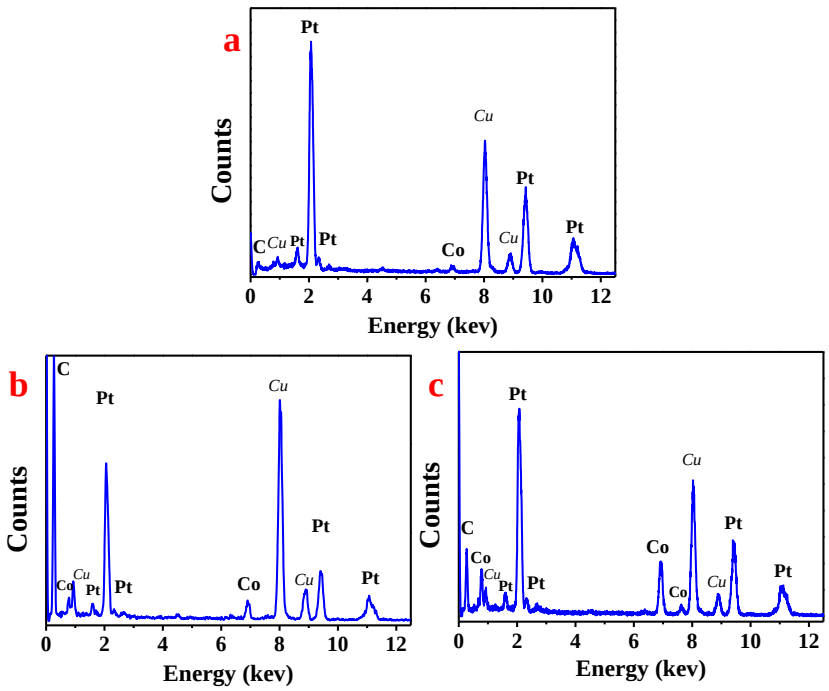


Fig. 5.9 EDX images for PtCo NAs obtained at **a.** pH 3, **b**. pH7 (PtCo-2) and **c**. pH11. The Cu signal is from the substrate. The Co atomic ratios are quantified to be 5%, 21% and 38% respectively.

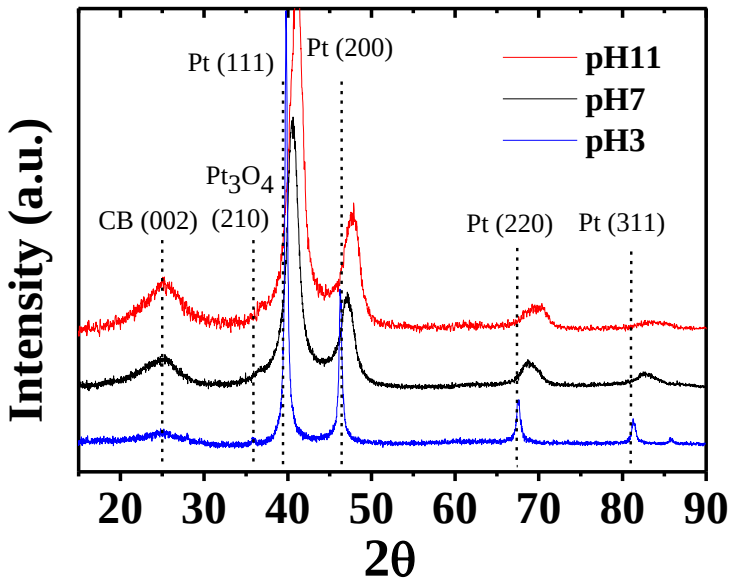


Fig. 5.10 XRD patterns for PtCo NAs at different pH conditions with same initial K_2PtCl_4 concentration and ablation time (250 mg/l and 7 min). The dash lines mark the standard peak positions for each species.

5.2.2 Investigation of ORR electrocatalytic activities

The ORR catalytic activities for the PtCo NAs synthesized with various initial [Pt^{2+}], as investigated with RDE measurements in 0.1 M $HClO_4$ electrolyte solutions, are summarized in Fig. 5.11. Cyclic voltammetry (CV) scans were conducted from 0.05 to 1.02 V vs. RHE at a scan rate of 50 mV/s. The ECSA calculated from the integration of the hydrogen evolution area in the CV curve indicate a gradual decrease from PtCo-1 to PtCo-4 (i.e., 30.92, 24.25, 18.31 and 14.55 m^2/g respectively), as shown in Fig. 5.11.a and Table 1. This is mainly attributed to the decreasing surface to volume ratios with increasing particle sizes of the PtCo NAs resulting from LASiS-GRR with higher initial [Pt^{2+}]. Fig. 5.11.b provides the ORR polarization curves scanned in O_2-saturated 0.1 M $HClO_4$ electrolyte for the PtCo catalysts under study. The half-wave potential values in Fig. 5.11.b indicate that most of the as-synthesized NA samples, i.e., PtCo-1, PtCo-2 and PtCo-3 outperform the catalytic activities of commercial Pt/C (see Table S1). The best ORR performance is noted for PtCo-2 sample with a 32 mV positive shift in the half-wave potential as compared to the Pt/C sample. This is mainly due to higher Co ratios with good alloying degree (58.01 %) in the PtCo-2 sample that shrinks the lattice constant and lowers d-band center which in turn reduces the oxygen binding energy. Added to this, the small particle sizes (mean crystallite size of 4.7 nm in Table 5.1) with moderate coalescence in PtCo-2 promote catalytic activities due to higher surface to volume ratios. In contrast, the PtCo-4 alloy exhibits the lowest activity, which can be ascribed to its lowest Co ratio (15.5 %), poor alloying (51.7 %) and largest size (~10 nm) as seen from Table 5.1. Interestingly, the PtCo-1 sample with smallest mean sizes (~3 nm) and slightly lower alloying degree (53.33%) than PtCo-2 (58%), exhibit less activity. This could be primarily attributed to the excess agglomeration in PtCo-1. Besides, the diffusion-limited current at high overpotential regions (+0.1 to +0.80 V vs. RHE) reaches ~5.6 mA/cm^2 for all samples, thereby indicating minimal formation of H_2O_2 during the ORR process as well as good charge transfer rates. It is noted that this

diffusion-limited current value agrees extremely well with those reported for commercial Pt/C and other peer research works [118,181]. The dynamics of the electron transfer process during ORR were analyzed using the Koutecky-Levich (KL) equation in rotating disk voltammetry (RDV) measurements carried out at different rotation rates (400 to 2200 rpm), as indicated in the experimental section. Fig. 5.11.c shows the slopes of the KL plots generated from the RDV curves (inset) for the PtCo-2 in the range of 0.70–0.87 V. The slopes estimate the number of transferred electrons (n) to be ~4.0, thereby indicating an ideal four-electron transport process for ORR. Fig. 5.11.d illustrates the Tafel plots extracted from the ORR polarization curves in the mixed kinetic/diffusion regions (low overpotential regions). The calculated Tafel slopes for the PtCo samples are in the range from 56.4 to 67.4 mV/dec, which are lower than the corresponding values for commercial Pt/C (70.5 mV/dec), indicating better charge carrier mobility. Besides, upon comparing the specific activities (SA) for each of the samples at 0.9 V vs. RHE potential on the Tafel plots in Fig. 5.11.d, all the PtCo samples are found to indicate higher SA values than the Pt/C sample. The detailed mass activity (MA) and SA values at 0.9 V vs. RHE are shown in Fig. 5.11.e and Table 5.2. The PtCo-2 sample is found to indicate the best catalytic activity with the MA and SA values of 0.28 $mA/\mu g_{Pt}$ and 1.18 mA/cm^2 respectively, thereby indicating c.a. 3 and 6-fold increase over the corresponding values for Pt/C (0.09 $mA/\mu g_{Pt}$ and 0.19 mA/cm^2). The outstanding ORR activities for the PtCo NAs is attributed to the uniform NAs with the Pt-rich shell, as evident from the EELS ratio mapping in Fig. 5.4.g and h. Added to this, the absence of any additional chemical including reducing agent/surfactant/stabilization agent during the LASiS-GRR synthesis process eliminates the possibilities of deteriorating the active surface area, thereby benefiting the catalytic performance. Finally, stability tests were conducted for the PtCo-2 sample by scanning CV at the same range as earlier CV tests for 5000 cycles at 100 mV/s. The results shown in Fig. 5.11.f reveal a ~14% decrease in ECSA (from 100 % (black) to 86.2 % (green) case) after 5000 cycles, while the Co_{al} also diminishes from 22.1% to 18.3%.

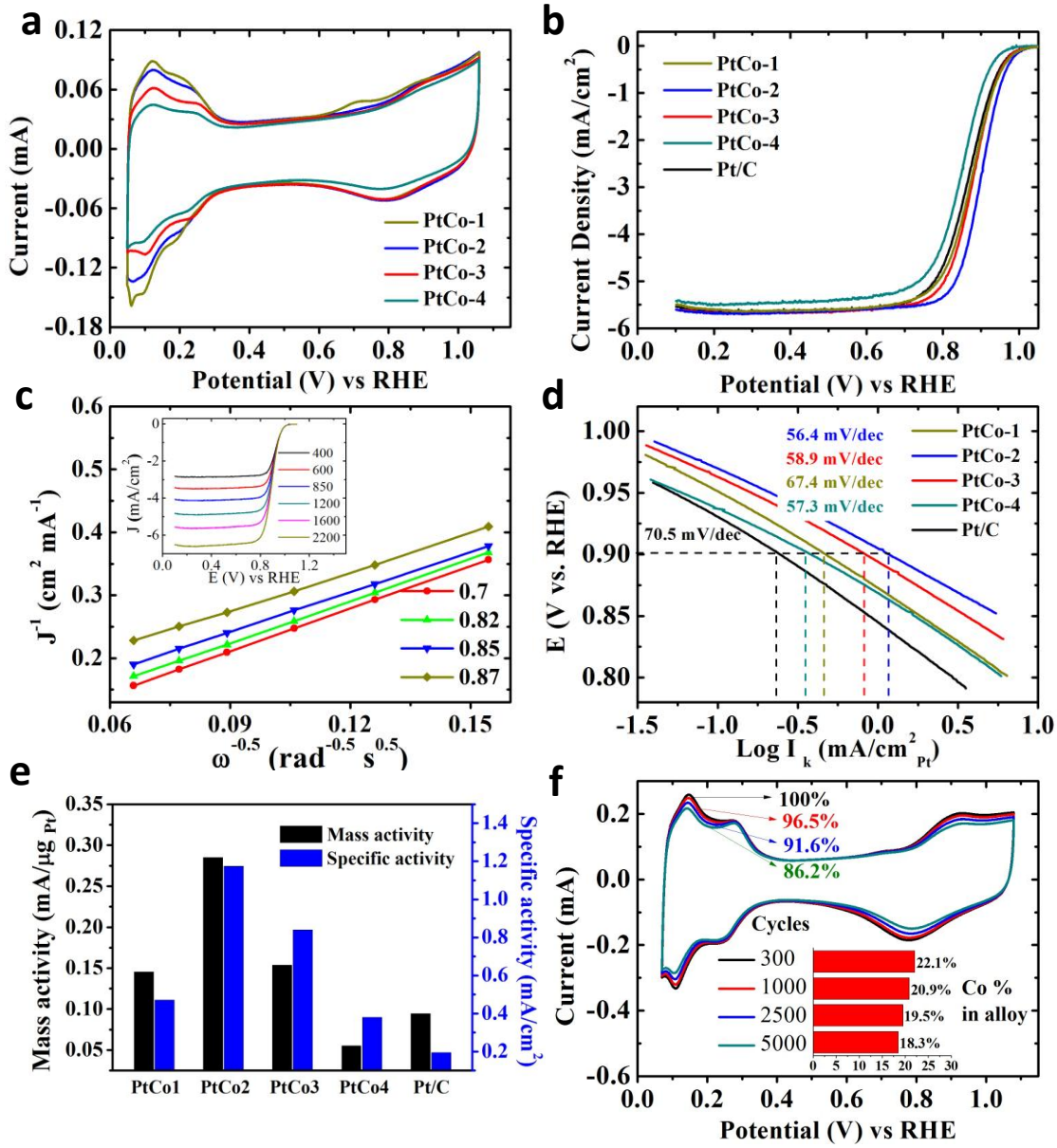


Fig. 5.11 Electrochemistry data indicating ORR activities of PtCo NAs made via LASiS-GRR when compared to commercial Pt/C samples using: **a.** Cyclic voltammetry curves at a scan rate of 50 mV/S; **b.** Linear sweep voltammograms for ORR polarization curves in 0.1 M $HClO_4$ electrolyte saturated with dissolved O_2 at 1600 rpm and scan rate of 5 mV/s; **c.** Koutecky-Levich plots from rotating disk voltammogram (RDV) data (shown in inset) for PtCo-2 at different potentials (0.70-0.87 V) indicating four electron transport process for ORR; **d.** Corresponding Tafel plots; **e.** Comparison of mass activity and specific activity at 0.9 V vs. RHE; **f.** Cyclic voltammetry curves indicating the % ECSA values and Co ratio (%) in the alloy after various numbers of potential cycles at a scan rate of 100 mV/s.

This is ascribed to the dissolution of catalysts in the acid electrolyte, which is a well-known phenomenon for Pt or other metal based ORR catalysts as also observed in earlier works [79,106,113,123]. Our on-going work is aimed towards addressing this long-standing issue via thermal annealing at high temperature (700 C^o) for transferring the current disordered Pt_3Co to the more stable ordered alloy.

Table 5.2 Summary of electrochemistry test results.

	Pt loading (µg/cm2)	ECSA (m2/g)	I_k at 0.9 V (mA/cm2)	MA (A/mg)	SA (mA/cm2)	Half-wave E (mV vs. RHE)
PtCo-1	19.85	30.92	2.89	0.15	0.47	875
PtCo-2	19.48	24.25	5.55	0.28	1.18	899
PtCo-3	20.03	18.31	3.08	0.15	0.84	879
PtCo-4	21.13	14.55	1.17	0.06	0.38	847
Pt	25.00	48.50	2.36	0.09	0.19	867
pH 3	23.40	6.67	0.62	0.03	0.40	806
pH 11	15.48	44.50	3.65	0.24	0.53	875

The electrochemistry results for the PtCo NAs synthesized at different pH conditions (referred to as pH3, pH7 and pH11 samples) are summarized in Fig. 5.12. The pH11 sample exhibits a much higher ECSA (44.50 m^2/g) than the pH7 or PtCo-2 (24.25 m^2/g) and pH3 sample (6.67 m^2/g) as calculated from the hydrogen adsorption peaks in the CV curves (Fig. 5.12.a). This is easily attributed to the smaller crystallite sizes (~4.15 nm from Table 5.1) for the pH11 sample as compared to both the pH7 (~4.70 nm) and pH3 (~17.98 nm) samples. For comparing the ORR activities, electrochemistry tests and plots similar to the ones carried out for PtCo-2 samples at pH7 condition are presented in Fig. 5.12. These measurements include ORR polarization curves (Fig. 5.12.b), Tafel plots (Fig. 5.12.c) and MA/SA comparisons (Fig. 5.12.d). The pH3 sample exhibits the poorest activity as compared to all the other samples, which can be ascribed to its larger crystallite sizes and extremely low Co_{al}. Here the interesting observation is that the pH11 sample, even with higher Co_{al} (~38.1 %) and smaller crystallite sizes (~4.15 nm), exhibit slightly less ORR activities in regards to the half-wave potential (~875 V vs. RHE), MA (~0.24 A/mg) and SA

(~0.53 mA/cm^2) when compare to the corresponding values for PtCo-2 (namely, 899 V vs. RHE, 0.28 A/mg and 1.18 mA/cm^2). Nevertheless, it needs to be noted that these values are still remarkably better than those for commercial Pt/C (namely, 867 V vs. RHE, 0.09 A/mg and 0.19 mA/cm^2, respectively).

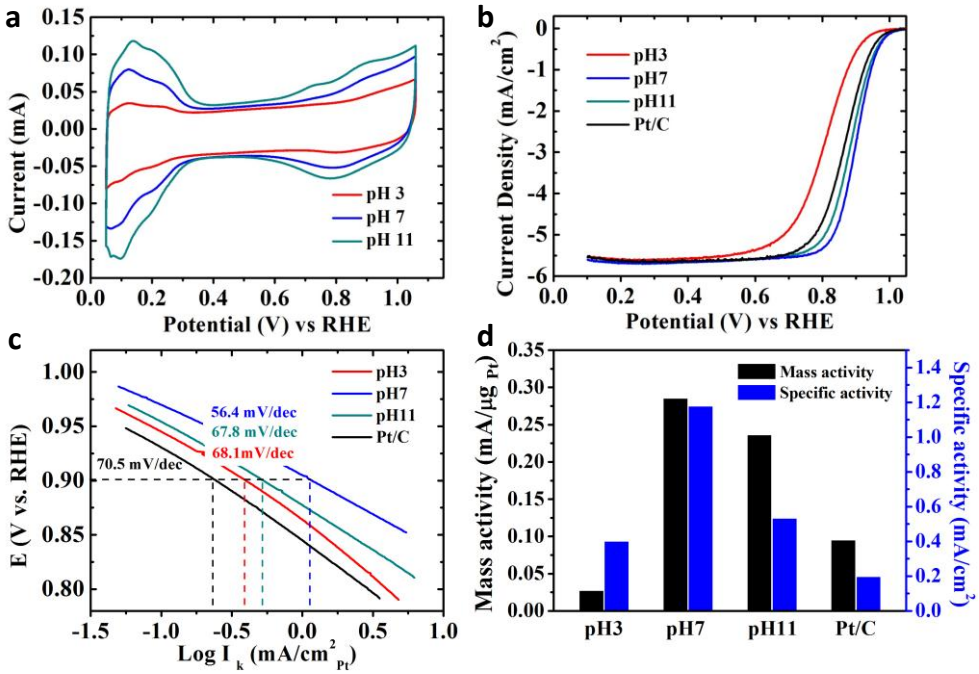


Fig. 5.12 Electrochemistry data for PtCo NAs made from LASiS-GRR at different pH conditions: **a.** Cyclic voltametry curves at a scan rate of 50 mV/S; **b.** Linear sweep voltammograms for ORR analysis in 0.1 M $HClO_4$ electrolyte saturated with dissolved O_2 at 1600 rpm and scan rate of 5 mV/s; **c.** The corresponding Tafel plots; **d.** Comparison of mass activity and specific activity at 0.9 V vs. RHE.

5.2.3 Reaction Pathways for PtCo NA formation: A discussion

In an effort to elucidate the role of LASiS-GRR in tailoring the degree of alloying/composition, structure, and in turn, the ORR activities of the aforementioned PtCo NAs, we dedicate this section towards explaining the detailed mechanistic picture behind the reaction pathways that lead to the formation of various PtCo NAs during LASiS-GRR. The concept of tandem LASiS-GRR is built on the ability to control the various reduction reaction pathways via GRR at the plasma cavitation-liquid interface that are essentially initiated by the rate-limiting source production of Co NPs via LASiS. In doing so, we tune the amount of reduced Pt NPs

that alloy with the seeding Co NPs, thereby tailoring the composition, structure and degree of alloying in the resulting NA samples. Thus, different extents of alloying in the aforementioned PtCo NAs and in turn their catalytic properties are systematically controlled in a simple yet, elegant fashion by tuning the relative rates of the following reaction mechanisms and pathways, as illustrated in the schematic in Fig. 13 for different initial Pt^{2+} and H^+ (pH conditions) concentrations. In O_2-free solution, the pulsed laser produces seeding Co NPs within the cavitation bubble that undergo the following reactions at the bubble-liquid interface during collisional quenching:

1. Galvanic replacement reaction (GRR) with K_2PtCl_4 based on the respective redox potentials for Co/Co^{2+} (-0.28 V vs. SHE) and Pt^{2+}/Pt (0.76 V vs. SHE):

$$Pt^{2+} + Co \rightarrow Pt + Co^{2+} \qquad \text{Reaction 1}$$

2. Oxidation by H^+ ions driven by pH:

$$Co + 2H^+ = Co^{2+} + H_2 \qquad \text{Reaction 2}$$

3. Alloying with reduced Pt from Reaction 1:

$$Co + Pt = PtCo(alloy) \qquad \text{Reaction 3}$$

At neutral conditions (pH = 7), with same Co production rate from the rate limiting steps of LASiS, the initial $[Pt^{2+}]$ plays a crucial role in driving the rate determining steps of reactions 1 through 3 to finally control the nanostructures and compositions. Specifically, when the initial $[Pt^{2+}]$ is low, the reduction rate of Pt through GRR (reaction 1) is much slower than the direct oxidation of Co by H^+ (reaction 2), therefore the alloying rate between reduced Pt and Co (reaction 3) is also slow. On the other hand, high initial $[Pt^{2+}]$ leads to a much faster reaction 1 than the other two reactions, therefore leaving few Co to alloy with large amount of reduced Pt and hindering the alloying process. To this end, an optimal amount of initial $[Pt^{2+}]$ is expected to produce the largest alloyed Co (Co_{al}).

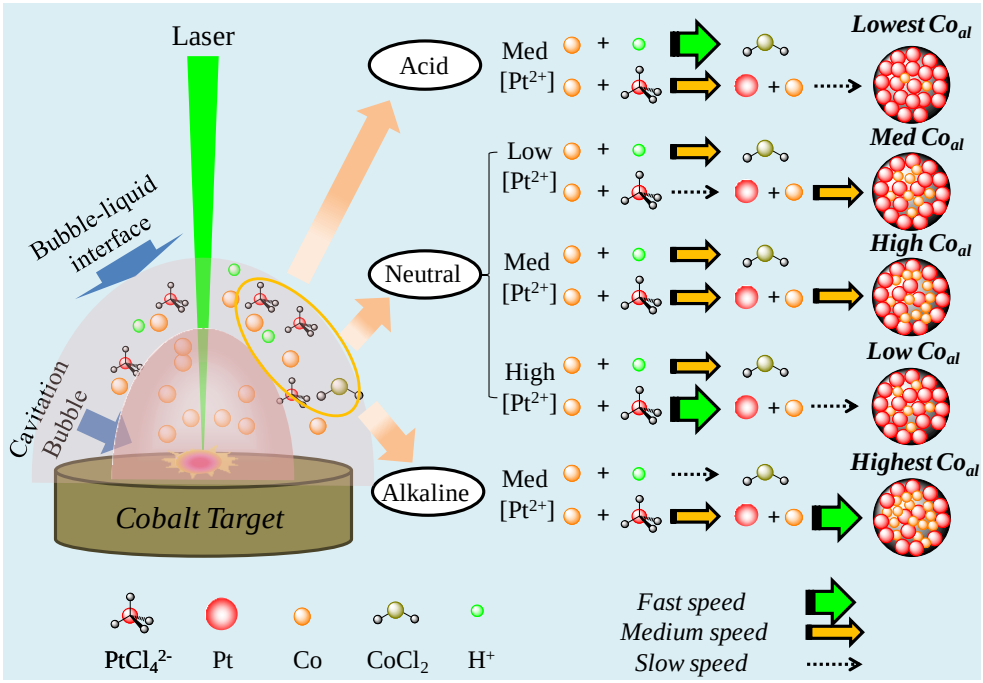


Fig. 5.13 Schematic diagram indicating the formation of PtCo NAs via tandem LASiS-GRR using different initial Pt^{2+} concentrations and pH conditions; pulsed laser produces seeding Co NPs which expand with the cavitation bubble and react with either Pt^{2+}, H^+ or reduced Pt (alloying process) at the bubble-liquid interface during collisional quenching. Based on the different Pt^{2+} concentration (low, medium, high) and pH conditions (acid, neutral, alkaline), different degrees of alloying for Co_{al} are obtained.

Meanwhile, the Pt-Co alloying process is also controlled by tuning the solution phase $[H^+]$ or pH conditions. Specifically, in acid conditions (low pH), an extremely low Co_{al} is expected since majority of the seeding Co NPs go through reaction 2 leaving few Co for reaction 3, which is similar to the case with low $[Pt^{2+}]$ at neutral condition. On the other hand, in alkaline conditions (high pH) with medium $[Pt^{2+}]$, abundant Co are present for reaction 3, in which case the highest Co_{al} is obtained. The aforementioned reaction mechanisms are also schematically represented in Fig. 5.13 for different $[Pt^{2+}]$ concentrations (low, medium, high), pH conditions (acid, neutral, alkaline) and corresponding relative speeds of the reaction pathways, namely, fast (big, bold green), medium (bold orange) and slow (dotted black).

5.2.4 Theoretical Modeling of Rate Kinetics

The reaction rates expressions have been shown in section 2.3.4, by applying Runge-Kutta method, theoretical modeling was constructed regarding the aforementioned four PtCo NA samples, namely, PtCo-1, PtCo-2, PtCo-3 and PtCo-4. The fitting results are shown in Fig. 5.14, where the green hollow dots reveal the experimental data of the [Pt^{2+}] evolution during laser ablation. The theoretical trends for the [Pt^{2+}] evolutions match with the experimental data in overall for the four different cases, especially at the beginning stages. However, at a later stage, i.e., after 50% reduction of [Pt^{2+}], the theoretical values drop down at a faster speed, which is probably due to the mass loss during the centrifugation and decanting processes thereby lower down the actual amount of reduced Pt(Co) NPs.

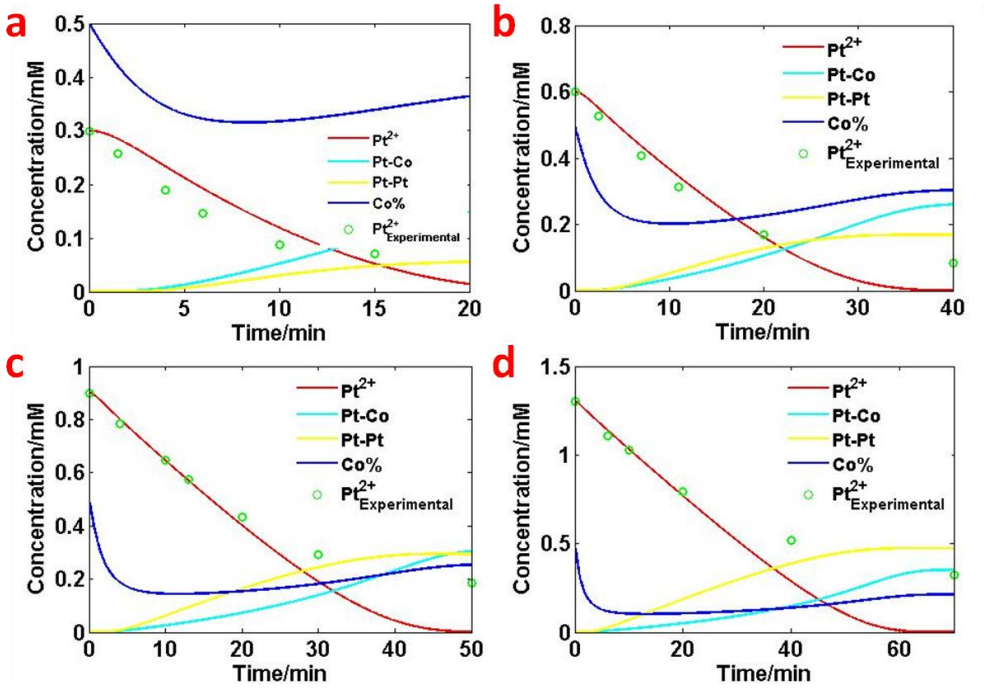


Fig. 5.14 Theoretical modeling of rate kinetics of LASiS-GRR on Co in K_2PtCl_4 solutions for the aforementioned four samples: **a.** PtCo-1; **b.** PtCo-2; **c.** PtCo-3; **d.** PtCo-4. The green hollow dots show the experimental [Pt^{2+}] evolution results, the blue lines reveal the atomic Co ratio in the PtCo alloy.

The blue lines indicate the atomic Co ratio in the PtCo alloy, which is calculated

from the numbers of Pt-Pt and Pt-Co bonding. The results imply a continuous decrease for the Co% from PtCo-1 to PtCo-4, which is slightly different from our experimental results via ICP-OES and EDS, where the values first increase from PtCo-1 to PtCo-2 then decline latter on, as summarized in Fig. 5.15. The inconsistency here can be possibly ascribed to PtCo-1 with low initial [Pt^{2+}] and less ablation time hence much lower concentration went through excess acid wash that dramatically dissolute alloyed Co. Besides, we hypothesized the solution phase pH is a constant (though in the real case it varies), while the model here only focused on the reaction rate kinetics without consideration of the more complicated nucleation processes as well as the laser irradiation effect. All those factors can drastically influence the accuracy of the results.

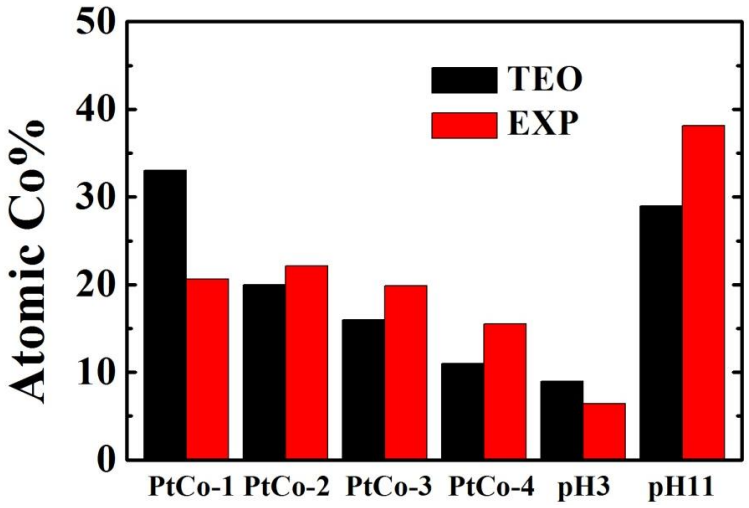


Fig. 5.15 Comparison of the theoretical and experimental values of atomic Co% in the four PtCo NAs.

In addition, we also applied the modeling for the pH3 and pH11 conditions as well as with continuous supply of K_2PtCl_4 salts respectively, as summarized in Fig. 5.16. Before setting up the modeling parameters (e.g., the solution phase pH), we first measured the pH change during the LASiS-GRR process. As can be seen from Table 5.3, at acid condition (pH3), the solution pH quickly increases to 5 after 1 min, then continuous to go up and stabilize at 8 within 3min. For the pH7 sample, the solution phase pH rapidly rises up to 9 within 1min and then become steady. When starting up

in an alkaline condition, the pH always keeps at 11. This is due to the reaction between seeding Co and water (H^+, to be specifically), which ends up forming $Co(OH)_2$ with limited solubility in water. Therefore, the high production rate of seeding Co during LASiS quickly lead to saturation of $Co(OH)_2$ in solution, in such a case pH also reaches equilibrium in a rapid speed. It needs to be mentioned that the more acidic final pH (pH8) for the initial pH3 condition is due to the higher [Co^{2+}] in solution (since a large portion of [Co^{2+}] is formed from direct oxidation of Co by excess H^+) that drive the reversible reaction $Co(OH)_2 \Leftrightarrow Co^{2+} + 2OH^-$ to the left side; on the other hand when starting with pH11, less [Co^{2+}] formation is anticipated, thereby the reaction is driven to the right and the final pH is higher.

Table 5.3 pH progression during LASiS-GRR on Co in K_2PtCl_4 with different initial pH values.

Time (min)	Measured pH		
	pH3	pH7	pH11
0	3	7	11
1	5	9	11
3	8	9	11
10	8	9	11

In order to simplify the modeling, we adopted the final pH values in each case for a comparison. From Fig. 5.16.aandb, the overall trend for the Co% matches with the experimental data, i.e., pH11 >pH7 >pH3, though the difference between each sample is smaller than the real case (see the detailed values summarized in Fig. 5.15). Such a modeling confirms our prior hypothesis of the pH influence on the alloy ratio. In addition, we also simulate the LASiS-GRR process with continuous supply of Pt salt. As can be seen from Fig. 5.16.candd, with injection rate of 10.6 mg $L^{-1}min^{-1}$, the system reaches the equilibrium where [Pt^{2+}] and Co% flat out with time. This will benefit our future research work for the potential mass production.

In future, we plan to apply this LASiS-GRR technique to a more universal alloy system along with efforts directed towards mass production by using different types

of laser (pulsed/continuous laser, different laser energy, wavelength, duration time, etc.) and a continuous supply of metal salts through the injection unit in the designed multifunctional cell. As a result, a green, facile and yet efficient synthesis technique for the mass production of various metal alloys with controllable physic-chemical and catalytic properties are expected to be realized.

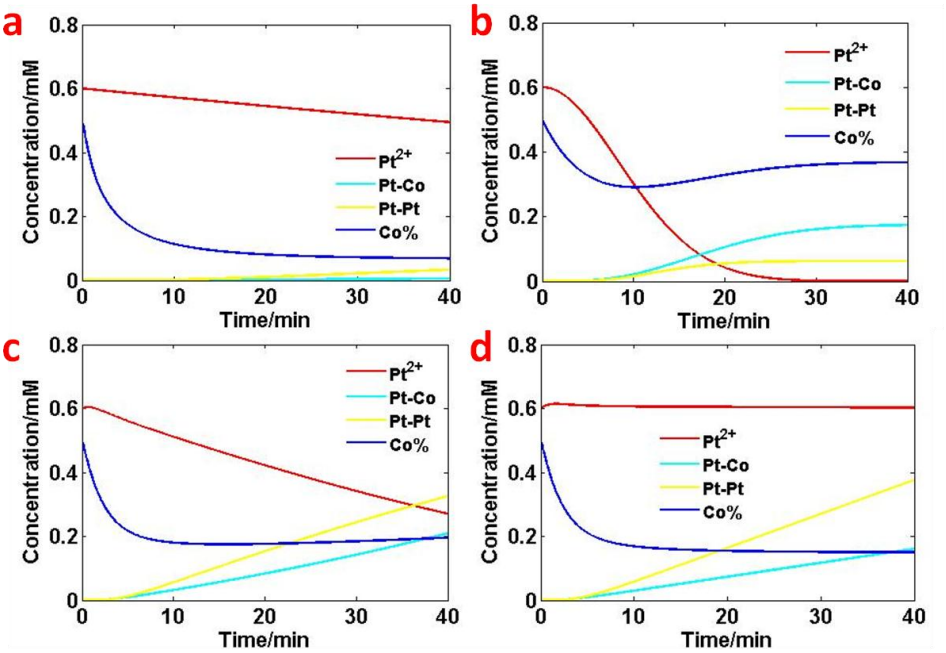


Fig. 5.16 Theoretical modeling of rate kinetics of LASiS-GRR on Co in K_2PtCl_4 solutions at pH3 (**a**) and pH11 (**b**) conditions as well as with continuous supply of K_2PtCl_4, where the injection rates are 7 and 10.6 mg $L^{-1}min^{-1}$ for the (**c**) and (**d**) respectively.

5.2.5 DFT calculation

The ORR activity for the (111) facet of the best catalyst under previous study, i.e., PtCo-2 with a Pt-rich core-shell (CS) structure has been evaluated and compared with pure Pt along with an ideal CS-Pt/Pt_3Co structure using the density functional theory (DFT). The model was constructed on a 3 × 3 unit cell slabs at the RPBE lattice constant of Pt (4.02 Å) comprising of a pure Pt shell and a uniform disordered PtCo alloy (22% atom. Co), as can be seen in Fig. 5.17.a. The bottom layers were fixed, and the top layer was allowed to relax, and the dipole correction was used in all cases. Thereafter, oxygen and hydroxide binding energies at two different positions, namely,

on top of Pt and at the hollow position (Fig. 5.17.b-e) were calculated accordingly.

Meanwhile, the Pt-Co alloying process is also controlled by tuning the solution phase [H^+] or pH conditions. Specifically, in acid conditions (low pH), an extremely low Co_{al} is expected since majority of the seeding Co NPs go through reaction 2 leaving few Co for reaction 3, which is similar to the case with low [Pt^{2+}] at neutral condition. On the other hand, in alkaline conditions (high pH) with medium [Pt^{2+}], abundant Co are present for reaction 3, in which case the highest Co_{al} is obtained. The aforementioned reaction mechanisms are also schematically represented in Fig. 5.13 for different [Pt^{2+}] concentrations (low, medium, high), pH conditions (acid, neutral, alkaline) and corresponding relative speeds of the reaction pathways, namely, fast (big, bold green), medium (bold orange) and slow (dotted black).

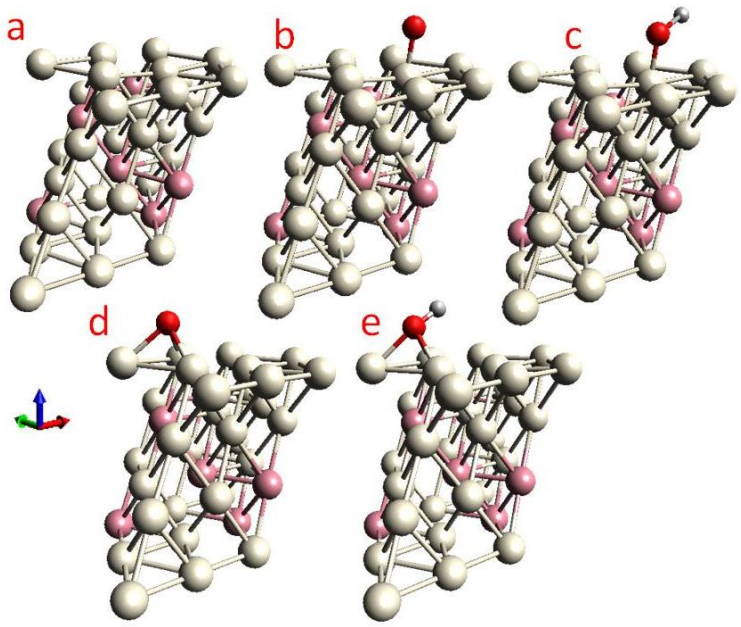


Fig. 5.17 Solvated surface structures on CS-Pt/PtCo (22%Co) (111) in a 3 ×3 unit cell for O/OH adsorption at different positions: **b, c,** on top of Pt; **d, e,** at hollow positions.

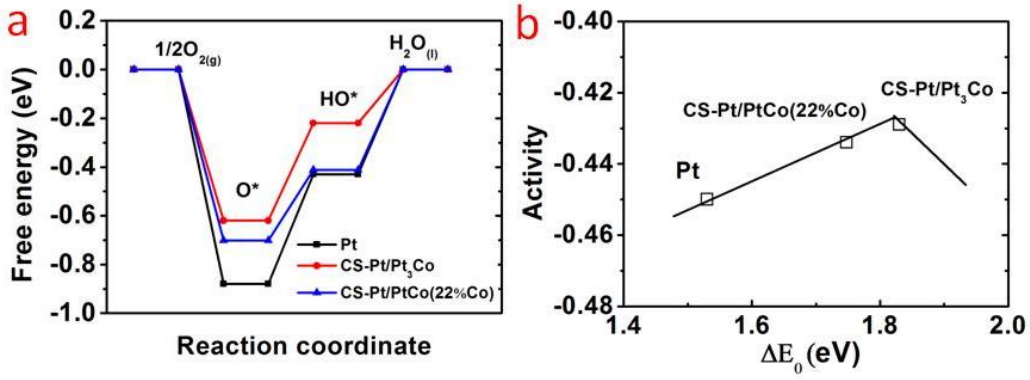


Fig. 5.18 **a**, Comparison of free energy changes during ORR; **b**, Activity volcano plot for ORR as a function of ΔE_O.

5.3 Summary

In this chapter, we report LASiS-GRR as a green, facile synthesis technique for the manufacturing of PtCo NAs as excellent ORR catalysts with controllable size, atomic compositions and alloying degrees. Specifically, the PtCo NAs with crystallite sizes of ~4.70 nm and ~58 % degree of alloying (~22 % reduction in Pt atomic content) exhibit superior ORR activities in acid electrolyte solutions as compared to the corresponding activities for standard Pt/C catalysts. Such activities are attributed to the unique capabilities of tandem LASiS-GRR to synthesize the aforementioned NAs with controlled sizes and uniform elemental distributions. Specifically, detailed structural characterizations of the NAs from EDX and EELS ratio mappings indicate a thin layer of Pt-rich shell on an alloyed core with relatively uniform Pt:Co ratio. The rational tuning of such structure-property relations are achieved by systematically controlling the initial Pt salt concentrations, ablation times and solution phase pH conditions during the LASiS-GRR technique. The transformative concept here is the ability of seeding NPs generated by the rate limiting step of LASiS to drive the simple redox chemistry in the rate controlling step of GRR that allows directed tailoring of sizes, structures and alloying/compositions in the final NCs/NAs. When operated in tandem, reaction pathways emerging from high-energy liquid-confined plasma can be regulated to create heteronanostructures with metastable structures and phases without the use of any external chemical agents/surfactants. Finally, simulation of the rate

kinetics of the LASiS-GRR process confirms part of our proposed mechanism, meanwhile provides the estimation for the injection rate of Pt salt in a continuous supply system towards mass production. Finally, DFT calculation theoretically confirmed our synthesized catalysts in term of high ORR activity.

Chapter 6 Future works with preliminary results: Synthesis of plasmonic nanocomposites for photocatalytic applications and other complex intermetallic nanomaterial systems

6.1 Synthesis of plasmonic nanocomposites for photocatalytic applications

6.1.1 Plasmonic nanocomposites: An introduction

Surface Plasmons (SP) are oscillations of coherent delocalized electrons that go through collective excitations at metal-dielectric interfaces.[135,138,183–186] Materials with surface plasmonic properties can be used for detecting chemicals and bio-molecules, photothermal cancer therapy, drug delivery, surface-enhanced Raman spectroscopy, photovoltaic cells, and solar fuel generation systems, etc.[187–197] When stimulated by an incident electromagnetic wave, the Plasmon oscillation becomes resonant. Such a surface Plasmon resonance (SPR) is generated when the inherent frequency of the oscillation against the nuclei restoring force equals to that of the incident light.[138,185] One remarkable features for those excited electron gas is the quantum effects, including quantum confinement,[198,199] quantum tunneling,[200,201] and nonlocal response,[202,203] that collaborate result in SPR only occurring on very small nanostructures, meanwhile the resonance frequency also vary with particle size.

The most famous plasmonic nanomaterials are Au and Ag, which are contributed by their natural SPR wavelength at the visible range along with low tendency to degrade.[133–136,138,193,204–207] Therefore, a number of research work have been carried out for adding them into photoactive materials by either physical mixing or chemical doping with the purpose of enhancing light harvesting.[133,135,136,208–210] Among which

forming core-shell geometry draws great attention to researchers and is considered as an effective route to endow those plasmonic properties for the light absorbance of another material, namely, either a dielectric medium or another kind of metal NP.[133,135,136,193,206,209] In such cases, SPR becomes localized, i.e., localized surface Plasmon resonance (LSPR), which is considerably dependent on the interfacial interactions between the plasmonic material and the surrounding media in terms of the resonance frequency and intensity.[133,136,206] As a result, the LSPR becomes tunable and can be optimized for specific applications.

Characterizations for the SPR mainly include UV-Vis absorbance on a large scale and, electron energy loss spectroscopy (EELS) for the small scale analysis.[198–201,211–215] The invention of scanning TEM (SETM) based EELS with extremely high resolution (> 0.1eV) makes possible the characterization of the near-field energy distribution of LSPR of individual nanoparticles. Specifically, EELS spectra can reveal the intensity and frequency of LSPR at the specific interested positions on a SETM mode image, while simultaneously conduct an elemental mapping either a dark or bright field so as to correlate the structure, chemical composition to the intrinsic LSPR properties on the nanoscale.[212,213,216–221]

In the current research work, by using our proposed LASiS-GRR technique, we successfully embedded Ag and Au into the photoactive material ZnO and TiO_2 with large band gap and therefore weak light absorbance. The detailed reactions between Zn/Ti and $AgNO_3$/$HAuCl_4$ can be written as follows:

$$Zn/Ti + 2Ag^{+} = 2Ag + Zn^{2+}/Ti^{2+} \qquad \text{Eqn. 6.1}$$

$$3Zn/Ti + 2Au^{3+} = 2Au + 3Zn^{2+}/Ti^{2+} \qquad \text{Eqn. 6.2}$$

Both reactions have negative Gibbs-free energies hence can occur automatically. Therefore it is of great interest to see what kind of complex nanostructure can be created within the extreme thermodynamic conditions endowed by the laser plasma during our proposed LASiS-ORR technique.

6.1.2 Results

6.1.2.1 Synthesis of Ag/Au@ZnO/TiO_2 via LASiS/LASiS-GRR

The direct products from LASiS on Zn and Ti in water were determined as a ZnO NPs as well as a mixed state of TiO_x NPs respectively. To be specific, Fig. 6.1.a exhibits the TEM images of produced ZnO NPs with irregular shapes and some degree of aggregation. The chemical composition (oxidation state) is determined by the SAED pattern in the inset along with the HRTEM images in Fig. 6.1.b that reveals the ZnO (100) lattice plane with the d-spacing of 0.281 nm. On the other hand, two types of nanostructures are formed in the products of LASiS on Ti, namely, a large portion of amorphous dendritic structure along with randomly embedded spherical NPs, which are later determined as Srilankite type TiO_2 through the identification of its d-spacing in SAED and HRTEM (reveals the (111) and (110) facets).

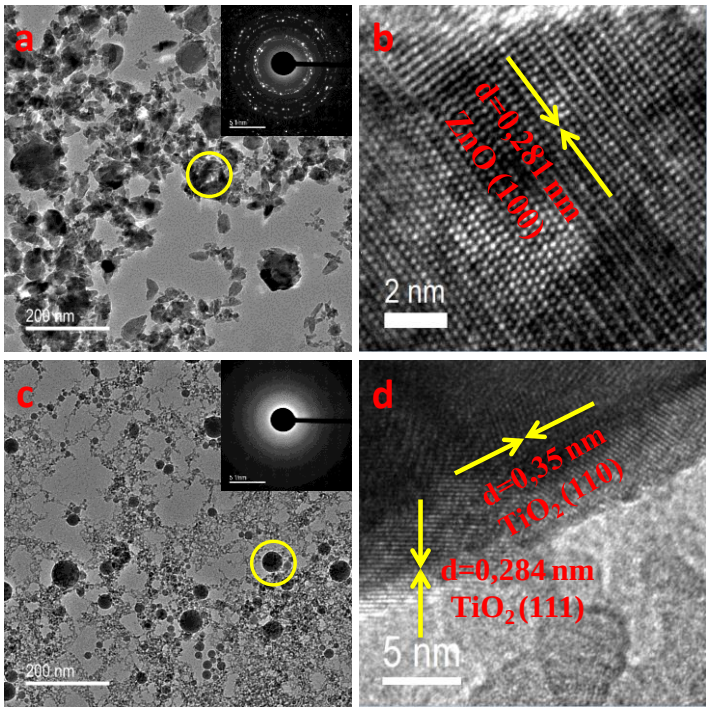


Fig. 6.1 LASiS on Zn (**a** and **b**) and Ti (**c** and **d**) in water (1064 nm laser for 10 min). **b**, **d**, HRTEM images for the circled position in **a** and **b** respectively indicating the products are ZnO and Srilankite type TiO_2 (only for the spherical part). The insets show the SAED patterns.

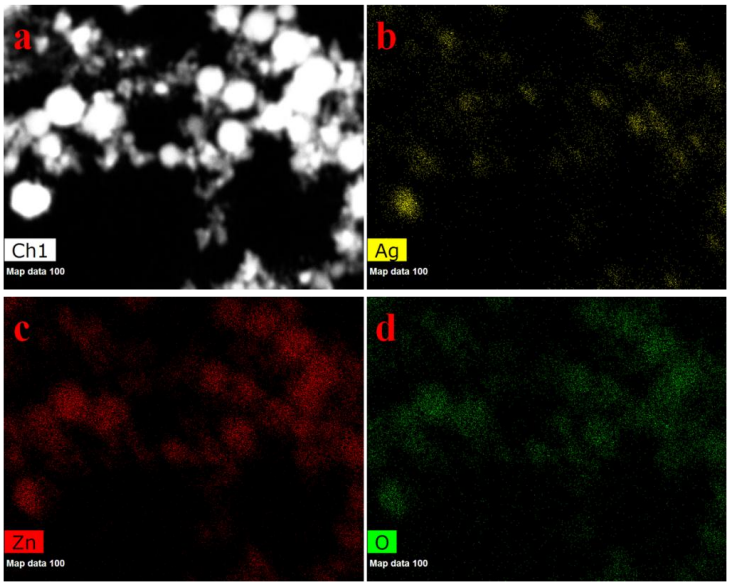


Fig. 6.2 **a**, HAADF image of the sample synthesized via LASiS on Zn in $AgNO_3$; **b, c, d,** the corresponding Ag, Zn and O EDX mappings.

It needs to be mentioned here that after acid wash using 10mM HNO_3 for 3 hrs, the amorphous TiO_x are completely gone, leaving only the spherical Srilankite type TiO_2, as will be confirmed latter. This acid-tolerant property provides them the great potential to be applied as sensor materials or catalysts in some harsh environment conditions.

By carrying out LASiS-GRR of Zn and Ti in $AgNO_3$ solution, we successfully embedded the Ag NPs into the ZnO and TiO_x matrices respectively, as demonstrated by Fig. 6.2 and Fig. 6.3.a-c showing EDX elemental mappings. It needs to be pointed out that for the Zn target, Ag is uniformly embedded inside the ZnO matrices, as dictated by Fig. 6.2.b; for LASiS on Ti, as mentioned earlier, it forms a mixture of amorphous TiO_x and spherical srilankite type TiO_2 NCs. For LASiS-GRR on Ti with $AgNO_3$, we performed acid wash right after, and which ends up forming core-shell Ag/srilankite TiO_2 NPs. These srilankite TiO_2 are thus confirmed to be anti-corrosive from acid, which provides the possibility to be utilized in harsh conditions. The embedding of Ag NPs is also confirmed by the XRD profile shown in Fig. 6.4, where ZnO are also found to have much higher crystallinity than TiO_x.

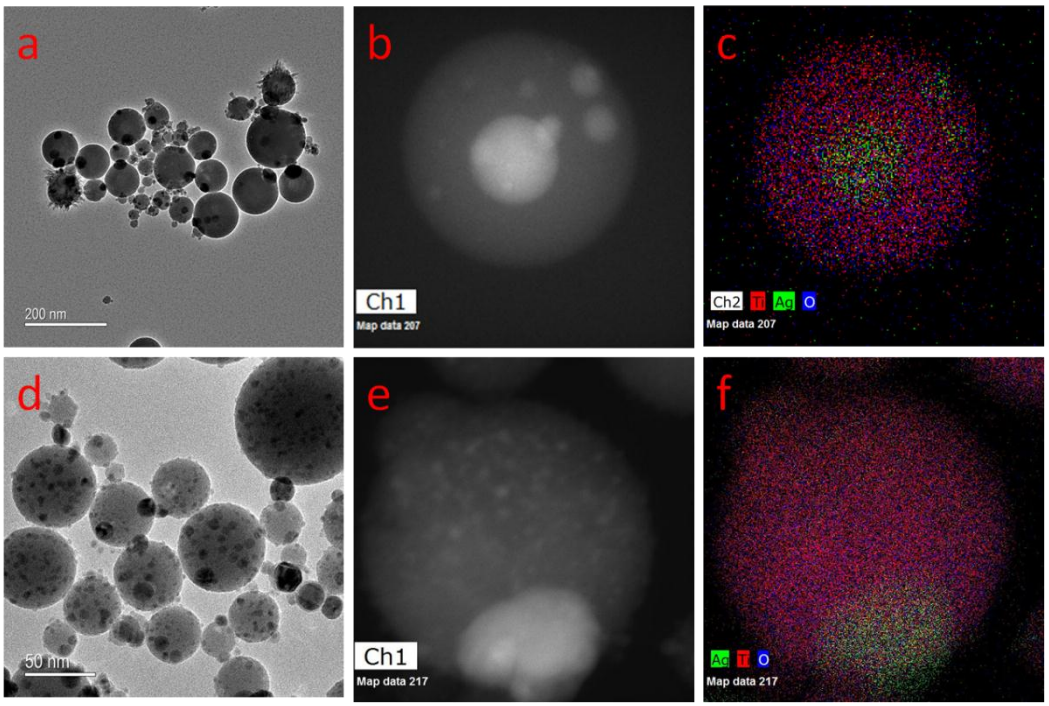


Fig. 6.3 **a** HAADF image of the sample synthesized via LASiS on Ti in $AgNO_3$ after HNO_3 wash; **b, c** Enlarged HAADF image and EDX mapping of **a**; **d** Sample **a** after RI**; e, f** Enlarged HAADF image and EDX mapping of **d**.

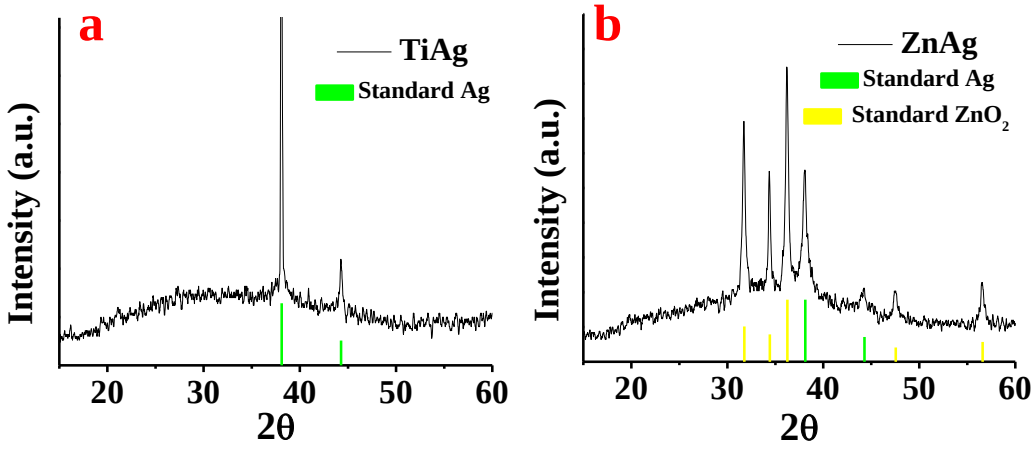


Fig. 6.4 XRD profile for the synthesized Ag/TiO_2 (**a**) and Ag/ZnO (**b**) NCs.

Also, similar to the chapter 3, we also carried out re-irradiation (RI) treatment to the synthesized Ag/TiO_2 using 532 nm laser. Such an operation was found to reshape already formed irregular shaped CoO_x NPs into spherical ones with enlarged sizes. Here, however, RI induces the formation of small clusters inside the big spherical srilankite TiO_2 NPs; meanwhile, a portion of embedded Ag NPs move outwards from the edge and become half-embedded, as revealed by Fig. 6.3 e-g.

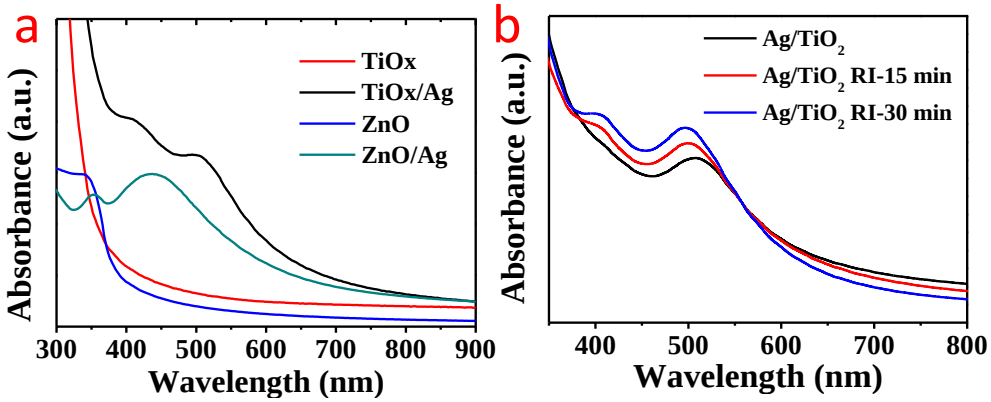


Fig. 6.5 UV-Vis absorbance of **a**, TiO_x/ZnO NPs with/without embedded Ag; **b**, acid washed Ag/TiO_x NCs after re-irradiated (RI) for different time scales.

6.1.2.2 Characterization of LSPR properties

Ag and Au are well-known for their localized surface Plasmon resonance (LSPR) properties, which, in our current research work, were characterized via UV-Vis absorbance and electron energy loss spectroscopy (EELS). For Ag/ZnO NCs, two plasmonic peaks form with the major one located at ~440 nm and minor one centered at 350 nm; while for the Ag/TiO_x, the two plasmonic peaks red-shift to the ~500 nm and 410 nm respectively, as can be seen in Fig. 6.5.a. The dissimilarity is due to the different Ag-metal oxide interactions as well as the variation in sizes, which dramatically impact the electron resonance frequency and hence affect the LSPR position. Fig. 6.5.b reveals the RI effect on the acid washed Ag/TiO_x NCs. It is first noted that right after acid wash, the minor peak at 400 nm is gone, which corresponds to the scatted Ag embedded in the amorphous TiO_x. However, the core-shell Ag/TiO_2

structure protects the Ag inside from washing away by acid, therefore remains the major LSPR peak. After RI for 15 and 30 min, the major peak slightly blue-shifts to the smaller wavelength (~490 nm), while the minor peak at 400 nm starts showing up again, which, we assume this is possibly ascribed to the Ag that gradually sliding out from the TiO_2 shell—a surface re-structuring process exerted by laser-induced thermal and photonic energy during RI.

For further characterizations, Appendix B presents a detailed EELS analysis for the plasnmonic peaks at different positions of the embedded Ag in the aforementioned NC systems are presented in Appendix B embedded

Finally, we carried out LASiS-GRR on Ti inside the $HAuCl_4$ solution followed by same acid washing procedure, which ends up forming separate Au NPs and srilankite type TiO_2, with the LSPR peak located at ~550 nm, as dictated by Fig. 6.7.a and b. It can be speculated that the separation of the two nanostructures is probably due to their different lattice structure and large surface binding energy, which will be investigated for verification in our future research work.

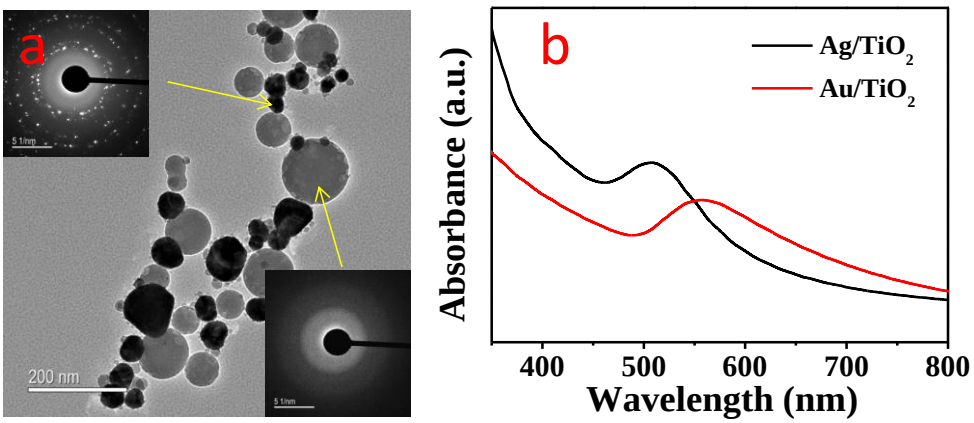


Fig. 6.6 **a**, TEM image of Au/TiO_2 NCs synthesized via LASiS-GRR, the insets at top and bottom exhibit the SAED of Au and TiO_2 respectively; **b**, Comparison of UV-Vis spectra of Ag/TiO_2 and Au/TiO_2.

It should be noted here that rational design and implementation of the aforementioned metal/metal oxide NC systems as suitable photocatalytic materials in future shall require systematic analysis and characterizations of their band gap and

edge potential properties (detailed band gap/edge calculations presented on Appendix A). Such detailed characterizations become necessary to ensure that these designer nanomaterials can efficiently absorb in the visible rage of the solar spectra while enabling the bandwidth to straddle between the redox potentials for water oxidation and proton reduction as well as promoting efficient charge transport properties.

6.2 Applications of LASiS/LASiS-GRR technique for the synthesis of other intermetallic NMs

6.2.1 LASiS on other metals

We have also carried out LASiS on metals other than Co, and found similar properties for the products when comparing with LASiS on Co. Fig. 6.7 illustrate the TEM images of the products from LASiS on Cu in water using 1064 nm laser. The direct products include two types of nanostructures, namely, spherical NPs along with nanorods, which are determined as Cu_2O and CuO respectively from the HRTEM images shown in c and d. However, both nanostructures are in their meta-stable phases, after three days of aging, both transform into larger CuO NRs with smaller length to diameter ratios (Fig. 6.7.b). Besides, we have also found out that LASiS on Ni with N_2 blow produces single crystal $Ni(OH)_2$, while LASiS on Mn in alkaline conditions leads to the formation of multiphase MnO_x NPs.

Furthermore, we have also tried LASiS on alloyed target, such as stainless steel (SS), in which case a mixture of metal oxides are formed with uniform distribution. Specifically, the products involve majority of γ-Fe_2O_3 along with small amount of CrO and NiO NPs, as shown in Fig. 6.8. In future, we will try to carry LASiS on more various types of targets, including inorganic elements such as C or Si, post transition metals, or even Lanthanoids and Actinoids.

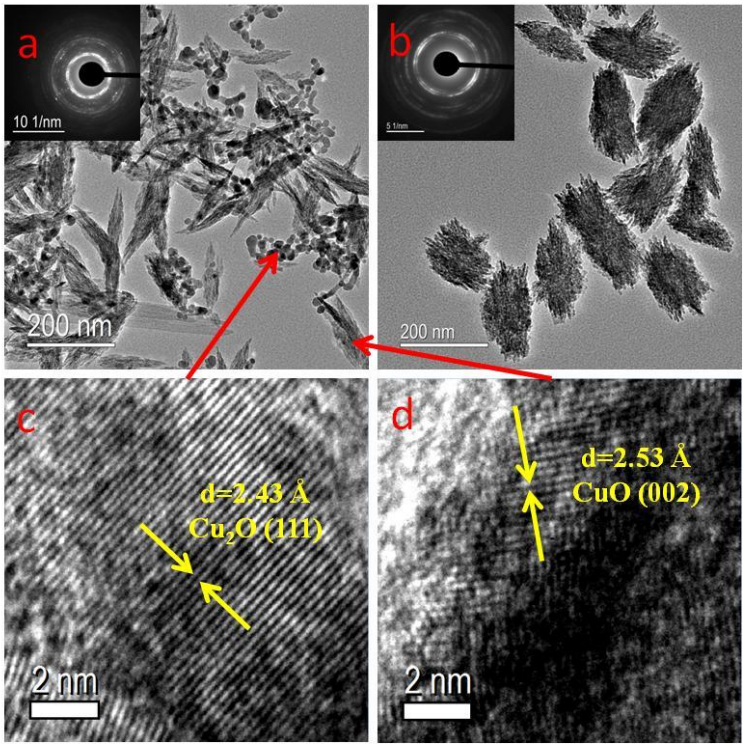


Fig. 6.7 TEM images of LASiS on Cu in water: **a**, right after LASiS; **b**, after 3 days aging; **c, d,** the corresponding HRTEM images for the spherical NPs and NRs in **a**.

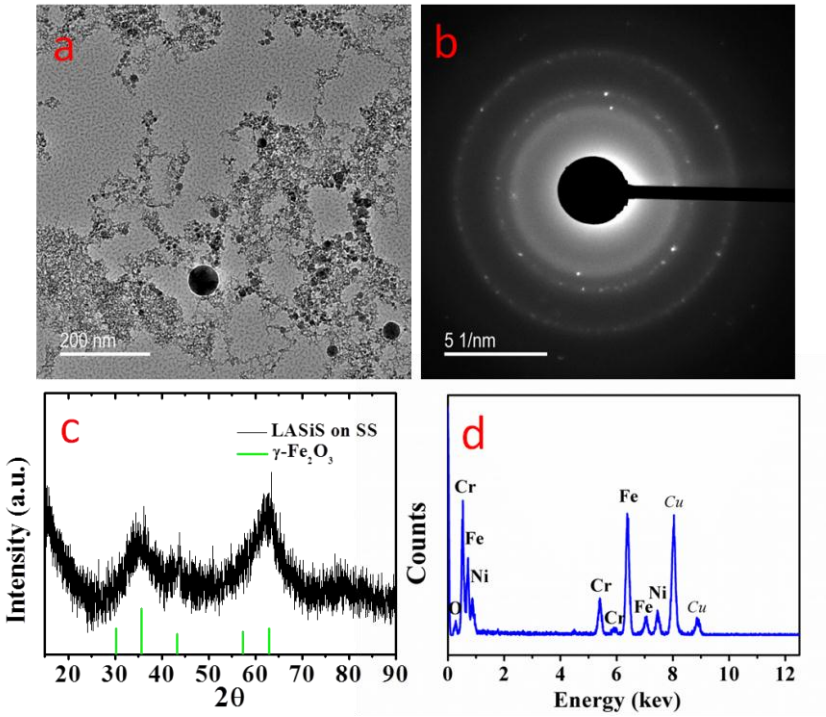


Fig. 6.8 LASiS on stainless steel in water: **a**, TEM images; **b**, SAED pattern; **c**, XRD data; **d**, EDX pattern.

6.2.2 LASiS/LASiS-GRR in organic solvents

We have also applied different solvents other than water, including toluene, ethanol, DFM, etc. Fig. 6.9.a, b reveal the TEM images along with the corresponding SAED pattern for the products of LASiS on Zn in toluene, where ZnO NPs are formed which however, covered by a carbon shell. By carrying out LASiS-GRR in organic solution, we first transferred $HAuCl_4$ from water phase into toluene using a phase transfer agent dodecylamine, followed by the same procedure as LASiS-GRR in water. The products are shown in Fig. 6.9.c, d, where Au NPs with medium agglomeration are found to uniformly distribute in the mixture of ZnO/carbon junction. Future studies include UV-Vis spectrum as well as EELS analysis for characterizing its SPR properties.

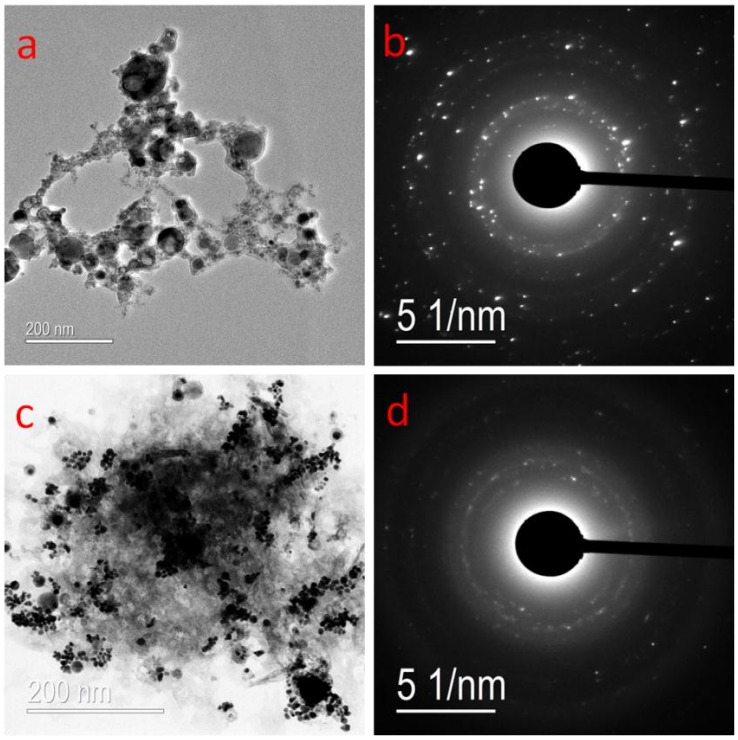


Fig. 6.9 TEM and the corresponding SAED patterns of: **a, b,** LASiS on Zn in toluene; **c, d,** LASiS on Zn in toluene with $HAuO_4$.

6.2.3 Other binary noble metal-transition metal nanoalloys

LASiS-GRR also works for other noble metal-transition metal NA systems. Two examples are shown below, namely, LASiS-GRR on Ni with K_2PtCl_4 (Fig. 6.10) and LASiS-GRR on Co with Na_2PdCl_4 (Fig. 6.11). The former forms pure PtNi NAs, however, showing less ORR activities than PtCo NAs; although the latter also forms PdCo NAs, but the atomic Co ratio is only 5%, much lower than the PtCo system, which is probably due to dissimilarity of the Pt and Co crystalline lattice structures.

6.2.4 Ternary alloys

Fig. 6.12 reveals the EDX mappings of the PtPdCo ternary alloys, which were prepared by LASiS-GRR on Co with existence of both K_2PtCl_4 and Na_2PdCl_4 precursors, though Co atomic ratio is still low here (less than 10%). In such cases, Pt^{2+} and Pd^{2+} will go through competing GRR reactions with the seeding Co generated from LASiS.

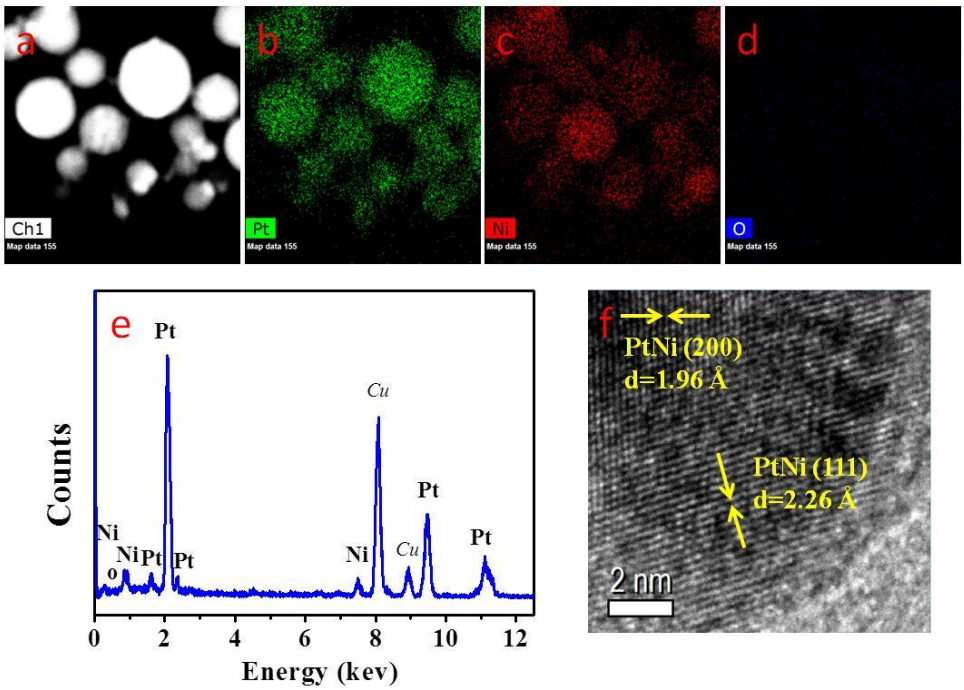


Fig. 6.10 LASiS-GRR on Ni with K_2PtCl_4: **a-d,** EDX mapping; **e,** EDX spectrum; **f,** HRTEM.

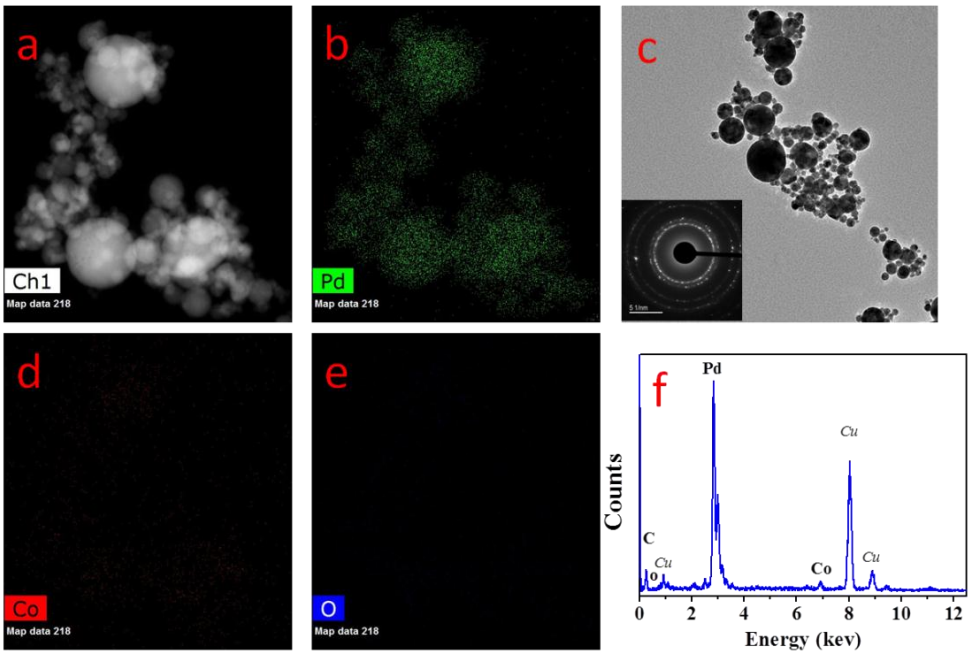


Fig. 6.11 LASiS-GRR on Co with Na_2PdCl_4: **a, b, d, e,** EDX mapping; **c,** TEM image; **f,** EDX spectrum.

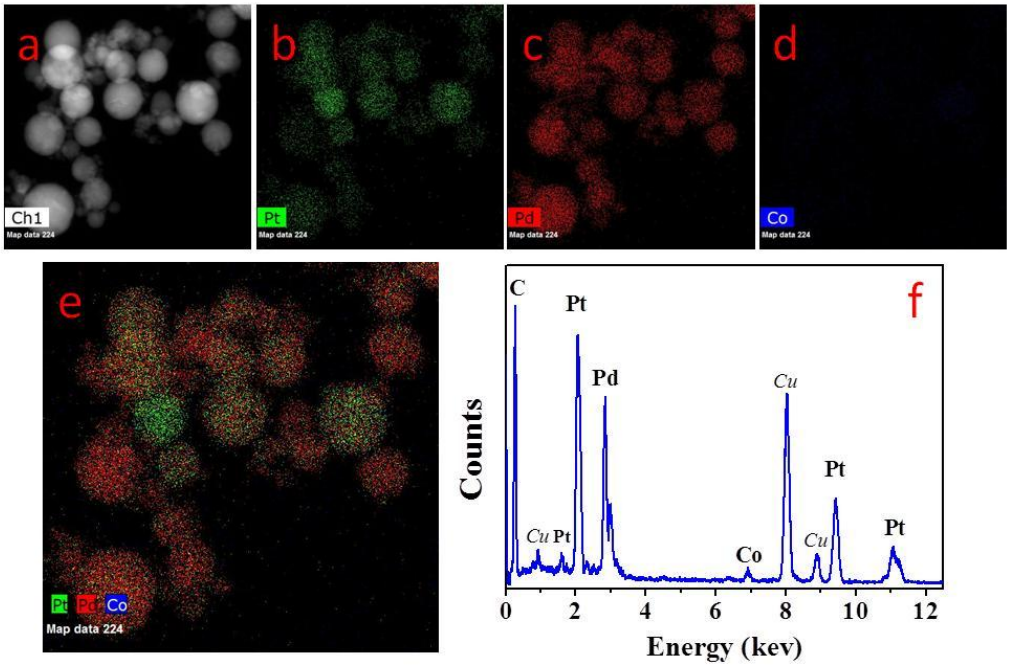


Fig. 6.12 EDX analysis of LASiS-GRR on Co with K_2PtCl_4 and Na_2PdCl_4.

6.3 Post treatment after LASiS-GRR

Post treatment such as thermal annealing plays a critical role in modifying the crystalline structures of already formed nanostructures. For PtCo alloys, it is reported that Pt_3Co ordered alloy can be formed after TA over 700 C^o,[79,89,222] which in turn benefits its catalytic properties such as ORR. However, due to the intrinsic low Co ratio, the supperlattice structure is very week or even invisible. Here, we thermal annealed our PtCo NA synthesized at pH11 condition (with 39% of Co atomic ratio) at 700 C^o for 2 hours in H_2/N_2 (10% H_2) environment. The products exhibit a core-shell structure with pure Pt as the shell and ordered Pt_3Co supperlattice as the core, as indicated by Fig. 6.13.a, b for the HRTEM image and XRD spectrum respectively. However, after TA, our NAs form extremely large aggregations, which is due to the fact that we did not use any kind of surfactant during LASiS-GRR process. Such severe aggregates dramatically reduce the electrochemical active surface areas of our NPs and therefore lower the ORR activities. Future work will focus on prohibiting the severe aggregation during TA process for those NPs so as to improve both mass and specific catalytic activities for the ORR process.

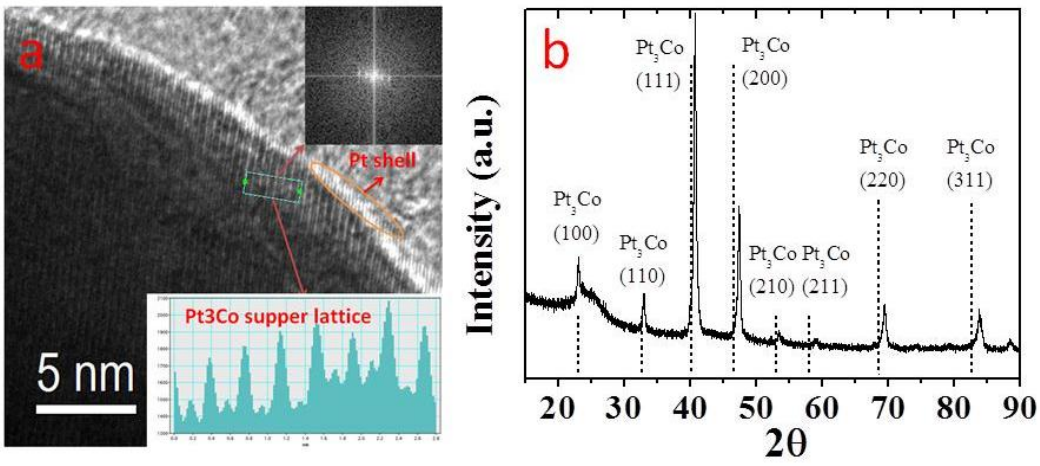


Fig. 6.13 PtCo NA (synthesized at pH11) after TA at 700 C^o for 2h: **a**, HRTEM showing a core-shell structure with a very thin pure Pt shell and a Pt_3Co superlattice core; **b**, the corresponding XRD pattern.

6.4 Summary

LASiS-GRR on Zn and Ti in $AgNO_3$ or $HAuCl_4$ solutions were carried out in our in-house designed multifunctional LASiS setup. The galvanic replacement reaction within the laser Plasma successfully embedded the plasmonic Ag into the ZnO or TiO_x matrices, with the majority Ag covered by spherical srilankite type TiO_2 NPs that are anti-corrosive in acid. Such core-shell structures exhibit localized surface Plasmon resonance at ~500 nm, as attributed by Plasmon-medium interaction. After re-irradiation, embedded Ag starts to move outwards and exhibiting a minor plasmonic peak at ~400 nm. In addition, we also exhibit the preliminary results for LASiS on other metal systems and in organic solvent, LASiS-GRR for production of other binary and ternary NAs, along with post treatment such as thermal annealing for the produced NAs from LASiS-GRR.

Chapter 7 Summary

A new nanoscale synthesis technique is proposed in this project which combines laser ablation synthesis in solution in tandem with galvanic replacement reaction (LASiS-GRR) as a facile and green synthesis technique for fabricating nanomaterials with various applications. Specifically, by using LASiS-GRR we synthesized and characterized various types nanomaterials including cobalt oxides (NPs and NRs) and hydroxides, nanocomposites of $PtCo/CoO_x$ as bifunctional ORR/OER catalysts, PtM nanoalloys (M stands for Co, Ni, Mn, etc.) as ORR catalysts, SPR enhanced NCs of Ag/Au embedded ZnO/TiO_2 as photocatalysts, along with other complex nanostructures or even ternary metal alloys. This is made possible by the specific thermodynamic conditions provided with LASiS where GRR takes places, which in turn result in formation of NPs with plasma-induced surface charges that prevent them from aggregation. As a consequence, unwanted chemicals such as surfactants that are harmful to catalysts are not needed in such an elegant synthesis technique, thereby remarkably improve their catalytic performances.

In the first project, we investigate the effects of laser parameters (wavelength, laser fluence) and solution phase properties (O_2 content, pH) on the size, shape, structure and composition of the resultant nanostructured materials produced from LASiS on bulk Co targets in aqueous solutions. Our results indicate that the chemical pathway during LASiS on Co in water leads to the formation of metastable intermediates such as CoO and single crystal β-$Co(OH)_2$ NPs in the presence and absence of solution-phase O_2 respectively. Both intermediates transform into Co_3O_4 NPs as the final products through oxidation and/or thermal decomposition in solution phase. In addition, we establish the role of the physics behind the different ablation mechanisms in tailoring the size and morphology of the final Co_3O_4 NPs. For both 1064 and 532 nm lasers, vaporization and normal boiling mechanism during LASiS at low laser fluence (<20 mJ/cm^2) dictates the formation of sparsely agglomerated NPs of bimodal size distribution. In contrast, the more efficient and explosive boiling

presides as the dominant mechanism over the former two during LASiS at higher laser fluences that results in mono-modal size distributions of spherical shaped primary NPs in the agglomerates formed. Furthermore, we demonstrate that the high absorbance of 532 nm laser by solution-phase colloidal NPs promotes their re-ablation into spherical structures with increased average sizes. This is evident from the higher mean particle sizes (~13–22 nm) for NPs produced by 532 nm LASiS as compared to the ones synthesized with 1064 nm LASiS (~10–14 nm). To this end, we conclude that although the 532 nm laser indicates higher energy penetration through the aqueous solutions, its self-absorption by colloidal NPs renders it less productive than ablation with 1064 nm laser over extended period of time. Finally, LASiS on Co in alkaline aqueous solutions (pH≥13) and low laser fluence conditions (<5 mJ/cm^2) produce Co_3O_4 nanorods (NRs) that exhibit enhanced LSPR properties in the visible range of ~400-410 nm wavelength. The aforementioned understanding of the chemical physics of laser ablation for different laser and solution phase parameters is fundamental to our critical design of LASiS and the following LASiS-GRR technique for tailored synthesis of a wide variety metal/metal oxide nanostructured materials in future.

In the second project, we presented tandem LASiS-GRR to manufacture complex PtCo/CoO_x nanocomposites (NCs) with outstanding ORR and OER catalytic activities. The transformative concept here is the ability to synthesize such complex heteronanostructures in one step without the need for any harsh chemical reagents and/or, surfactants. This is made possible by the non-equilibrium thermodynamic conditions emerging from extreme physicochemical conditions of high energy LASiS operating in tandem with chemical reduction processes (GRR in this case). The synthesized PtCo NCs exhibited excellent yet, stable catalytic activities for both oxygen reduction reactions (ORR) and oxygen evolution reactions (OER) in alkaline media. Specifically, we reported a combined overpotential of 756 mV vs. RHE for the PtCo-3 NC (33.3 molar %, 62.3 wt. %), which is the highest value ever reported using carbon black as the supporting material. This excellent bifunctional activity is

attributed to the structural and electronic properties of PtCo nanoalloy that promote oxygen adsorption, as well as to the sponge-shaped CoO_x matrices in which the PtCo NPs are embedded that bring about the synergic "spillover" effects to facilitate both ORR and OER activities. Added to this, the CoO_x matrix also prevents the PtCo NPs from aggregation and dissolution in alkaline electrolytes. Encouraged by the current results, we have work in progress to extend the aforementioned clean yet, facile synthesis routes for the future design of various complex intermetallic NCs in a rapid and cost-effective fashion.

Thereafter, by applying a acid wash process, we synthesized PtCo NAs as excellent ORR catalysts with controllable size, atomic compositions and alloying degrees. Specifically, the PtCo NAs with crystallite sizes of ~4.70 nm and ~58 % degree of alloying (~22 % reduction in Pt atomic content) exhibit superior ORR activities in acid electrolyte solutions as compared to the corresponding activities for standard Pt/C catalysts. Such activities are attributed to the unique capabilities of tandem LASiS-GRR to synthesize the aforementioned NAs with controlled sizes and uniform elemental distributions. Specifically, detailed structural characterizations of the NAs from EDX and EELS ratio mappings indicate a thin layer of Pt-rich shell on an alloyed core with relatively uniform Pt:Co ratio. The rational tuning of such structure-property relations are achieved by systematically controlling the initial Pt salt concentrations, ablation times and solution phase pH conditions during the LASiS-GRR technique. The transformative concept here is the ability of seeding NPs generated by the rate limiting step of LASiS to drive the simple redox chemistry in the rate controlling step of GRR that allows directed tailoring of sizes, structures and alloying/compositions in the final NCs/NAs. When operated in tandem, reaction pathways emerging from high-energy liquid-confined plasma can be regulated to create heteronanostructures with metastable structures and phases without the use of any external chemical agents/surfactants. Finally, simulation of the rate kinetics of the LASiS-GRR process confirms part of our proposed mechanism, meanwhile provides the estimation for the injection rate of Pt salt in a continuous supply system towards

mass production. Finally, DFT calculation theoretically confirmed our synthesized catalysts in term of high ORR activity.

Finally, LASiS-GRR on Zn and Ti in $AgNO_3$ or $HAuCl_4$ solutions were carried out in our in-house designed multifunctional LASiS setup. Our preliminary results indicate that the galvanic replacement reaction within the laser Plasma successfully embedded the plasmonic Ag into the ZnO or TiO_x matrices, with the majority Ag covered by spherical srilankite type TiO_2 NPs that are anti-corrosive in acid. Such core-shell structures exhibit localized surface Plasmon resonance at ~500 nm, as attributed by Plasmon-medium interaction. After re-irradiation, embedded Ag starts to move outwards and exhibiting a minor plasmonic peak at ~400 nm. In addition, we also exhibit the preliminary results for LASiS on other metal systems and in organic solvent, LASiS-GRR for production of other binary and ternary NAs, along with post treatment such as thermal annealing for the produced NAs from LASiS-GRR.

References

1. Liao, L. *et al.* Efficient solar water-splitting using a nanocrystalline CoO photocatalyst. *Nat. Nanotechnol.* **9,** 69–73 (2013).
2. Langille, M. R., Personick, M. L. & Mirkin, C. A. Plasmon-Mediated Syntheses of Metallic Nanostructures. *Angew. Chemie Int. Ed.* **52,** 13910–13940 (2013).
3. Wu, Y., Wang, D. & Li, Y. Nanocrystals from solutions: catalysts. *Chem. Soc. Rev.* **43,** 2112–2124 (2014).
4. Ghosh Chaudhuri, R. & Paria, S. Core/shell nanoparticles: Classes, properties, synthesis mechanisms, characterization, and applications. *Chem. Rev.* **112,** 2373–2433 (2012).
5. Blakemore, J. D., Gray, H. B., Winkler, J. R. & Mu, A. M. Co 3 O 4 Nanoparticle Water-Oxidation Catalysts Made by Pulsed-Laser Ablation in Liquids. *Catalysis* **3,** 2497–2500 (2013).
6. Wang, L. *et al.* Nanorod-assembled Co3O4 hexapods with enhanced electrochemical performance for lithium-ion batteries. *J. Mater. Chem.* **22,** 23541 (2012).
7. Yuan, C. *et al.* Lysine-assisted hydrothermal synthesis of urchin-like ordered arrays of mesoporous Co(OH)2 nanowires and their application in electrochemical capacitors. *J. Mater. Chem.* **20,** 10809 (2010).
8. Nguyen, H. & El-Safty, S. a. Meso- and macroporous Co3O4 nanorods for effective VOC gas sensors. *J. Phys. Chem. C* **115,** 8466–8474 (2011).
9. Shinde, V. R., Mahadik, S. B., Gujar, T. P. & Lokhande, C. D. Supercapacitive cobalt oxide (Co3O4) thin films by spray pyrolysis. *Appl. Surf. Sci.* **252,** 7487–7492 (2006).
10. Metin, Ö.¨, Mazumder, V., Özkar, S. & Sun, S. Monodisperse nickel nanoparticles and their catalysis in hydrolytic dehydrogenation of ammonia borane. *J. Am. Chem. Soc.* **132,** 1468–1469 (2010).
11. Thorum, M. Oxygen reduction electrocatalysis. *Dissertation* (2011). at <https://www.ideals.illinois.edu/handle/2142/24318>
12. Song, C. & Zhang, J. Electrocatalytic oxygen reduction reaction. *PEM Fuel Cell Electrocatal. Catal. Layers Fundam. Appl.* 89–134 (2008). doi:10.1007/978-1-84800-936-3_2
13. Rezvani, M. R. & Shokuhfar, a. Synthesis and characterization of nano structured Cu-Al-Mn shape memory alloy by mechanical alloying. *Mater. Sci. Eng. A* **532,** 282–286 (2012).
14. Ataie, a., Kazemzadeh, H., Nikkhah-Moshaie, R. & Ahmed, F. M. Synthesis of nano-crystalline magnetite by SHS route. *IEEE Trans. Magn.* **45,** 2496–2498 (2009).
15. Xia, D. *et al.* Synthesis of ordered intermetallic PtBi2 nanoparticles for methanol-tolerant catalyst in oxygen electroreduction. *Chem. Mater.* **18,** 5746–5749 (2006).
16. Thiagarajan, S. J., Wang, W. & Yang, R. Chapter x nanocomposites as high efficiency thermoelectric materials. 1–47

17. Liao, M. *et al.* Co3O4 Nanoparticles as Robust Water Oxidation Catalysts Towards Remarkably Enhanced Photostability of a Ta3N5 Photoanode. *Adv. Funct. Mater.* **22,** 3066–3074 (2012).
18. Thangavelu, K., Parameswari, K., Kuppusamy, K. & Haldorai, Y. A simple and facile method to synthesize Co3O4 nanoparticles from metal benzoate dihydrazinate complex as a precursor. *Mater. Lett.* **65,** 1482–1484 (2011).
19. Ke, X. *et al.* Molten salt synthesis of single-crystal Co3O4 nanorods. *Mater. Lett.* **61,** 3901–3903 (2007).
20. Thota, S. & Kumar, J. Sol–gel synthesis and anomalous magnetic behaviour of NiO nanoparticles. *J. Phys. Chem. Solids* **68,** 1951–1964 (2007).
21. Hong, J. W. *et al.* Controlled synthesis of Pd-Pt alloy hollow nanostructures with enhanced catalytic activities for oxygen reduction. *ACS Nano* **6,** 2410–2419 (2012).
22. Lou, X. W., Deng, D., Lee, J. Y., Feng, J. & Archer, L. A. Self-Supported Formation of Needlelike Co3O4 Nanotubes and Their Application as Lithium-Ion Battery Electrodes. *Adv. Mater.* **20,** 258–262 (2008).
23. Mazumder, V., Chi, M., More, K. L. & Sun, S. Synthesis and Characterization of Multimetallic Pd/Au and Pd/Au/FePt Core/Shell Nanoparticles. *Angew. Chemie Int. Ed.* **49,** 9368–9372 (2010).
24. Le, H. A. *et al.* Chemical Vapor Synthesis and Characterization of Manganese Oxides. *Chem. Vap. Depos.* **17,** 228–234 (2011).
25. Kang, Y. S., Risbud, S., Rabolt, J. F. & Stroeve, P. Synthesis and Characterization of Nanometer-Size Fe_3O_4 and γ-Fe_2O_3 Particles. *Chem. Mater.* **8,** 2209–2211 (1996).
26. Wang, Y., Ren, J., Deng, K., Gui, L. & Tang, Y. Preparation of Tractable Platinum, Rhodium, and Ruthenium Nanoclusters with Small Particle Size in Organic Media. *Chem. Mater.* **12,** 1622–1627 (2000).
27. Zhang, Y. *et al.* Near-monodisperse Ni-Cu bimetallic nanocrystals of variable composition: Controlled synthesis and catalytic activity for H2 generation. *J. Phys. Chem. C* **112,** 12092–12095 (2008).
28. Leonard, B. M., Zhou, Q., Wu, D. & DiSalvo, F. J. Facile Synthesis of PtNi Intermetallic Nanoparticles: Influence of Reducing Agent and Precursors on Electrocatalytic Activity. *Chem. Mater.* **23,** 1136–1146 (2011).
29. Zhang, J., Yang, H., Fang, J. & Zou, S. Synthesis and Oxygen Reduction Activity of Shape-Controlled Pt_3Ni Nanopolyhedra. *Nano Lett.* **10,** 638–644 (2010).
30. Wiechen, M., Zaharieva, I., Dau, H. & Kurz, P. Layered manganese oxides for water-oxidation: alkaline earth cations influence catalytic activity in a photosystem II-like fashion. *Chem. Sci.* **3,** 2330 (2012).
31. Li, X. *et al.* Synthesis of Mn3O4 nanoparticles and their catalytic applications in hydrocarbon oxidation. *Powder Technol.* **190,** 324–326 (2009).
32. Armbrüster, M., Wowsnick, G., Friedrich, M., Heggen, M. & Cardoso-Gil, R. Synthesis and catalytic properties of nanoparticulate intermetallic Ga-Pd

compounds. *J. Am. Chem. Soc.* **133,** 9112–8 (2011).
33. Zheng, L. *et al.* Capping agent free synthesis of PtSn bimetallic nanoparticles with enhanced electrocatalytic activity and lifetime over methanol oxidation. *Catal. Commun.* **9,** 624–629 (2008).
34. Barcikowski, S. & Compagnini, G. Advanced nanoparticle generation and excitation by lasers in liquids. *Phys. Chem. Chem. Phys.* **15,** 3022–6 (2013).
35. Amendola, V. & Meneghetti, M. What controls the composition and the structure of nanomaterials generated by laser ablation in liquid solution? *Phys. Chem. Chem. Phys.* **15,** 3027–3046 (2013).
36. Amans, D. *et al.* Synthesis of oxide nanoparticles by pulsed laser ablation in liquids containing a complexing molecule: Impact on size distributions and prepared phases. *J. Phys. Chem. C* **115,** 5131–5139 (2011).
37. Cristoforetti, G., Pitzalis, E., Spiniello, R., Ishak, R. & Muniz-Miranda, M. Production of Palladium Nanoparticles by Pulsed Laser Ablation in Water and Their Characterization. *J. Phys. Chem. C* **115,** 5073–5083 (2011).
38. Wang, C. X., Liu, P., Cui, H. & Yang, G. W. Nucleation and growth kinetics of nanocrystals formed upon pulsed-laser ablation in liquid. *Appl. Phys. Lett.* **87,** 201913 (2005).
39. Tsuji, T., Hamagami, T., Kawamura, T., Yamaki, J. & Tsuji, M. Laser ablation of cobalt and cobalt oxides in liquids: influence of solvent on composition of prepared nanoparticles. *Appl. Surf. Sci.* **243,** 214–219 (2005).
40. Amendola, V. & Meneghetti, M. Laser ablation synthesis in solution and size manipulation of noble metal nanoparticles. *Phys. Chem. Chem. Phys.* **11,** 3805 (2009).
41. Yan, Z., Bao, R., Huang, Y. & Chrisey, D. B. Hollow particles formed on laser-induced bubbles by excimer laser ablation of Al in liquid. *J. Phys. Chem. C* **114,** 11370–11374 (2010).
42. Itina, T. E. On Nanoparticle Formation by Laser Ablation in Liquids. *J. Phys. Chem. C* **115,** 5044–5048 (2011).
43. Amendola, V., Riello, P. & Meneghetti, M. Magnetic nanoparticles of iron carbide, iron oxide, iron@iron oxide, and metal iron synthesized by laser ablation in organic solvents. *J. Phys. Chem. C* **115,** 5140–5146 (2011).
44. Kevin Hagedorn, Bing Liu, and A. M. 2013IntermtallicPtPb_NP_LASIS_JElectrochemSoc_Hagedorn-F106-10.pdf. *J. Electrochem. Soc.* **160,** F106–F110 (2013).
45. Hur, T. B., Phuoc, T. X. & Chyu, M. K. Synthesis of Mg-Al and Zn-Al-layered double hydroxide nanocrystals using laser ablation in water. *Opt. Lasers Eng.* **47,** 695–700 (2009).
46. Jiménez, E., Abderrafi, K., Abargues, R., Valdés, J. L. & Martínez-Pastor, J. P. Laser-ablation-induced synthesis of SiO2-capped noble metal nanoparticles in a single step. *Langmuir* **26,** 7458–7463 (2010).
47. Zeng, H. *et al.* Violet photoluminescence from shell layer of Zn/ZnO core-shell nanoparticles induced by laser ablation. *Appl. Phys. Lett.* **88,** 1–4 (2006).

48. Niu, K. Y., Yang, J., Kulinich, S. a., Sun, J. & Du, X. W. Hollow nanoparticles of metal oxides and sulfides: Fast preparation via laser ablation in liquid. *Langmuir* **26,** 16652–16657 (2010).
49. Bai, G. *et al.* Porous Co3O4 nanowires and nanorods: Highly active catalysts for the combustion of toluene. *Appl. Catal. A Gen.* **450,** 42–49 (2013).
50. Liu, P. *et al.* Room temperature synthesized rutile TiO(2) nanoparticles induced by laser ablation in liquid and their photocatalytic activity. *Nanotechnology* **20,** 285707 (2009).
51. Miotello, a. & Kelly, R. Laser-induced phase explosion: New physical problems when a condensed phase approaches the thermodynamic critical temperature. *Appl. Phys. A Mater. Sci. Process.* **69,** 67–73 (1999).
52. Park, K., Lee, D., Rai, a., Mukherjee, D. & Zachariah, M. R. Size-resolved kinetic measurements of aluminum nanoparticle oxidation with single particle mass spectrometry. *J. Phys. Chem. B* **109,** 7290–7299 (2005).
53. Wagener, P., Ibrahimkutty, S., Menzel, A., Plech, A. & Barcikowski, S. Dynamics of silver nanoparticle formation and agglomeration inside the cavitation bubble after pulsed laser ablation in liquid. *Phys. Chem. Chem. Phys.* **15,** 3068–3074 (2013).
54. Mortazavi, S. Z., Parvin, P., Reyhani, A., Golikand, A. N. & Mirershadi, S. Effect of laser wavelength at IR (1064 nm) and UV (193 nm) on the structural formation of palladium nanoparticles in deionized water. *J. Phys. Chem. C* **115,** 5049–5057 (2011).
55. Intartaglia, R. *et al.* Optical properties of femtosecond laser-synthesized silicon nanoparticles in deionized water. *J. Phys. Chem. C* **115,** 5102–5107 (2011).
56. Alrehaily, L. M., Joseph, J. M., Biesinger, M. C., Guzonas, D. a & Wren, J. C. Gamma-radiolysis-assisted cobalt oxide nanoparticle formation. *Phys. Chem. Chem. Phys.* **15,** 1014–24 (2013).
57. Compagnini, G. *et al.* Monitoring the formation of inorganic fullerene-like MoS \n 2 nanostructures by laser ablation in liquid environments. *Appl. Surf. Sci.* **258,** 5672–5676 (2012).
58. Blandin, P. *et al.* Femtosecond laser fragmentation from water-dispersed microcolloids: toward fast controllable growth of ultrapure Si-based nanomaterials for biological applications. *J. Mater. Chem. B* **1,** 2489–2495 (2013).
59. Singh, S. C. Effect of oxygen injection on the size and compositional evolution of ZnO/Zn(OH)2 nanocomposite synthesized by pulsed laser ablation in distilled water. *J. Nanoparticle Res.* **13,** 4143–4152 (2011).
60. Hu, S., Melton, C. & Mukherjee, D. A facile route for the synthesis of nanostructured oxides and hydroxides of cobalt using laser ablation synthesis in solution (LASIS). *Phys. Chem. Chem. Phys.* **16,** 24034–24044 (2014).
61. Oh, M. H. *et al.* Galvanic Replacement Reactions in Metal Oxide Nanocrystals. *Science (80-.).* **340,** 964–968 (2013).
62. Sarkar, a & Manthiram, a. Synthesis of Pt @ Cu Core-Shell Nanoparticles

by Galvanic Displacement of Cu by Pt 4 + Ions and Their Application as Electrocatalysts for Oxygen Reduction Reaction in Fuel Cells. *Society* 4725–4732 (2010). doi:10.1021/jp908933r

63. Teng, X. *et al.* Formation of Pd/Au nanostructures from Pd nanowires via galvanic replacement reaction. *J. Am. Chem. Soc.* **130,** 1093–1101 (2008).
64. Sun, Y. & Wang, Y. Monitoring of galvanic replacement reaction between silver nanowires and HAuCl4 by in situ transmission x-ray microscopy. *Nano Lett.* **11,** 4386–4392 (2011).
65. Zhang, H. *et al.* Synthesis of Pd-Pt bimetallic nanocrystals with a concave structure through a bromide-induced galvanic replacement reaction. *J Am Chem Soc* **133,** 6078–6089 (2011).
66. Ortiz, N. & Skrabalak, S. E. Controlling the growth kinetics of nanocrystals via galvanic replacement: Synthesis of Au tetrapods and star-shaped decahedra. *Cryst. Growth Des.* **11,** 3545–3550 (2011).
67. Xia, X., Wang, Y., Ruditskiy, A. & Xia, Y. 25th Anniversary Article: Galvanic Replacement: A Simple and Versatile Route to Hollow Nanostructures with Tunable and Well-Controlled Properties. *Adv. Mater.* **25,** 6313–6333 (2013).
68. Zhang, W., Yang, J. & Lu, X. Tailoring galvanic replacement reaction for the preparation of Pt/Ag bimetallic hollow nanostructures with controlled number of voids. *ACS Nano* **6,** 7397–7405 (2012).
69. Gray, H. B. Powering the planet with solar fuel. *Nat. Chem.* **1,** 112 (2009).
70. Gasteiger, H. A. & Markovi , N. M. CHEMISTRY: Just a Dream--or Future Reality? *Science (80-.).* **324,** 48–49 (2009).
71. Park, S., Shao, Y., Liu, J. & Wang, Y. Oxygen electrocatalysts for water electrolyzers and reversible fuel cells: status and perspective. *Energy Environ. Sci.* **5,** 9331 (2012).
72. Liang, Y. *et al.* Co3O4 nanocrystals on graphene as a synergistic catalyst for oxygen reduction reaction. *Nat. Mater.* **10,** 780–786 (2011).
73. Guo, X., Xu, W., Li, S., Liu, Y. & Li, M. Surfactant-free scalable synthesis of hierarchically spherical Co 3 O 4 superstructures and their enhanced lithium-ion storage performances. *Nanotechnology* **465401,** 465401 (2012).
74. Gorlin, Y. & Jaramillo, T. F. A Bifunctional Nonprecious Metal Catalyst for Oxygen Reduction and Water Oxidation. *J. Am. Chem. Soc.* **132,** 13612–13614 (2010).
75. Kristian, N., Yu, Y., Lee, J.-M., Liu, X. & Wang, X. Synthesis and characterization of Cocore–Ptshell electrocatalyst prepared by spontaneous replacement reaction for oxygen reduction reaction. *Electrochim. Acta* **56,** 1000–1007 (2010).
76. Sa, Y. J., Kwon, K., Cheon, J. Y., Kleitz, F. & Joo, S. H. Ordered mesoporous Co3O4 spinels as stable, bifunctional, noble metal-free oxygen electrocatalysts. *J. Mater. Chem. A* **1,** 9992 (2013).
77. Huo, R., Jiang, W.-J., Xu, S., Zhang, F. & Hu, J.-S. Co/CoO/CoFe2O4/G nanocomposites derived from layered double hydroxides towards mass

production of efficient Pt-free electrocatalysts for oxygen reduction reaction. *Nanoscale* **6,** 203–206 (2014).

78. Lin, R. *et al.* Synthesis and application of core–shell Co@Pt/C electrocatalysts for proton exchange membrane fuel cells. *J. Power Sources* **223,** 190–198 (2013).
79. Wang, D. *et al.* Structurally ordered intermetallic platinum–cobalt core–shell nanoparticles with enhanced activity and stability as oxygen reduction electrocatalysts. *Nat. Mater.* **12,** 81–87 (2012).
80. Yin, Q. *et al.* A Fast Soluble Carbon-Free Molecular Water Oxidation Catalyst Based on Abundant Metals. *Science (80-.).* **328,** 342–345 (2010).
81. Kanan, M. W. & Nocera, D. G. In Situ Formation of an Oxygen-Evolving Catalyst in Neutral Water Containing Phosphate and Co2+. *Science (80-.).* **321,** 1072–1075 (2008).
82. Liang, Y. *et al.* Covalent hybrid of spinel manganese-cobalt oxide and graphene as advanced oxygen reduction electrocatalysts. *J. Am. Chem. Soc.* **134,** 3517–3523 (2012).
83. Yeager, E. Electrocatalysts for O2 reduction. *Electrochim. Acta* **29,** 1527–1537 (1984).
84. Snyder, J., McCue, I., Livi, K. & Erlebacher, J. Structure/Processing/Properties relationships in nanoporous nanoparticles as applied to catalysis of the cathodic oxygen reduction reaction. *J. Am. Chem. Soc.* **134,** 8633–8645 (2012).
85. Jin, W., Du, H., Zheng, S., Xu, H. & Zhang, Y. Comparison of the oxygen reduction reaction between NaOH and KOH solutions on a Pt electrode: The electrolyte-dependent effect. *J. Phys. Chem. B* **114,** 6542–6548 (2010).
86. Dembinska, B. Synthesis And Characterization of New Non-Platinum Electrocatalysts for Oxygen Reduction Beata Dembinska. *ECS Trans.* **45,** 77–88 (2013).
87. Trunov, A. Analysis of oxygen reduction reaction pathways on Co3O4, NiCo2O4, Co3O4–Li2O, NiO, NiO–Li2O, Pt, and Au electrodes in alkaline medium. *Electrochim. Acta* **105,** 506–513 (2013).
88. Loukrakpam, R. *et al.* Atomic Ordering Enhanced Electrocatalytic Activity of Nanoalloys for Oxygen Reduction Reaction. *J. Phys. Chem. C* **117,** 20715–20721 (2013).
89. Shan, S., Luo, J., Yang, L. & Zhong, C.-J. Nanoalloy catalysts: structural and catalytic properties. *Catal. Sci. Technol.* **4,** 3570–3588 (2014).
90. Jang, J.-H. *et al.* Rational syntheses of core-shell Fex@Pt nanoparticles for the study of electrocatalytic oxygen reduction reaction. *Sci. Rep.* **3,** 2872 (2013).
91. God ínez-Salom ón, F., Hallen-L ópez, M. & Solorza-Feria, O. Enhanced electroactivity for the oxygen reduction on Ni@Pt core-shell nanocatalysts. *Int. J. Hydrogen Energy* **37,** 14902–14910 (2012).
92. Wang, Y. *et al.* Carbon supported MnOx-Co3O4 as cathode catalyst for oxygen reduction reaction in alkaline media. *Int. J. Hydrogen Energy* **38,** 13611–13616 (2013).

93. Xu, J., Gao, P. & Zhao, T. S. Non-precious Co3O4 nano-rod electrocatalyst for oxygenreduction reaction in anion-exchange membranefuelcells. *Energy Environ. Sci.* **5,** 5333–5339 (2012).
94. Cook, T. R. *et al.* Solar Energy Supply and Storage for the Legacy and Nonlegacy Worlds. *Chem. Rev.* **110,** 6474–6502 (2010).
95. Higashi, M., Domen, K. & Abe, R. Fabrication of an efficient BaTaO2N photoanode harvesting a wide range of visible light for water splitting. *J. Am. Chem. Soc.* **135,** 10238–10241 (2013).
96. Ohno, T., Bai, L., Hisatomi, T., Maeda, K. & Domen, K. Photocatalytic water splitting using modified GaN:ZnO solid solution under visible light: Long-time operation and regeneration of activity. *J. Am. Chem. Soc.* **134,** 8254–8259 (2012).
97. Su, J., Guo, L., Bao, N. & Grimes, C. A. Nanostructured WO_3 /$BiVO_4$ Heterojunction Films for Efficient Photoelectrochemical Water Splitting. *Nano Lett.* **11,** 1928–1933 (2011).
98. Grimaud, A. *et al.* Double perovskites as a family of highly active catalysts for oxygen evolution in alkaline solution. *Nat. Commun.* **4,** 2439 (2013).
99. Suntivich, J., May, K. J., Gasteiger, H. A., Goodenough, J. B. & Shao-Horn, Y. A Perovskite Oxide Optimized for Oxygen Evolution Catalysis from Molecular Orbital Principles. *Science (80-.).* **334,** 1383–1385 (2011).
100. Zhu, Y. *et al.* $SrNb_{0.1}Co_{0.7}Fe_{0.2}O_{3-\delta}$ Perovskite as a Next-Generation Electrocatalyst for Oxygen Evolution in Alkaline Solution. *Angew. Chemie Int. Ed.* **54,** 3897–3901 (2015).
101. Zhu, Y. *et al.* Boosting Oxygen Reduction Reaction Activity of Palladium by Stabilizing Its Unusual Oxidation States in Perovskite. *Chem. Mater.* **27,** 3048–3054 (2015).
102. Jakšić, J. M., Labou, D., Papakonstantinou, G. D., Siokou, A. & Jakšić, M. M. Novel spillover interrelating reversible electrocatalysts for oxygen and hydrogen electrode reactions. *J. Phys. Chem. C* **114,** 18298–18312 (2010).
103. Ho, V., Pan, C., Rick, J., Su, W. & Hwang, B. Nanostructured Ti0. 7Mo0. 3O2 Support Enhances Electron Transfer to Pt: Used as High Performance Catalyst for Oxygen Reduction Reaction. *J. Am. Chem. Soc.* **133,** 11716–11724 (2011).
104. Zhu, Y. *et al.* A universal and facile way for the development of superior bifunctional electrocatalysts for oxygen reduction and evolution reactions utilizing the synergistic effect. *Chemistry* **20,** 15533–42 (2014).
105. ANTOLINI, E., SALGADO, J., GIZ, M. & GONZALEZ, E. Effects of geometric and electronic factors on ORR activity of carbon supported Pt–Co electrocatalysts in PEM fuel cells. *Int. J. Hydrogen Energy* **30,** 1213–1220 (2005).
106. Koh, S., Toney, M. F. & Strasser, P. Activity-stability relationships of ordered and disordered alloy phases of Pt3Co electrocatalysts for the oxygen reduction reaction (ORR). *Electrochim. Acta* **52,** 2765–2774 (2007).
107. Li, X. G., Colon-Mercado, H. R., Wu, G., Lee, J. W. & Popov, B. N.

Development of method for synthesis of Pt-Co cathode catalysts for PEM fuel cells. *Electrochem. Solid State Lett.* **10,** B201–B205 (2007).

108. Wang, Y.-J. *et al.* Carbon-Supported Pt-Based Alloy Electrocatalysts for the Oxygen Reduction Reaction in Polymer Electrolyte Membrane Fuel Cells: Particle Size, Shape, and Composition Manipulation and Their Impact to Activity. *Chem. Rev.* **115,** 3433–3467 (2015).
109. Zhao, X. *et al.* Octahedral Pd@Pt $_{1.8}$ Ni Core–Shell Nanocrystals with Ultrathin PtNi Alloy Shells as Active Catalysts for Oxygen Reduction Reaction. *J. Am. Chem. Soc.* **137,** 2804–2807 (2015).
110. Zhang, C., Hwang, S. Y., Trout, A. & Peng, Z. Solid-state chemistry-enabled scalable production of octahedral Pt-Ni alloy electrocatalyst for oxygen reduction reaction. *J. Am. Chem. Soc.* **136,** 7805–7808 (2014).
111. Zhang, Q.-H., Yang, W.-H., Wang, H.-H., Wang, M.-Q. & Cai, C.-J. Facile Synthesis of Platinum Alloy Nanoparticles with Enhanced Activity for Ethylene Glycol Electro-Oxidation. *ECS Electrochem. Lett.* **3,** F73–F75 (2014).
112. Han, L. *et al.* A seed-mediated approach to the morphology-controlled synthesis of bimetallic copper–platinum alloy nanoparticles with enhanced electrocatalytic performance for the methanol oxidation reaction. *J. Power Sources* **286,** 488–494 (2015).
113. Markovic, N. M., Schmidt, T. J., Stamenkovic, V. & Ross, P. N. Oxygen Reduction Reaction on Pt and Pt Bimetallic Surfaces: A Selective Review. *Fuel Cells* **1,** 105–116 (2001).
114. Paulus, U. & Wokaun, A. Oxygen Reduction on Carbon-Supported Pt - Ni and Pt - Co Alloy Catalysts. *J. Phys. Chem. B.* **106,** 4181–4191 (2002).
115. Toda, T., Igarashi, H., Uchida, H. & Watanabe, M. Enhancement of the electroreduction of Oxygen on Pt alloys with Fe, Ni, and Co. *J. Electrochem. Soc.* **146,** 3750–3756 (1999).
116. Stamenkovic, V. R. *et al.* Trends in electrocatalysis on extended and nanoscale Pt-bimetallic alloy surfaces. *Nat. Mater.* **6,** 241–247 (2007).
117. Greeley, J. *et al.* Alloys of platinum and early transition metals as oxygen reduction electrocatalysts. *Nat. Chem.* **1,** 552–556 (2009).
118. Wu, J. & Yang, H. Platinum-based oxygen reduction electrocatalysts. *Acc. Chem. Res.* **46,** 1848–1857 (2013).
119. US Department of Energy. Fuel Cell Technical Team Roadmap, June 2013. *Http://Www1.Eere.Energy.Gov/Vehiclesandfuels/Pdfs/Program/Fctt_Roadmap_June2013.Pdf* (2013). at <http://www1.eere.energy.gov/vehiclesandfuels/pdfs/program/fctt_roadmap_june2013.pdf>
120. Chen, B., Cheng, D. & Zhu, J. Synthesis of PtCu nanowires in nonaqueous solvent with enhanced activity and stability for oxygen reduction reaction. *J. Power Sources* **267,** 380–387 (2014).
121. Zhu, Z., Zhai, Y. & Dong, S. Facial Synthesis of PtM (M = Fe, Co, Cu, Ni) Bimetallic Alloy Nanosponges and Their Enhanced Catalysis for Oxygen

Reduction Reaction. *ACS Appl. Mater. Interfaces* **6,** 16721–6 (2014).
122. Wang, C. *et al.* Monodisperse Pt3Co nanoparticles as a catalyst for the oxygen reduction reaction: Size-dependent activity. *J. Phys. Chem. C* **113,** 19365–19368 (2009).
123. Wang, C., Markovic, N. M. & Stamenkovic, V. R. Advanced platinum alloy electrocatalysts for the oxygen reduction reaction. *ACS Catal.* **2,** 891–898 (2012).
124. Huang, X. *et al.* High-performance transition metal – doped Pt3Ni octahedra for oxygen reduction reaction. *Science (80-.).* **348,** 1230–1234 (2015).
125. Gan, L. *et al.* Element-specific anisotropic growth of shaped platinum alloy nanocrystals. *Science* **346,** 1502–6 (2014).
126. Li, H. *et al.* Design and preparation of highly active Pt-Pd/C catalyst for the oxygen reduction reaction. *J. Phys. Chem. C* **111,** 5605–5617 (2007).
127. Hyman, M. P. & Medlin, J. W. Effects of Electronic Structure Modifications on the Adsorption of Oxygen Reduction Reaction Intermediates on Model Pt (111)-Alloy Surfaces. *J. Phys. Chem. C* **111,** 17052–17060 (2007).
128. Xu, Y., Ruban, A. V. & Mavrikakis, M. Adsorption and Dissociation of O2 on Pt-Co and Pt-Fe Alloys. *J. Am. Chem. Soc.* **126,** 4717–4725 (2004).
129. Ma, Y. & Balbuena, P. B. Pt surface segregation in bimetallic Pt3M alloys: A density functional theory study. *Surf. Sci.* **602,** 107–113 (2008).
130. Cheng, D., Qiu, X. & Yu, H. Enhancing oxygen reduction reaction activity of Pt-shelled catalysts via subsurface alloying †. *Phys. Chem. Chem. Phys.* **1,** 20377–81 (2014).
131. Joya, K. S. & De Groot, H. J. M. Biomimetic molecular water splitting catalysts for hydrogen generation. *Int. J. Hydrogen Energy* **37,** 8787–8799 (2012).
132. Hisatomi, T., Kubota, J. & Domen, K. Recent advances in semiconductors for photocatalytic and photoelectrochemical water splitting. *Chem. Soc. Rev.* DOI: 10.1039/C3CS60378D (2014). doi:10.1039/c3cs60378d
133. Zamiri, R. *et al.* Laser assisted fabrication of ZnO/Ag and ZnO/Au core/shell nanocomposites. *Appl. Phys. A Mater. Sci. Process.* **111,** 487–493 (2013).
134. Giorgetti, E. *et al.* Cu/Ag-based bifunctional nanoparticles obtained by one-pot laser-assisted galvanic replacement. *J. Nanoparticle Res.* **15,** 1360 (2013).
135. Chen, Y. *et al.* The Study of Surface Plasmon in Au/Ag Core/Shell Compound Nanoparticles. *Plasmonics* **7,** 509–513 (2012).
136. Gu, L. W. C. C. Z. H. K. J. C. E. E. C. D., Lukaszew, R. a & Lei Wang , César Clavero , Zachary Huba , Kyler J. Carroll , Everett E. Carpenter , Diefeng Gu, and R. a. L. Plasmonics and Enhanced Magneto-Optics in Core− Shell Co− Ag Nanoparticles. *Nano Lett.* **11,** 1237–1240 (2011).
137. Raza, S., Yan, W., Stenger, N., Wubs, M. & Mortensen, N. A. Blueshift of the surface plasmon resonance in silver nanoparticles: substrate effects. *Opt. Express* **21,** 27344 (2013).
138. Sachan, R. *et al.* Self-organized bimetallic Ag–Co nanoparticles with tunable

localized surface plasmons showing high environmental stability and sensitivity. *Nanotechnology* **23,** 275604 (2012).
139. Warren, S. C. & Thimsen, E. Plasmonic solar water splitting. *Energy Environ. Sci.* **5,** 5133–5146 (2012).
140. Liu, Z., Hou, W., Pavaskar, P., Aykol, M. & Cronin, S. B. Plasmon resonant enhancement of photocatalytic water splitting under visible illumination. *Nano Lett.* **11,** 1111–1116 (2011).
141. Nørskov, J. K. *et al.* Origin of the overpotential for oxygen reduction at a fuel-cell cathode. *J. Phys. Chem. B* **108,** 17886–17892 (2004).
142. Nørskov, J. K., Bligaard, T., Rossmeisl, J. & Christensen, C. H. Towards the computational design of solid catalysts. *Nat. Chem.* **1,** 37–46 (2009).
143. Liu, X. *et al.* Co3O4/C nanocapsules with onion-like carbon shells as anode material for lithium ion batteries. *Electrochim. Acta* **100,** 140–146 (2013).
144. Wen, Z. *et al.* A facile fluorine-mediated hydrothermal route to controlled synthesis of rhombus-shaped Co3O4 nanorod arrays and their application in gas sensing. *J. Mater. Chem. A* **1,** 7511 (2013).
145. Vijayakumar, S., Kiruthika Ponnalagi, a., Nagamuthu, S. & Muralidharan, G. Microwave assisted synthesis of Co3O4 nanoparticles for high-performance supercapacitors. *Electrochim. Acta* **106,** 500–505 (2013).
146. Patil, D., Patil, P., Subramanian, V., Joy, P. a & Potdar, H. S. Highly sensitive and fast responding CO sensor based on Co3O4 nanorods. *Talanta* **81,** 37–43 (2010).
147. Zhang, M., de Respinis, M. & Frei, H. Time-resolved observations of water oxidation intermediates on a cobalt oxide nanoparticle catalyst. *Nat. Chem.* **6,** 362–367 (2014).
148. Risch, M. *et al.* Atomic structure of cobalt-oxide nanoparticles active in light-driven catalysis of water oxidation. *Int. J. Hydrogen Energy* **37,** 8878–8888 (2012).
149. Sun, X. *et al.* Morphology controlled high performance supercapacitor behaviour of the Ni-Co binary hydroxide system. *J. Power Sources* **238,** 150–156 (2013).
150. Gong, L. & Su, L. Facile synthesis and capacitive performance of the Co(OH)2 nanostructure via a ball-milling method. *Appl. Surf. Sci.* **257,** 10201–10205 (2011).
151. Wang, Z., Chen, X., Zhang, M. & Qian, Y. Synthesis of Co3O4 nanorod bunches from a single precursor Co(CO3)0.35Cl0.20(OH)1.10. *Solid State Sci.* **7,** 13–15 (2005).
152. Zhu, H. T. *et al.* Synthesis and magnetic properties of antiferromagnetic Co3O4 nanoparticles. *Phys. B Condens. Matter* **403,** 3141–3145 (2008).
153. Karthick, S. N., Hemalatha, K. V., Justin Raj, C., Kim, H. J. & Yi, M. Synthesis of nano-bound microsphere Co3O4 by simple polymer-assisted sol–gel technique. *J. Nanoparticle Res.* **15,** 1474 (2013).
154. Liu, Z., Ma, R., Osada, M., Takada, K. & Sasaki, T. Selective and controlled

synthesis of alpha- and beta-cobalt hydroxides in highly developed hexagonal platelets. *J. Am. Chem. Soc.* **127,** 13869–13874 (2005).

155. Yang, J., Liu, H., Martens, W. N. & Frost, R. L. Synthesis and characterization of Cobalt hydroxide, cobalt oxyhydroxide, and cobalt oxide nanodiscs. *J. Phys. Chem. C* **114,** 111–119 (2010).
156. Gallant, D., Pézolet, M. & Simard, S. Optical and physical properties of cobalt oxide films electrogenerated in bicarbonate aqueous media. *J. Phys. Chem. B* **110,** 6871–6880 (2006).
157. Jiang, R., Li, B., Fang, C. & Wang, J. Metal/Semiconductor Hybrid Nanostructures for Plasmon-Enhanced Applications. *Adv. Mater.* **26,** 5274–5309 (2014).
158. Huang, Y. *et al.* Transient Platinum Oxide Formation and Oxygen Reduction on Carbon-Supported Platinum and Platinum-Cobalt Alloy Electrocatalysts. *J. Electrochem. Soc.* **161,** 10–15 (2014).
159. Shan, S. *et al.* Nanoalloy catalysts for electrochemical energy conversion and storage reactions. *RSC Adv.* **4,** 42654–42669 (2014).
160. Hu, S., Goenaga, G., Melton, C., Zawodzinski, T. A. & Mukherjee, D. PtCo/CoOx nanocomposites: Bifunctional electrocatalysts for oxygen reduction and evolution reactions synthesized via tandem laser ablation synthesis in solution-galvanic replacement reactions. *Appl. Catal. B Environ.* **182,** 286–296 (2016).
161. Lu, X. *et al.* Mechanistic studies on the galvanic replacement reaction between multiply twinned particles of Ag and HAuCl4 in an organic medium. *J. Am. Chem. Soc.* **129,** 1733–1742 (2007).
162. Sun, Y. & Xia, Y. Mechanistic Study on the Replacement Reaction between Silver Nanostructures and Chloroauric Acid in Aqueous Medium. *J. Am. Chem. Soc.* **126,** 3892–3901 (2004).
163. Huang, Q., Yang, H., Tang, Y., Lu, T. & Akins, D. L. Carbon-supported Pt-Co alloy nanoparticles for oxygen reduction reaction. *Electrochem. commun.* **8,** 1220–1224 (2006).
164. Salgado, J. R. C., Antolini, E. & Gonzalez, E. R. Structure and Activity of Carbon-Supported Pt−Co Electrocatalysts for Oxygen Reduction. *J. Phys. Chem. B* **108,** 17767–17774 (2004).
165. Stamenković, V., Schmidt, T. J., Ross, P. N. & Marković, N. M. Surface Composition Effects in Electrocatalysis: Kinetics of Oxygen Reduction on Well-Defined Pt 3 Ni and Pt 3 Co Alloy Surfaces. *J. Phys. Chem. B* **106,** 11970–11979 (2002).
166. Cortés-Escobedo, C. a. *et al.* Mechanically activated Pt-Ni and Pt-Co alloys as electrocatalysts in the oxygen reduction reaction. *Int. J. Hydrogen Energy* **39,** 16722–16730 (2014).
167. Kim, J. W. *et al.* Effects of stabilizers on the synthesis of Pt3Cox/C electrocatalysts for oxygen reduction. *Int. J. Hydrogen Energy* **36,** 12088–12095 (2011).

168. Duong, H. T., Rigsby, M. a., Zhou, W. P. & Wieckowski, A. Oxygen reduction catalysis of the Pt3Co alloy in alkaline and acidic media studied by X-ray photoelectron spectroscopy and electrochemical methods. *J. Phys. Chem. C* **111,** 13460–13465 (2007).
169. He, Q. & Mukerjee, S. Electrocatalysis of oxygen reduction on carbon-supported PtCo catalysts prepared by water-in-oil micro-emulsion. *Electrochim. Acta* **55,** 1709–1719 (2010).
170. Zignani, S. C., Antolini, E. & Gonzalez, E. R. Evaluation of the stability and durability of Pt and Pt-Co/C catalysts for polymer electrolyte membrane fuel cells. *J. Power Sources* **182,** 83–90 (2008).
171. Hwang, B. J. *et al.* An Investigation of Structure - Catalytic Activity Relationship for Pt - Co / C Bimetallic Nanoparticles toward the Oxygen Reduction Reaction. *J. Phys. Chem. C* **111,** 15267–15276 (2007).
172. Carpenter, M. K., Moylan, T. E., Kukreja, R. S., Atwan, M. H. & Tessema, M. M. Solvothermal synthesis of platinum alloy nanoparticles for oxygen reduction electrocatalysis. *J. Am. Chem. Soc.* **134,** 8535–8542 (2012).
173. Santiago, E. I., Varanda, L. C. & Villullas, H. M. Carbon-supported Pt-Co catalysts prepared by a modified polyol process as cathodes for PEM fuel cells. *J. Phys. Chem. C* **111,** 3146–3151 (2007).
174. Liu, Z., Yu, C., Rusakova, I. a., Huang, D. & Strasser, P. Synthesis of Pt3Co alloy nanocatalyst via reverse micelle for oxygen reduction reaction in PEMFCs. *Top. Catal.* **49,** 241–250 (2008).
175. Zheng, J. N. *et al.* One-pot synthesis of platinum3cobalt nanoflowers with enhanced oxygen reduction and methanol oxidation. *J. Power Sources* **268,** 744–751 (2014).
176. Ledoux, G., Amans, D., Dujardin, C. & Masenelli-Varlot, K. Facile and rapid synthesis of highly luminescent nanoparticles via pulsed laser ablation in liquid. *Nanotechnology* **20,** 445605 (2009).
177. Liu, P., Cui, H., Wang, C. X. & Yang, G. W. From nanocrystal synthesis to functional nanostructure fabrication: laser ablation in liquid. *Phys. Chem. Chem. Phys.* **12,** 3942–52 (2010).
178. Zeng, H. *et al.* Nanomaterials via Laser Ablation/Irradiation in Liquid: A Review. *Adv. Funct. Mater.* **22,** 1333–1353 (2012).
179. Sievers, G. *et al.* Mesoporous Pt–Co oxygen reduction reaction (ORR) catalysts for low temperature proton exchange membrane fuel cell synthesized by alternating sputtering. *J. Power Sources* **268,** 255–260 (2014).
180. Schenk, A. *et al.* Platinum-cobalt catalysts for the oxygen reduction reaction in high temperature proton exchange membrane fuel cells - Long term behavior under ex-situ and in-situ conditions. *J. Power Sources* **266,** 313–322 (2014).
181. Wang, C. *et al.* Synthesis of Homogeneous Pt-Bimetallic Nanoparticles as Highly Efficient Electrocatalysts. *Acs Catal.* **1,** 1355–1359 (2011).
182. Hu, G. *et al.* Atomistic understanding of the origin of high oxygen reduction electrocatalytic activity of cuboctahedral Pt $_3$ Co–Pt core–shell nanoparticles.

Catal. Sci. Technol. (2015). doi:10.1039/C5CY01128K
183. Chu, M.-W. *et al.* Probing Bright and Dark Surface-Plasmon Modes in Individual and Coupled Noble Metal Nanoparticles Using an Electron Beam. *Nano Lett.* **9,** 399–404 (2009).
184. Koh, A. L. *et al.* Electron Energy-Loss Spectroscopy (EELS) of Surface Plasmons in Single Silver Nanoparticles and Dimers: Influence of Beam Damage and Mapping of Dark Modes. *ACS Nano* **3,** 3015–3022 (2009).
185. Sachan, R. *et al.* Ferroplasmons : Intense Localized Surface Plasmons in Metal-. *ACS Nano* **8,** 9790–9798 (2014).
186. Bosman, M., Keast, V. J., Watanabe, M., Maaroof, A. I. & Cortie, M. B. Mapping surface plasmons at the nanometre scale with an electron beam. *Nanotechnology* **18,** 165505 (2007).
187. Gramotnev, D. K. & Bozhevolnyi, S. I. Plasmonics beyond the diffraction limit. *Nat. Photonics* **4,** 83–91 (2010).
188. Laux, E., Genet, C., Skauli, T. & Ebbesen, T. W. Plasmonic photon sorters for spectral and polarimetric imaging. *Nat. Photonics* **2,** 161–164 (2008).
189. Ferry, V. E., Munday, J. N. & Atwater, H. A. Design Considerations for Plasmonic Photovoltaics. *Adv. Mater.* **22,** 4794–4808 (2010).
190. Huschka, R. *et al.* Light-induced release of DNA from gold nanoparticles: Nanoshells and nanorods. *J. Am. Chem. Soc.* **133,** 12247–12255 (2011).
191. Zhang, H., Harpster, M. H., Wilson, W. C. & Johnson, P. a. Surface-enhanced Raman scattering detection of DNAs derived from virus genomes using Au-coated paramagnetic nanoparticles. *Langmuir* **28,** 4030–7 (2012).
192. Linic, S., Christopher, P. & Ingram, D. B. Plasmonic-metal nanostructures for efficient conversion of solar to chemical energy. *Nat. Mater.* **10,** 911–921 (2011).
193. Field, E. Ag @ SiO 2 Core Shell Nanoparticles for Surface-Enhanced Raman Scattering. **3,** 3493–3496 (2009).
194. Lezec, H. & Thio, T. Diffracted evanescent wave model for enhanced and suppressed optical transmission through subwavelength hole arrays. *Opt. Express* **12,** 3629–3651 (2004).
195. Pillai, S. & Catchpole, K. Surface plasmon enhanced silicon solar cells. *J. Appl. Phys.* **101,** 093105 (2007).
196. Sershen, S. R., Westcott, S. L., Halas, N. J. & West, J. L. Temperature-sensitive polymer-nanoshell composites for photothermally modulated drug delivery. *J. Biomed. Mater. Res.* **51,** 293–298 (2000).
197. Lal, S., Clare, S. E. & Halas, N. J. Nanoshell-enabled photothermal cancer therapy: Impending clinical impact. *Acc. Chem. Res.* **41,** 1842–1851 (2008).
198. Öztürk, Z. F. Field enhancement at metallic interfaces due to quantum confinement. *J. Nanophotonics* **5,** 051602 (2011).
199. Kraus, W. & Schatz, G. Plasmon resonance broadening in small metal particles. *J. Chem. Phys.* **79,** 6130–6139 (1983).
200. Esteban, R., Borisov, A. G., Nordlander, P. & Aizpurua, J. Bridging quantum

and classical plasmonics with a quantum-corrected model. *Nat. Commun.* **3,** 825 (2012).

201. Zuloaga, J., Prodan, E. & Nordlander, P. Quantum description of the plasmon resonances of a nanoparticle dimer. *Nano Lett.* **9,** 887–891 (2009).
202. Raza, S., Toscano, G., Jauho, A.-P., Wubs, M. & Mortensen, N. A. Unusual resonances in nanoplasmonic structures due to nonlocal response. *Phys. Rev. B* **84,** 121412 (2011).
203. Aizpurua, J. & Rivacoba, A. Nonlocal effects in the plasmons of nanowires and nanocavities excited by fast electron beams. *Phys. Rev. B - Condens. Matter Mater. Phys.* **78,** 035404 (2008).
204. Yan, Z., Compagnini, G. & Chrisey, D. B. Generation of AgCl cubes by excimer laser ablation of bulk Ag in aqueous NaCl solutions. *J. Phys. Chem. C* **115,** 5058–5062 (2011).
205. Yan, Z., Bao, R. & Chrisey, D. B. Generation of Ag–Ag_2O complex nanostructures by excimer laser ablation of Ag in water. *Phys. Chem. Chem. Phys.* **15,** 3052–3056 (2013).
206. Amendola, V., Polizzi, S. & Meneghetti, M. Laser Ablation Synthesis of Silver Nanoparticles Embedded in Graphitic Carbon Matrix. *Sci. Adv. Mater.* **4,** 497–500 (2012).
207. Kalyva, M. *et al.* Electrical response from nanocomposite PDMS-Ag NPs generated by in situ laser ablation in solution. *Nanotechnology* **24,** 035707 (2013).
208. Malviya, K. D. & Chattopadhyay, K. Synthesis and mechanism of composition and size dependent morphology selection in nanoparticles of Ag-Cu alloys processed by laser ablation under liquid medium. *J. Phys. Chem. C* **118,** 13228–13237 (2014).
209. Mottaghi, N. *et al.* Ag/Pd core-shell nanoparticles by a successive method: Pulsed laser ablation of Ag in water and reduction reaction of PdCl2. *Appl. Surf. Sci.* **292,** 892–897 (2014).
210. Mendivil, M. I. *et al.* Synthesis of silver nanoparticles and antimony oxide nanocrystals by pulsed laser ablation in liquid media. *Appl. Phys. A* **110,** 809–816 (2013).
211. Li, G. *et al.* Spatially Mapping Energy Transfer from Single Plasmonic Particles to Semiconductor Substrates via STEM/EELS. *Nano Lett.* 150410084932000 (2015). doi:10.1021/acs.nanolett.5b00802
212. Scholl, J. a., Koh, A. L. & Dionne, J. a. Quantum plasmon resonances of individual metallic nanoparticles. *Nature* **483,** 421–427 (2012).
213. Bosman, M. *et al.* Surface Plasmon Damping Quantified with an Electron Nanoprobe. *Sci. Rep.* **3,** 1–7 (2013).
214. Guiton, B. S. *et al.* Correlated Optical Measurements and Plasmon Mapping of Silver Nanorods. *Nano Lett.* **11,** 3482–3488 (2011).
215. Collins, S. M., Nicoletti, O., Rossouw, D., Ostasevicius, T. & Midgley, P. A. Excitation Dependent Fano-like Interference Effects in Plasmonic Silver

Nanorods. *Phys. Rev. B* **90,** 155419 (2014).
216. Raza, S. *et al.* Extremely confined gap surface-plasmon modes excited by electrons. *Nat. Commun.* **5,** 1–7 (2014).
217. Diaz-Egea, C. *et al.* Mapping the plasmonic response of gold nanoparticles embedded in TiO 2 thin films. *Nanotechnology* **26,** 405702 (2015).
218. Wang, H. *et al.* Multifunctional TiO2 nanowires-modified nanoparticles bilayer film for 3D dye-sensitized solar cells. *Optoelectron. Adv. Mater. Rapid Commun.* **4,** 1166–1169 (2010).
219. Iberi, V., Mirsaleh-Kohan, N. & Camden, J. P. Understanding plasmonic properties in metallic nanostructures by correlating photonic and electronic excitations. *J. Phys. Chem. Lett.* **4,** 1070–1078 (2013).
220. Pedireddy, S. *et al.* Synthesis of Spiky Ag − Au Octahedral Nanoparticles and Their Tunable Optical Properties. *J. Phys. Chem. C* **117,** 16640–16649 (2013).
221. Scholl, J. a., Garc á-Etxarri, A., Koh, A. L. & Dionne, J. a. Observation of Quantum Tunneling between Two Plasmonic Nanoparticles. *Nano Lett.* **13,** 564–569 (2013).
222. Wang, D. *et al.* Structurally ordered intermetallic platinum–cobalt core–shell nanoparticles with enhanced activity and stability as oxygen reduction electrocatalysts. *Nat. Mater.* **12,** 81–87 (2012).

Appendices

Appendix A. Band gap/edge measurement

Experimental

Band gap measurement

Band gaps were measured using diffuse reflectance spectroscopy, with the main mechanism picture illustrated in Fig. A1. Generally speaking, a measurement light and a reference light will be shot on two standard white boards separately as background first, thereafter, replace one white board with sample and do the measurement again. The diffuse reflectance light will be absorbed by the spherical detector, and therefore can be shown in the monitor. In order to minimize the specular reflection component and meanwhile allow the incident beam going deeper into the sample to collect more scattered light, samples under detect need to be grounded and diluted by a non-absorbing matrix material but with similar reflective index such as KBr (for IR light) at a ratio of 1-5% by weight.

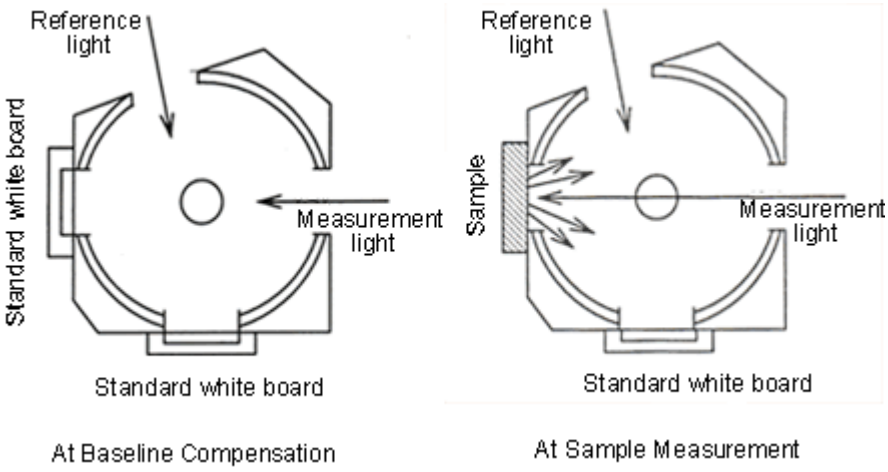


Fig. A1 Mechanistic picture for diffuse reflectance measurement. (http://www.shimadzu.com/an/spectro/uv/accessory/solidsample/solid.html)

After measuring the diffuse reflectance R, the Kubelka-Munk equation can be applied to obtain the ratio of the absorption coefficient k over scattering coefficient s,

$$F(R) = \frac{(1-R)^2}{2R} = \frac{k}{s}$$

Then by applying Tauc equation, band gap E_g can be calculated.

$$(Fh\upsilon)^2 = h\upsilon - E_g$$

It needs to be pointed out that the particle size must be way smaller than the thickness of the sample for collecting adequate amount of scatting signals. Meanwhile the white standard should be properly chosen based on the wavelength of incident light, i.e., KBr works for IR range, while $BaSO_4$ and MgO are usually used for UV-Vis, Spectralon usually applies for UV-Vis-NIR.

Band edge measurement

The interface between an electrode and an electrolyte could be modeled by an equivalent circuit, also called a Randles circuit, which is comprised of a double layer capacitor (namely Inner Helmholtz plane (IHP) and Outer Helmholtz plane (OHP)), in parallel with a polarization resistor, a Warburg impedance (maybe), along with a resistor in series connection, as shown in Fig. A2. The model involves both a faradaic part, which is correlated to redox reactions, and a non-faradaic part (capacitive component) that is considered as noises. EIS makes possible separating those two parts by providing both a direct and alternating potential during tests. And by applying the Butler-Volmer equation,

$$i = i_0\{\exp(-\frac{\alpha nF}{RT}\eta) - \exp[\frac{(1-\alpha)nF}{RT}\eta]\}$$

The whole impedance can be expressed as two parts, namely, a real part Z' and an imaginary number Z", i.e.,

$$Z(\omega) = Z'(\omega) + jZ''(\omega)$$

By plotting the imaginary number Z" against the real part Z', or plotting the absolute value of impedance or phase angle vs. frequency, we can either obtain Nyquist plot or Bode plot respectively.

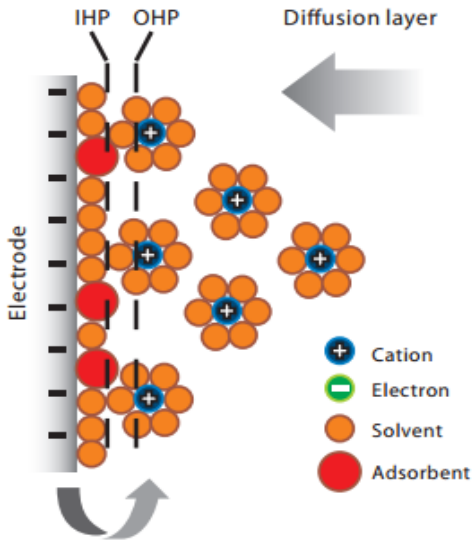


Fig. A2 Schematic illustration of equivalent circuit (Randles circuit) at an electrode electrolyte interface.

Finally, the double-layer capacitance could be obtained by fitting with models, thereafter the flat band potential that can be regarded either as conduction band edge (p-type semiconductor) or valance band edge (n-type semiconductor) will be measured by extrapolating the Mott-Schottky plots:

$$\frac{1}{C_{sc}^2} = \frac{2}{e\xi\xi_0 N}(E - E_{FB} - \frac{kT}{e})$$

Preliminary results

Due to the extreme thermodynamic condition within the liquid confined plasma plume for the LASiS-GRR process, the resultant products might differ from the counterparts synthesized through conventional methods in terms of crystalline structures and quantum properties. Therefore, it is necessary to measure their band gap and band edge for photocatalysis purposes. The band gap can be measured via Ultraviolet–visible diffuse reflectance spectra, specifically, according to the Tauc equation: $(F\upsilon)^2 = \upsilon - E_g$, where F is the Kubelka–Munk function of the diffuse reflectance R: $F = (1-R)^2/2R$, therefore by plotting $(F\upsilon)^2$ vs. υ, the intercepts of extrapolated straight lines can give us the corresponding direct band gaps of the

photocatalysts understudy. On the other hand, band edge will be measured via electrochemical impedance spectroscopy by applying Mott-Schottky plots:

$$\frac{1}{C_{sc}^2} = \frac{2}{e\xi\xi_0 N}(E - E_{FB} - \frac{kT}{e})$$

For exploiting the potentials of our synthesized NCs to be utilized as photocatalysts, the corresponding band gaps of ZnO and TiO_2 were preliminarily measured to be 3.3 and 3.6 eV, while after embedding with Ag, the band gaps shift to 3.8 for Ag/ZnO and 2.5 for Ag/TiO_2 (Fig. A3).

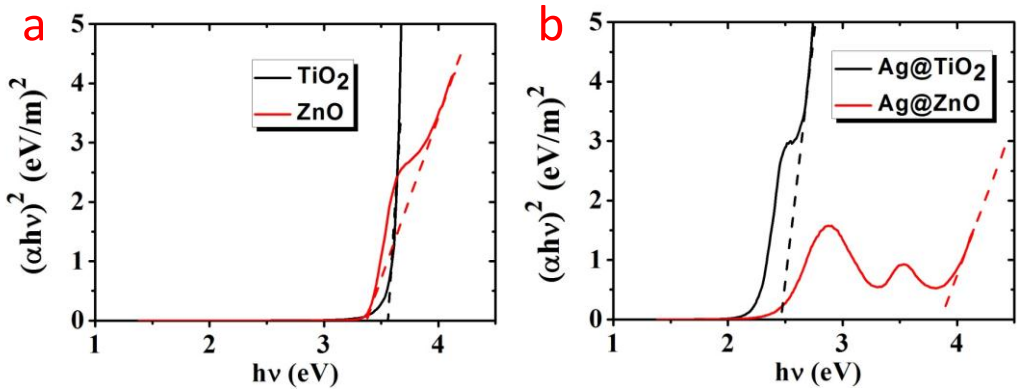


Fig. A3 Measurement of band gaps using Tauc plots for **a**, TiO_2 and ZnO NPs and **b**, Ag embedded TiO_2 and ZnO NCs.

On another hand, the band edges were measured via electrochemistry impedance spectroscopy (EIS). Fig. A4.a shows our preliminary results for the Nyquist plot of the CoO_x NPs that implies the relationship between the real part and imaginary part of the measured impedance at various applied potentials. By fitting with the equivalent circuit (Fig. A5), NP-electrolyte interface capacitances can be calculated and plotted with the corresponding applied potentials (Mott-Schottky plot, Fig. A4.b). The flat-band potential (considered as the valance band of NP) is then determined to be -0.59 V vs. NHE by extrapolating the straight line to C^{-2}=0. The conduction band can then be calculated as 2.9 V vs NHE.

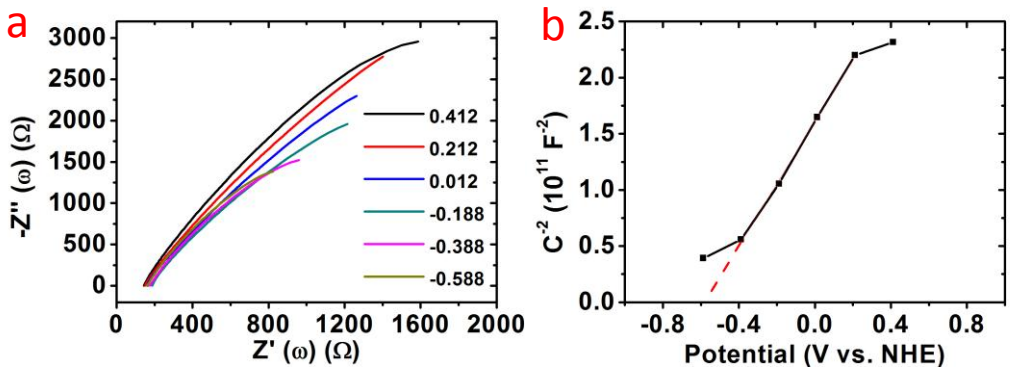


Fig. A4 Electrochemistry Impedance Spectroscopy (EIS) results for CoO_x NPs synthesized from LASiS: **a,** Nyquist plot at different applied potential; **b,** Mott-Schottky plot for calculation of the flat-band potential.

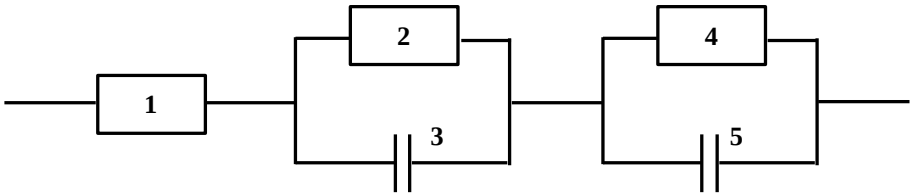


Fig. A5 Equivalent circuit used to mimic the impedance in the electrochemistry system. 1. Electrolyte resistance; 2. NP resistance; 3. NP/electrolyte interface capacitance; 4. Charge transfer resistance; 5. NP capacitance.

It needs to be mentioned the above results for the band gape/edge measurements are in their preliminary stage. In future, we will confirm those data and meanwhile applied these band gap/edge measurements to all the NPs, NCs we synthesized in earlier chapters, especially for the photocatalytic materials ZnO and TiO_2 before and after embedding the plasmonic Ag/Au. This will in turn help us to determine what types of semiconductors they can play in either a one-step or two-step excitation routes for setting up an efficient solar water splitting system.

Appendix B. EELS study of the plasmonic Ag/TiO_2 NCs

Electron energy loss spectroscopy (EELS) studies in Fig. A6 shows that the center Ag NP (position **d**) barely has any Plasmon peak, while the bottom Ag near the edge (position **e**) displays a slight peak at 2.5 eV, which matches with the plasmonic

peak in the UV-Vis spectra at ~500 nm. For the top Ag NP that is half-embedded in the srilankite type TiO_2, EELS is taken at three different spots. It is noted that from the spot **c** to **a**, i.e., towards outside of the matrix, the LSPR peak shifts from mono peak at 2.5 eV to a bimodal peak centered at 2.6 eV and 3.1 eV, that corresponds to wavelengths of ~480 nm and ~400 nm respectively. EELS results match very well with the UV-Vis spectra for the LSPR peak positions, indicating that outside part of the Ag gives rise to the new minor peak at ~400 nm after RI, and in turn confirms our assumption that RI re-structures the already formed core-shell NCs by driving the embedded Ag NPs outwards. It needs to be pointed out that the LSPR intensities can be dramatically blocked by the TiO_x matrix, especially for the one located at 3.1 eV (400 nm), which is probably due to the strong interaction between the two species.

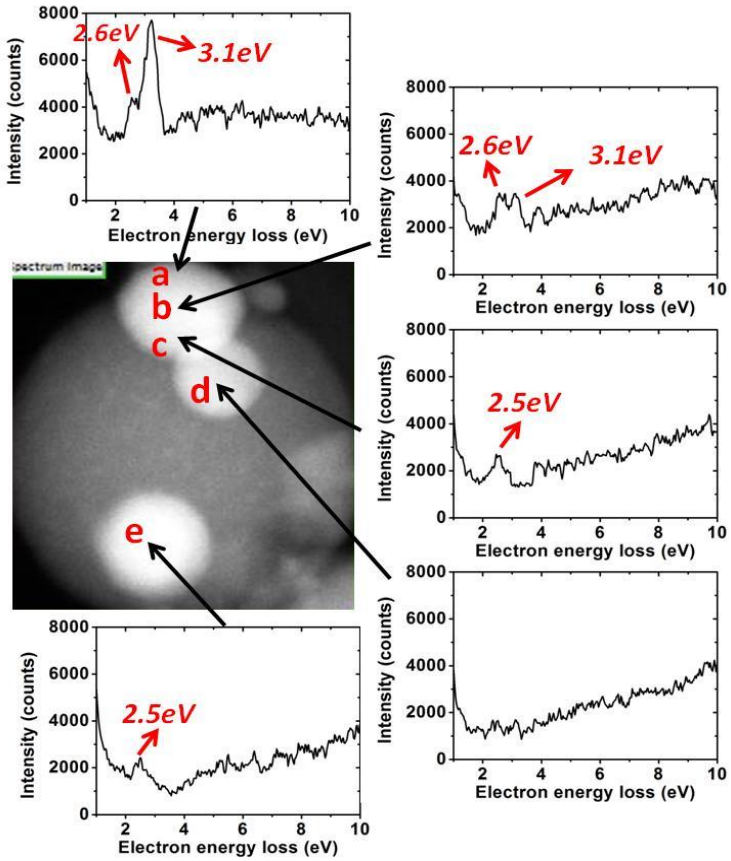


Fig. A6 EELS spectra at various positions of the embedded Ag NPs in Ag/TiO_2 NCs.

Vita

Sheng Hu was born on Jun 30, 1986 in Hangzhou, China, to the parents of Zhizhong Hu and Xinyu Huang. He attended Hangzhou No. 2 High School of Zhejiang province in 2002. After graduation, he headed west to Sichuan University, China in 2005, with the major of Polymer Material Processing Engineering. After getting a Bachelor degree in the summer of 2009, he then worked in the company of Panasonic (Hangzhou) for one year. In 2010 fall, he decided to study in the department of Chemical and Biomolecular Engineering at the University of Tennessee, Knoxville as a graduate student with full assistantship. Sheng Hu graduated with a Master of Science degree in Polymer Engineering in August 2012. Thereafter, he continued his research as a Ph.D. candidate in Department of Chemical and Biomolecular Engineering under the supervision of Dr. Dibyendu Mukherjee affiliated with the Sustainable Energy Education and Reserach Center (SEERC).